

A Thermoelectric Investigation of Selected Lead Salts  
and the Spin-Seebeck Effect in Semiconductors

A Dissertation

Presented in Partial Fulfillment of the Requirements for the Degree Doctor of Philosophy  
in the Graduate School of The Ohio State University

By

Christopher M. Jaworski

Graduate Program in Mechanical Engineering

The Ohio State University

2012

Dissertation Committee:

Joseph P. Heremans, Advisor

Sandip Mazumder

Roberto Myers

Walter Lempert

©

Christopher M. Jaworski

2012

## Abstract

The dimensionless thermoelectric figure of merit,  $zT$ , is used to characterize the conversion efficiency of thermoelectric materials. In this dissertation, we include experimental results on new  $p$ -type semiconducting alloys based on lead telluride that have higher  $zT$  values than historical materials. Through alloying PbTe:Tl with sulfur, we demonstrate an increase in  $zT$  over the parent material PbTe:Tl. Next, we remove the toxic element Tl from the PbTe/PbS alloy and retain the high efficiency via doping heavy valence band in PbTe, a separate mechanism than the high- $zT$  resonant level doping achieved by the impurity Tl. We present experimental evidence relevant to the valence band structure of PbTe alloys at elevated temperature and demonstrate that these alloys remain direct gap semiconductors at temperatures relevant to automotive thermoelectric waste heat recovery (<850K).

Secondly, we report the first confirmation measurement of a new effect – the spin-Seebeck effect – in thin films of GaMnAs, of work by researchers at Tohoku University two years prior on NiFe. The spin-Seebeck effect is a thermally driven spin distribution – the spin analog to the charge-Seebeck effect, and is measured using the inverse spin Hall effect in platinum transducers that are attached to the spin-polarized material. We report extensive measurements over temperature and at various positions along the sample. We show that this effect is phonon driven, and that a phonon-magnon drag is capable of

enhancing the magnitude of this effect, much like phonon-electron drag in charge Seebeck. Lastly, by using a non-magnetic material with large spin orbit interaction, we show the magnitude of this effect can reach the order of mV/K, whereas in ferromagnets it is order  $\mu\text{V/K}$ . Here, external magnetic field generates the necessary spin splitting. The discovery of this effect may allow for solid state heat engines based off spin, as an analog to thermoelectricity heat engines.

## Acknowledgments

Foremost, I would like to thank my parents: for all their support throughout the years. Next, I would like to thank my advisor Professor Heremans for all the late nights in the labs, the detailed discussions about our latest ideas, and the independence that I developed in a research setting. Vladimir Jovovic was instrumental in my training and with helping me through the beginning of my graduate school education. Next, I'd like to thank Professor Myers, for initializing the three of us to the spin-Seebeck effect. Lastly, I'd like to thank my colleague Michele Nielsen for all of our coffee breaks full of thermoelectric discussion.

I would also like to thank the various funding agencies that made my graduate study possible. I received two one-year fellowships: my first year of study I received the Innovative Incentive Program Fellowship, my final year I received the Graduate Automotive Technology Education Fellowship. The years in-between I was funded by a Department of Energy Energy Efficiency and Renewable Energy grant in a collaboration between researchers and engineers at Ford, Visteon, Amerigon, ZT:Plus, and the Ohio State University. Portions of the research in this dissertation are published as detailed in the Vita and subjected to copyright policies of Nature Publishing Group, American Physical Society, and Royal Society of Chemistry. Usages only occur in cases where I am 1<sup>st</sup> author and are in accordance with the copyright holder's policies concerning Ph.D. Dissertations.

## **Vita**

April 29, 1985.....Born – Lorain, Ohio

June 2007.....B.S., Mechanical Engineering, The Ohio State University

December 2008.....M.S., Mechanical Engineering, The Ohio State University

June 2007-present.....Graduate Research Associate/Graduate Fellow  
The Ohio State University

## **Fields of Study**

Major Field: Mechanical Engineering

## Publications

1. Jin, H., Jaworski, C.M., and Heremans, J.P., “Enhancement in the Figure of Merit of p-type  $\text{Bi}_{100-x}\text{Sb}_x$  alloys through multiple valence-band doping” *Appl. Phys. Lett.*, 2012, *accepted*
2. Jaworski, C.M., Myers, R.C., Johnston-Halperin, E., and Heremans J.P., “Giant spin-Seebeck effect in a non-magnetic material”, *Nature*, **487**, 210, 2012.
3. Nielsen, M.D., Levin, E.M., Jaworski, C.M., Schmidt-Rohr, K., Heremans, J.P., “Chromium as a resonant donor impurity in PbTe” *Phys. Rev. B*, **85** 045210, 2012
4. Jaworski, C.M. & Heremans, J.P., “Thermoelectric transport properties of the n-type impurity Al in PbTe” *Phys. Rev. B*, **85** 033204, 2012
5. Jaworski, C.M., Wiendlocha, B., Jovovic, V., and Heremans, J.P., “Combining Alloys Scattering of Phonons and Resonant Electron Levels to Reach a High Thermoelectric Figure of Merit in PbTeSe and PbTeS alloys”, *Energy & Environ. Sci.*, **4** 4155, 2011.
6. Girard, S.N., He, J., Zhou, X., Shoemaker, D., Jaworski, C. M., Uher, C., David, V.P., Heremans, J.P., Kanatzidis, M.G. “High Performance Na-doped PbTe-PbS thermoelectric Materials: Electronic Density of States Modification and Shape-Controlled Nanostructures” *J. Am. Chem. Soc.* **133** 41 16588, 2011.
7. Jaworski, C.M., Yang, J., Mack, S., Awschalom, D.D., Myers, R.C., and Heremans, J.P., “Spin-Seebeck effect: A Phonon Driven Spin Distribution” *Phys. Rev. Lett.* **106** 186601, 2011.
8. Jaworski, C.M., Yang, J., Mack, S., Awschalom, D.D., Heremans, J.P., and Myers, R.C., “Observation of the spin-Seebeck effect in a ferromagnetic semiconductor” *Nature Materials*, **9**, 898, 2010.
9. Jaworski, C.M., Kulbachinskii, V., Heremans, J.P., “Resonant level formed by tin in  $\text{Bi}_2\text{Te}_3$  and the enhancement of room-temperature thermoelectric power”, *Phys. Rev. B* **80** 233201, 2009.
10. Jaworski, C.M., Tobola, J., Levin, E. M., Schmidt-Rohr, K., Heremans, J.P., “Antimony as an amphoteric dopant in lead telluride”, *Phys. Rev. B.* **80** 125208, 2009.

11. Masayuki, M., Nakamura, D., Hasegawa, Y., Komine, T., Taguchi, T., Nakamura, S., Jaworski, C.M., Jovovic, V., Heremans, J.P., "Mean free path limitation of thermoelectric properties of bismuth nanowire", *J. Appl. Phys.* **105**, 11, 113706. 2009.
12. Heremans, J.P., Jaworski, C.M. "Experimental study of the thermoelectric power factor enhancement in composites", *Appl. Phys. Lett.* **93** 122107, 2008.
13. Sootsman, J., Jovovic, V., Jaworski, C.M., Heremans, J. He, J., Dravid, V., Kanatzidis, M., "Understanding Electrical Transport and the Large Power Factor Enhancements in Co-Nanostructured PbTe", Proceedings of the Material Research Society, Spring Meeting 2009
14. Headings, L., Washington, G., Jaworski, C.M., "Thermoelectrics as elements of hybrid-electric vehicle thermal energy systems", Proc of the SPIE, the International society for Optical Engineering, Vol. 6930 2008
15. Headings L., Jaworski C., Heremans J., Guezennec Y., Rizzoni G., Washington, Marano V. "Opportunities for Thermoelectric Energy Conversion in Hybrid Vehicles", Proc. of IMECE 2006 ASME International Mechanical Engineering Congress and Exposition, IMECHE2006-15085 2006.

## Table of Contents

|  |             |
|--|-------------|
| <b>Abstract</b> .....  | <b>ii</b>   |
| <b>Acknowledgments</b> .....                                 | <b>iv</b>   |
| <b>Vita</b> .....  | <b>v</b>    |
| <b>Publications</b> .....                                    | <b>vi</b>   |
| <b>Table of Contents</b> .....                               | <b>viii</b> |
| <b>List of Figures</b> .....                                 | <b>x</b>    |
| <b>List of Tables</b> .....                                  | <b>xiv</b>  |
| <b>Chapter 1: Introduction</b> .....                         | <b>1</b>    |
| Overview .....   | 1           |
| Thermoelectric Device Efficiency .....                       | 4           |
| State of the Art Thermoelectric Materials .....              | 6           |
| <b>Chapter 2: Condensed Matter Physics</b> .....             | <b>10</b>   |
| Introduction to Electron Transport .....                     | 10          |
| Crystal Lattices & Electronic Band Structure .....           | 15          |
| Magnetic Ordering .....                                      | 25          |
| Thermal Conductivity .....                                   | 30          |
| Lattice Thermal Conductivity .....                           | 32          |
| Phonon Drag .....  | 35          |
| Galvanomagnetic and Thermomagnetic Effects .....             | 37          |
| Hall Effect and Hall Prefactor .....                         | 39          |
| Shubnikov – de Haas (SdH) Oscillations .....                 | 42          |
| <b>Chapter 3: Experimental Techniques</b> .....              | <b>48</b>   |
| Thermoelectric Methods .....                                 | 48          |
| Spin-Seebeck Effect Methods .....                            | 52          |
| <b>Chapter 4: Lead Chalcogenides</b> .....                   | <b>56</b>   |
| General Properties .....                                     | 56          |
| Electronic Band Structure Fits .....                         | 58          |
| Doping PbTe with Aluminum .....                              | 60          |
| PbTe: Upper/Lower Valence Bands Temperature Dependence ..... | 65          |

|   |            |
|---|------------|
| PbTe-PbS: Tl.....   | 70         |
| PbTe-PbS: Na.....   | 84         |
| <b>Chapter 5: Spin-Seebeck Effect in Semiconductors.....</b>        | <b>95</b>  |
| Gallium Manganese Arsenide .....                                    | 95         |
| Material Background .....   | 95         |
| Temperature and Positional Dependence .....                         | 98         |
| Scratch Test .....  | 105        |
| Point Contacts: Nernst Effect .....                                 | 107        |
| Substrate Thermal Conductivity and Low Temperature .....            | 112        |
| Theory of Spin-Seebeck Effect in Ferromagnetic Semiconductors ..... | 118        |
| Indium Antimonide: A Non-magnetic Material.....                     | 124        |
| Material Background .....   | 125        |
| Control Tests.....  | 128        |
| Spin-Seebeck Effect .....   | 133        |
| Mechanism of Non-magnetic Spin-Seebeck Effect.....                  | 137        |
| <b>Conclusions.....</b>   | <b>141</b> |
| <b>References.....</b>  | <b>142</b> |

## List of Figures

|  |    |
|--|----|
| Figure 1: Thermally generated charge separation is the charge Seebeck effect. Schematic is depicted for a p-type semiconductor. ....   | 1  |
| Figure 2: Thermally generated spin distribution is the spin-Seebeck effect.....  | 2  |
| Figure 3: Schematic of typical TE generator with p-type and n-type legs connected thermally in parallel and electrically in series with a load resistor. ....  | 4  |
| Figure 4: Fermi-Dirac statistics at various temperatures, density of states $g(\epsilon)$ both parabolic and non-parabolic bands, the occupation of the bands at various temperatures for parabolic bands, and the comparison between band nonparabolicity. ....   | 22 |
| Figure 5: Left: density of states of parabolic band and a band with a resonant level. Right: energy dispersion relation for the valence band of PbTe:Tl alloys. The Tl level creates a distortion at the top of the UVB in this case. ....   | 24 |
| Figure 6: Ground state versus spin wave for Heisenberg ferromagnet.....  | 30 |
| Figure 7: Schematic of the Normal and Umklapp processes. Normal are additive – leading to an infinite $\kappa$ . Umklapp are resistive, and result in a finite $\kappa$ . High temperature $\kappa$ decreases as additional higher energy phonon modes are populated, thus allowing for additional Umklapp scattering processes..... | 33 |
| Figure 8: Schematic of the dispersion curves for a crystal showing both acoustic and optical phonon modes. In this figure we assume the longitudinal and transverse modes have the same dispersion and the crystal has two types of ions that have a mass ratio of 2. ....   | 34 |
| Figure 9: Thermal conductivity and specific heat for a GaAs bulk sample.....   | 35 |
| Figure 10: Schematic of measurement geometry in cryostat of the four measured properties: electrical resistivity, Hall coefficient, Seebeck and Nernst-Ettingshausen coefficients that are the standard measurements performed. ....   | 37 |
| Figure 11: Schematics of the Hall, Nernst, and Righi-Leduc effects .....   | 39 |
| Figure 12: Variation of Fermi surface in a quantizing magnetic field.....  | 43 |
| Figure 13: a) Electrical resistivity of a sample as a function of magnetic field at low T showing clear oscillations. b) trace in (a) with parabolic background subtracted. c) inverse Fourier transform of data in b) vs $1/B$ . with a maximum $\sim 1.15T^{-1}$ .....   | 46 |
| Figure 14: Schematic of the inverse spin Hall effect. The ferromagnet (FM) inject spin into the normal metal (Pt). The spin current is deflected preferentially via skew scattering or side jump, and results in a transverse flow of charge. In open circuit conditions, this creates an electric field $E_{ISHE}$ .....            | 47 |

|  |    |
|--|----|
| Figure 15: Measurement schematic in home built cryostats.....  | 50 |
| Figure 16: Measurement setup in the Thermal Transport Option.....  | 51 |
| Figure 17: Measurement setup for spin-Seebeck experiments. Not to scale. Voltages shown for ferromagnets. ....   | 53 |
| Figure 18: $\alpha$ , $\rho$ , $N$ , and $n$ of $\text{Pb}_{1-x}\text{Al}_x\text{Te}$ . The inset shows the carrier concentration from Hall measurements as a function of nominal Al concentration. Symbols are experimental points; lines are added to guide the eye. ....  | 61 |
| Figure 19: Pisarenko plot for $\text{Pb}_{1-x}\text{Al}_x\text{Te}$ . Symbols are experimental points, the solid line is calculated for the lowest conduction band in PbTe.....  | 63 |
| Figure 20: Effective mass, Fermi level and scattering parameter for $\text{Pb}_{1-x}\text{Al}_x\text{Te}$ .....  | 64 |
| Figure 21: (left panel) Proposed band structure of PbTe based on contradicting literature and UVB hole density availability for the two $\Delta\varepsilon_v(T)$ . (right panel) The curves are the number of holes in the UVB at the location where $E_F$ crosses into the LVB. ....  | 67 |
| Figure 22: $\alpha$ , $\rho$ , $N$ , and $\text{RH}$ of $\text{Pb}_{0.98}\text{Tl}_{0.02}\text{Te}_{1-x}\text{S}_x$ . The inset shows the carrier concentration from Hall measurements as a function of nominal Al concentration. Symbols are experimental points; lines are added to guide the eye. ....  | 73 |
| Figure 23: Pisarenko relation for PbTe-S with Tl. The UVB and LVB lines are calculated for the upper and lower valence bands of PbTe.....  | 74 |
| Figure 24: Thermal conductivity and $zT$ of PbTeS:Tl alloys. ....  | 77 |
| Figure 25: Density of states ( $g(\varepsilon)$ ) of PbTeS-PbTeSe doped with Tl. ....  | 79 |
| Figure 26: Hall resistances as a function of magnetic field for $\text{Pb}_{0.99}\text{Na}_{0.01}\text{Te}_{1-x}\text{S}_x$ .....  | 85 |
| Figure 27: Calculated photo-excited electron density (Eq. 91) vs. temperature and calculated thermally excited electron density at various temperature as a function of hole carrier density.....  | 87 |
| Figure 28: Low temperature electrical properties of 1% Na doped samples. a) Seebeck coefficient, b) Nernst coefficient, c) electrical resistivity, and d) Hall coefficient from 2-420 K The symbols are experimental points; the lines are added to guide the eye. ....  | 88 |
| Figure 29: Low temperature electrical properties of 8% S samples with different dopant concentrations. a) Hall coefficient b) Nernst coefficient c) and d) Seebeck coefficient in 0, 7T external field for 8% S and various [Na]. The symbols are experimental points; the lines are added to guide the eye. ....  | 92 |
| Figure 30: Seebeck coefficient, electrical resistivity, thermal conductivity and $zT$ for samples with [Na] = 0.01. The symbols are experimental points; the lines are added to guide the eye. ....  | 93 |
| Figure 31: Measurement schematic and raw voltage traces in two different crystallographic directions. <b>a</b> , Measurement geometry (not to scale). <b>b</b> , Crystal directions in GaMnAs. <b>c</b> and <b>d</b> , Magnetization, $\mathbf{M}$ , as a function of applied magnetic field, $\mathbf{B}$ oriented along the easy $[1\bar{1}0]$ , $[100]$ , and hard $[110]$ axes. <b>e</b> and <b>f</b> , Transverse |    |

|   |     |
|---|-----|
| voltage, $V_y$ as a function of $\mathbf{B}$ , along the easy $[1\bar{1}0]$ and hard $[110]$ axes with an applied $\Delta T_x$ of 1.77 K and 3.13 K, respectively. Data are shown on strips near the hot and cold ends of the sample.....   | 99  |
| Figure 32: $\Delta V_y$ vs $\Delta T_x$ shows linear behavior at 6 different $\Delta T$ values on all nine strips, and $\Delta V_y=0$ at zero gradient.....   | 100 |
| Figure 33: a) Positional dependence of $S_{xy}$ at various temperatures. $S_{xy}$ varies via a $\sinh(x-L/2)$ around the midpoint of the sample. b) Normalized $S_{xy}$ at various temperatures. $S_{xy}$ at each strip has been divided by the maximum $S_{xy}$ at each respective temperature. ....   | 101 |
| Figure 34: a) Temperature dependence of various Pt strips across the GaMnAs sample. b) Magnetization showing ferromagnetic behavior and thermopower $\alpha_{xx}$ .....   | 103 |
| Figure 35: Repeat of spin-Seebeck effect in a 2 <sup>nd</sup> GaMnAs sample. Data was measured on a thin film GaMnAs sample on a GaAs wafer with in-plane magnetization and $s=0.16$ . <b>a</b> , $S_{xy}$ as a function of temperature for three Pt strips. Strip 1 is at the hot end, strips 2 and 3 are centered around the midpoint of the sample. <b>b</b> , $\Delta T_x$ vs. $\Delta V_y$ at $T\sim 98\text{K}$ <b>c</b> , Raw traces with background voltages subtracted.....  | 104 |
| Figure 36: Severance of electrical communication: the scratch test.....   | 106 |
| Figure 37: Repeat of scratch test and the spin-Seebeck effect's dependence on temperature gradient. <b>a</b> , Schematic for Case 1 (intact sample), Case 2 (sample was shortened 15% and a strip of GaMnAs was scratched away from the center of the sample), Case 3 (a second scratch was added). <b>b</b> , $V_y$ was recorded during hysteresis loops from the hot-side contact before and after each scratch. $V_y$ was normalized by the temperature gradient, which changed in each case. <b>c</b> , Spin-Seebeck coefficient. ....  | 107 |
| Figure 38: Spin-Seebeck in GaMnAs mixed with planar/anomalous Nernst effect. Point contacts were used as shown in the schematic (not to scale) with $x // [1\bar{1}0]$ . <b>a</b> , Transverse voltage, $V_y$ as a function of applied magnetic field, $\mathbf{B}$ at the hot and cold ends of the sample with an applied $\Delta T_x$ of 0.67 K. <b>b</b> , The change in transverse voltage, $\Delta V_y$ as a function of the applied thermal gradient, $\Delta T_x$ , for strips along the length of sample. <b>c</b> , $S\alpha_{xy}$ as a function of the sample temperature for differently positioned contacts. Inset plots the spatial dependence of $S\alpha_{xy}$ at a selected temperature. .... | 109 |
| Figure 39: Measurements with out-of-plane magnetization. a, Sample layout (not to scale). Strained GaMnAs on InGaAs results in an out-of-plane magnetic easy axis $[001]$ . b, Out-of-plane magnetization, $M$ as a function of magnetic field, $B$ . c, Transverse voltage, $V_y$ versus $B_{001}$ measured on point contacts (the transverse Nernst-Ettingshausen effect) and on strip contacts with $B$ 6° tilted from the $xy$ -plane. ....   | 111 |
| Figure 40: Nernst coefficient versus temperature. Point contact #1 is at the hot end, and the numbers monotonically increase toward the cold end. The insets include a schematic of the Nernst effect field and flux directions, as well as a schematic (not to scale) of the sample measured in this study. The externally applied magnetic field is approximately 6° off the $xy$ -plane. ....  | 112 |

|  |     |
|--|-----|
| Figure 41: Thermal properties of one GaMnAs/GaAs sample versus temperature. (a) Magnetization of the GaMnAs and substrate (GaAs) thermal conductivity. The inset shows the substrate specific heat. (b) Spin-Seebeck coefficient $S_{xy}$ of the GaMnAs. (c) Thermopower $\alpha_{xx}$ of the sample (green stars) and of a similar sample (purple dots). The vertical dashed lines divide the figure into four ranges. Fits described in the text. ....     | 116 |
| Figure 42: a) spin Seebeck coefficient and thermal conductivity and b) thermopower on high thermal conductivity GaAs substrate. ....   | 118 |
| Figure 43: Spin-Seebeck effect shows odd hysteric behavior in ferromagnets. Temperature profile of phonons and magnons. The $T$ difference between phonons and magnons act as a driving force. Cartoon showing the effect of phonon drag on the magnetic moment $M_x$ in each region. Change in $M_x$ due to phonon drag across the temperature gradient. Schematic hysteresis loops representing the voltage detected on the Pt strips in each region. .... | 123 |
| Figure 44: a) Pt-InSb interface is p-type near the InSb surface with a small depletion region. b) Fan chart for InSb and calculated $\epsilon_F$ calculated relative to mid-gap. The data shown in this figure was calculated by Roberto Myers (a) and Joseph Heremans (b). ..   | 128 |
| Figure 45: Galvanomagnetic properties of InSb. $\rho(T)$ showing the band gap at higher temperatures. ....   | 129 |
| Figure 46: Thermomagnetic properties of InSb. (a) thermopower $\alpha_{xxx}(T)$ with $B_x // \nabla_x T$ at $B_x=0.7T$ . Schematic (not to scale) of In point contacts on InSb. (b) $\alpha_{yxx}(B)$ most likely resulting from a small parasitic $\nabla_{y,z} T$ and misalignments in Cu contact placement along $x$ . (c) $\alpha_{xxx}(B)$ has oscillations at low $B$ . ....   | 130 |
| Figure 47: Thermomagnetic properties with $B$ oriented along the $z$ -axis. (a) and (b) are transverse magnetothermopower, and are even in $B$ . (c) and (d) are conventional Nernst effect. ....  | 132 |
| Figure 48: Experimental data on the spin-Seebeck effect in InSb. $S_{xy}(B_x)$ on 1 <sup>st</sup> InSb sample. ....  | 134 |
| Figure 49: Even part of spin-Seebeck at various temperature gradients on second InSb sample. Magnitude of $\Delta V_y$ scales linearly with $\Delta T_x$ . ....  | 135 |
| Figure 50: Spin-Seebeck effect in InSb on a 2 <sup>nd</sup> sample. ....   | 135 |
| Figure 51: Maximum of $S_{xy}$ on the cold Pt bar in sample 1 in Figure 48. ....   | 137 |
| Figure 52: Explanation of spin-Seebeck effect mechanism in InSb. ....  | 138 |

## List of Tables

|  |     |
|--|-----|
| Table 1: Fermi level, effective mass, scattering parameter, and density of states of TI doped $\text{PbTe}_{1-x}\text{S}_x$ . .....                          | 76  |
| Table 2. Comparison between nominal sodium composition and measured Hall coefficients in $\text{Pb}_{1-y}\text{Na}_y\text{Te}_{0.92}\text{S}_{0.08}$ . ..... | 92  |
| Table 3 Fitting parameters for experimental data in Figure 33 to Eq. 93. ....  | 101 |

## Chapter 1: Introduction

### Overview

Thomas Seebeck in 1821 discovered that conductors, when subjected to a temperature gradient, generated a voltage. This effect has been termed Seebeck effect after its founder, and is also called thermopower. It is this generation of a voltage that allows for the generation of electric power from thermal power, as depicted in Figure 1 and is given:

$$\alpha \equiv \frac{E}{\nabla T} = \frac{\Delta V}{\Delta T}, \quad (1)$$

where  $\alpha$  is the charge Seebeck coefficient, or thermopower,  $E$  is the induced electric field,  $\nabla T$  is the imposed temperature gradient, and  $\Delta V$ ,  $\Delta T$  are the measurable temperature and voltage differences. On a high level, this occurs because of a redistribution of electrons/holes under a temperature gradient ( $\nabla T$ ).

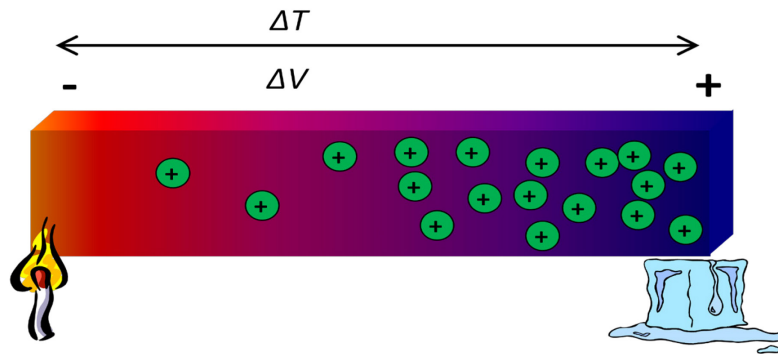


Figure 1: Thermally generated charge separation is the charge Seebeck effect. Schematic is depicted for a p-type semiconductor.

In 2008, K. Uchida & E. Saitoh reported the first measurements of the spin-Seebeck effect<sup>1</sup>, which consists of a redistribution of spins in a material subjected to a  $\nabla T$  as shown in Figure 2. By using the inverse spin Hall effect (ISHE) in a non-magnetic metal (Platinum), this spin distribution is converted into an electric field, which is then measured. As the net sign of the summation of spins is different on the two halves of the sample, one side has more spin up, the other more spin down, thus the ISHE generated electric field in adjacent Pt strips will have opposing signs for the two ends.

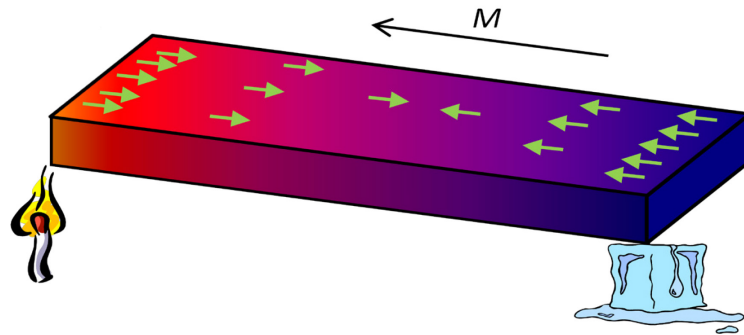


Figure 2: Thermally generated spin distribution is the spin-Seebeck effect.

Through the ISHE, a voltage is generated, thus allowing usage of thermospin materials for waste heat recovery. However, unlike in thermoelectrics, the material parameters governing the figure of merit are decoupled, thus allowing for potentially high efficient thermospin generators.<sup>2</sup>

While the previously mentioned high level explanation for the charge Seebeck effect explains why n-type and p-type materials will have opposing signs of the Seebeck effect,

it lacks many of the subtleties and nuances that give rise to the magnitude of the voltage generated. Host band structure including degree of non-parabolicity, band degeneracy, temperature, extrinsic and intrinsic conduction, energy gap, doping levels and designed modifications of the band structure are all factors in the final magnitude of the charge Seebeck voltage

Likewise, while only 4 years old, we have begun to explore the origin and subtleties of the spin-Seebeck effect. We first discovered that we can sever electrical communication between the material being studied, leaving only the substrate, and the spin-Seebeck generated voltage remains unaffected.<sup>3</sup> Uchida took this further and showed that conducting electrons are not needed at all, by observing the spin-Seebeck effect in YIG ( $\text{Y}_3\text{Fe}_5\text{O}_{12}$ ), an insulator.<sup>4</sup> We measured that the positional dependence of the spin-distribution is a  $\sinh(x)$  around the midpoint of the sample, which is reminiscent of the magnon-phonon temperature difference in a crystal under a  $\nabla T$ .<sup>5</sup> We further showed that the magnitude of the distribution is not only a function of net magnetization of the sample, but depends greatly on the thermal conductivity of the substrate.

New energy conversion device possibilities exist for spin-Seebeck effect based systems as all solid-state conversion technologies along the lines of current thermoelectric devices. Critically, the optimization of the efficiency of thermoelectric materials involves reaching a compromise between mutually counter-indicated properties (thermopower, electrical and thermal conductivities) of a single material. In contrast, the spin-Seebeck effect involves properties (phonon-spin interactions, spin orbit interactions) of at least two different materials that can be optimized independently.

## Thermoelectric Device Efficiency

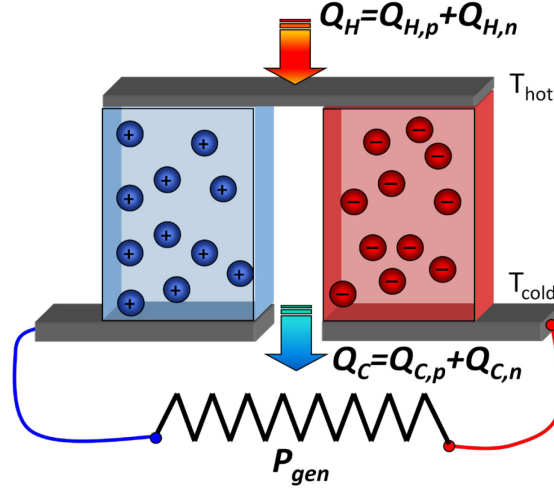


Figure 3: Schematic of typical TE generator with p-type and n-type legs connected thermally in parallel and electrically in series with a load resistor.

Figure 3 shows a typical p-n TE segment in generation mode. A thermodynamic analysis of the hot junction ignoring contact losses yields:

$$Q_H = Q_{H,p} + Q_{H,n} = \left( \kappa_p \frac{A_p}{L_p} + \kappa_n \frac{A_n}{L_n} \right) (T_H - T_C) + (\alpha_p - \alpha_n) T_H I - \frac{I^2}{2} \left( \rho_p \frac{L_p}{A_p} + \rho_n \frac{L_n}{A_n} \right) \quad (2)$$

Where  $A_p$ ,  $L_p$ ,  $A_n$ ,  $L_n$  are the areas and lengths of the p-type and n-type legs, respectively.  $\alpha_p$ ,  $\alpha_n$ ,  $\kappa_p$ ,  $\kappa_n$  and  $\rho_p$ ,  $\rho_n$  are the Seebeck coefficient, thermal conductivities and electrical resistivity of the legs.  $T_H$  and  $T_C$  are the hot and cold temperatures, while  $I$  is the current passing through the legs. As the material properties are temperature dependant, it is necessary to integrate the material properties over temperature. The first term on the right hand side arises from the thermal conductivity of the legs. The second is the Peltier heat and the third is Joule heat. The Peltier term has  $T_H$  as this is the temperature at which the

heat is evolved and the  $\frac{1}{2}$  in the Joule term occurs because only half of the Joule heat will travel towards the hot side. Setting  $A_p=A_n$  and  $L_p=L_n$  as is typical of commercial thermoelectric modules simplifies the equation:

$$Q_H = Q_{H,p} + Q_{H,n} = (K_p + K_n)(T_H - T_C) + (\alpha_p - \alpha_n)T_H I - \frac{I^2}{2}(R_p + R_n) \quad (3)$$

Where  $K$  and  $R$  are defined as the total thermal conductance and electrical resistance of the leg. Analysis of the cold junction yields:

$$Q_C = Q_{C,p} + Q_{C,n} = (K_p + K_n)(T_H - T_C) + (\alpha_p - \alpha_n)T_C I + \frac{I^2}{2}(R_p + R_n) \quad (4)$$

The significant differences in this equation are  $T_C$  in the Peltier term, and the additive Joule heat. This heat is deleterious to  $COP$  in cooling operation, but additive in heating mode. Generated power is simply  $P_{gen}=I^2 R_{load}$ , where  $R_{load}=R_N+R_P$  for maximum power. Thermal efficiency at maximum power follows:

$$\eta = \frac{P_{gen}}{Q_H} = \frac{I^2 R_{load}}{K\Delta T + \alpha T_H I + \frac{1}{2} I^2 R_{load}} = \frac{\Delta T}{T_H} \frac{\sqrt{1 + \left(\frac{\alpha^2 \sigma}{\kappa} T\right)} - 1}{\sqrt{1 + \left(\frac{\alpha^2 \sigma}{\kappa} T\right)} + T_H / T_C} \quad (5)$$

$$\eta = \frac{\Delta T}{T_H} \frac{\sqrt{1 + (zT)} - 1}{\sqrt{1 + (zT)} + T_H / T_C}$$

Where  $\alpha = \alpha_p - \alpha_n$ ,  $K = K_p + K_n$ , and  $zT$  is termed the dimensionless thermoelectric figure of merit:

$$zT = \frac{\alpha^2 \sigma}{\kappa} T = \frac{\alpha^2}{\rho \kappa} T \quad (6)$$

One can also express this using  $R$  and  $K$  in place of  $\sigma$  and  $\kappa$ . It is now clear why the parameter  $z$  and  $zT$  are useful in evaluating thermoelectric materials. Furthermore, we see the Carnot efficiency  $\Delta T/T_H$  in this equation, thus total efficiency is a function of only  $zT$  and  $T_H, T_C$ . A  $zT$  of 1 gives about 12% efficiency, while a  $zT=2$  reaches about 18% efficiency with  $T_H=773\text{K}, T_C=363\text{K}$ .

Contact resistances, both thermal ( $K_c$ ) and electrical ( $R_c$ ) lower the efficiency of a device built from thermoelectric elements. This is usually called device  $ZT$ .

$$ZT = \frac{\alpha^2}{(R + R_c)(K + K_c)} T \quad (7)$$

This creates an optimal A-L ratio for the legs of the module, as one does not want contact resistance to dominate the device efficiency as will occur in devices built with thin-film thermoelectric materials. It is this reason that researchers are trying to extend the gains in  $zT$  in thin-film materials (see next section) to bulk solids.

## State of the Art Thermoelectric Materials

The ‘historically’ best thermoelectrics have had peak  $zT \leq 1$  and can be divided into different operating temperatures and thus different applications.<sup>6</sup> Below 300K,  $\text{Bi}_{1-x}\text{Sb}_x$  with  $x \sim 0.12$  alloys are the best n-type materials and can be used for cryogenic cooling. No good p-type BiSb alloy currently exists: the best p-type reported to date has a  $zT \sim 0.12$  and was work done by H. Jin and myself<sup>7</sup>.  $(\text{Bi}_{1-x}\text{Sb}_x)_2(\text{Te}_{1-x}\text{Se}_x)_3$  both p-type and n-type at  $250 < T < 473\text{K}$  are used both in Peltier cooling for refrigeration and the cold end

of waste heat recovery systems and an increase to  $zT \sim 1.4$  was shown by nanostructuring<sup>8</sup>. TAGS, a  $(\text{GeTe})_{1-x}(\text{AgSbTe}_2)_x$  alloy with  $x \sim 0.15$  is the best p-type in the 600-900K,<sup>9</sup> but cannot cycle due to a phase transition, and is only usable in radioisotope thermoelectric generators in space. PbTe both n-type and p-type thus finds usage in the 500-800K waste heat recovery. At 1000K or above, SiGe alloys, both n-type and p-type are used in the hot side of the radioisotope TE generators. Other classes of materials are the skutterudite alloys such as  $\text{CoSb}_3$ , half-Heusler alloys including  $\text{Hf}_{0.75}\text{Zr}_{0.25}\text{NiSn}$ , and Zintl compounds –  $\text{Yb}_{14}\text{MnSb}_{11}$ .<sup>9</sup>

Nanostructured materials have been the focus of much research in the past decade since the publication of reports of  $zT > 2$  on thin films of PbTe/PbSe<sup>10</sup> and  $\text{Bi}_2\text{Te}_3\text{-Sb}_2\text{Te}_3$ <sup>11</sup> superlattices at room temperature. However, the PbTe/PbSe superlattices had a mistake in the Hall measurements<sup>12</sup> and the large thermal conductivity reduction did not repeat.<sup>13</sup>  $\text{AgPb}_x\text{SbTe}_{2+x}$  was the first report on bulk nanostructured material with  $zT > 2$ <sup>14</sup> at 800K. Attempts at device fabrication with this material were unsuccessful due to the presence of the 2<sup>nd</sup> phase,  $\text{Ag}_2\text{Te}$ , which has phase transition at 145°C.<sup>15</sup> After  $\text{AgPb}_x\text{SbTe}_{2+x}$ , numerous alloys with nanostructures were synthesized that all had peak  $zT$  around 1.5<sup>16</sup> at 600-800K. As the lowest thermal conductivity that can be reached is the amorphous limit (for  $\sim\text{PbTe}$  0.3 W/m K), this nano-structuring technique appears to have saturated the increase in  $zT$ . Furthermore, one must choose nanostructures that are energetically favorable at elevated temperatures, lest they dissolve. Therefore, the increase in power factor and thus  $zT$  seen with resonant levels<sup>37</sup> in PbTe doped with Tl opened another opportunity for increasing  $zT$ . We explore an alloy of PbTe:Tl in this dissertation.

A new method that has attracted a renewed interest over the past several years is based upon that of AgSbTe<sub>2</sub><sup>17</sup>. The Sb has an unbounded electron pair that creates extremely non-harmonic behavior in the crystal lattice and inhibits phonon propagation through the lattice to that near the minimal value. This has been extended to other I-V-VI compounds such as NaSbSe<sub>2</sub> and NaBiTe<sub>2</sub>.<sup>18</sup>

There are several general rules that one follows when designing thermoelectric materials. First, materials comprised of heavy atoms are useful because of an increased spin orbit interaction that leads to a decreased band gap to that useful to thermoelectricity, approximately 200 meV at 300K. Also, heavier atoms have a lower specific heat, thus leading to lower thermal conductivities. Second, the material must be doped appropriately which results in most TE materials being doped narrow gap semiconductors. Isoelectronic alloy scattering is another technique that must be utilized intelligently. The electronegativities of the elements must be close to minimize electron scattering. This occurs with Te & Se, and Bi & Sb.

Deriving the power factor from  $\sigma = pe\mu = Np_p e^2 \frac{\tau}{m_p^*}$  for a system with a degeneracy of pockets  $N$  where  $m_p^*$  is the mass of the pocket,

$$PF = S^2\sigma = \frac{m_d^*}{p^{1/3}} \frac{64\pi^{16/3} k_B^4 T^2 \tau}{3^{10/3} h^4} = N \frac{m_p^*}{p_p^{1/3}} \frac{64\pi^{16/3} k_B^4 T^2 \tau}{3^{10/3} h^4} \propto N \sqrt{m_p^*} \quad (8)$$

shows that PF scales linearly with  $N$  in contrast to  $m_D^*$ , which scales with  $N^{2/3}$ . Obtaining a high  $m_D^*$  through a multiply-degenerate Fermi surface is more effective than using a single heavy mass band, as in resonant levels. The main cause for this is the fact that the

mobility scales inversely with the band mass  $m_p^*$ , not with the total  $m_D^*$ . High degeneracy may be innate to the material, as with PbTe and Bi<sub>2</sub>Te<sub>3</sub>, and it can be enhanced by appropriate alloying. Examples<sup>19,20</sup> where this occurs are Bi<sub>2-x</sub>Sb<sub>x</sub>Te<sub>3</sub> and Bi<sub>2</sub>Te<sub>3-y</sub>Se<sub>y</sub>.

## Chapter 2: Condensed Matter Physics

The notation used for a transport coefficient in a magnetic field has three indices. The convention used here is as follows: the first index  $1$  denotes the direction of the applied flux, electrical ( $j$ ) or thermal current density ( $\dot{Q}$ ); the second index  $2$  denotes the direction of the measured potential ( $V$ ), and the third index  $3$  denotes the direction of the applied magnetic field. For example, a  $\dot{Q}_x$  and resulting  $\nabla T_x$  give rise to a longitudinal voltage  $V_x$ . This potential, divided by the length  $L$  of the sample, gives an electric field  $E_x = V_x/L$ . In the presence of a magnetic field  $B_z$  aligned along the  $z$ -axis, also a transverse voltage  $V_y$  and a transverse electric field  $E_y = V_y/W$  arise. The ratio of fields and fluxes give then the transport coefficients indicated. Thus, a measurement of the transverse magnetothermopower is demarcated  $\alpha_{xxz}$  while Nernst-Ettingshausen thermopower is  $\alpha_{xyz}$ . Similarly, longitudinal magnetoresistivity is:  $\rho_{xxx} \equiv E_x/j_x(B_x)$ .

### Introduction to Electron Transport

In this section we derive several phenomena using the relaxation time approximation. While this approximation simplifies the probability matrix  $W_{k,k'}$  associated with scattering as well as availability of both states to scatter into and out of, it is very didactic in nature and helps to understand the origins of electronic conductivity, electronic thermal conductivity, Seebeck, and Peltier effects.

I first begin with the Boltzmann equation in magnetic field  $\mathbf{H}$  using semiclassical electron dynamics<sup>21</sup>:

$$\frac{\partial g}{\partial t} + \mathbf{v} \cdot \nabla_{\mathbf{r}} g + -q(\mathbf{E} + \mathbf{v} \times \mathbf{H}) \cdot \frac{1}{\hbar} \nabla_{\mathbf{k}} g = \left( \frac{\partial g}{\partial t} \right)_{coll} = \frac{f - g}{\tau} \quad (9)$$

Here  $-q$  (the electron charge) would be replaced by  $+q$  for holes,  $g$  is the nonequilibrium distribution function,  $\mathbf{v}$  is the electron velocity,  $\mathbf{E}$  is the electric field,  $\tau$  is the relaxation time,  $\hbar$  is the reduced Planck constant, and  $f$  is the equilibrium distribution function:

$$f = \frac{1}{e^{\frac{\varepsilon - \varepsilon_F}{k_B T}} + 1} \quad , \quad (10)$$

also known as the Fermi-Dirac distribution function.  $k_B$  is the Boltzmann constant,  $\varepsilon$  is the electron energy, and  $\varepsilon_F$  is the Fermi level. For a free electron  $\varepsilon(\mathbf{k}) = \hbar^2 \mathbf{k}^2 / 2m$ , where  $\mathbf{k}$  is the electron wavevector:  $k=2\pi/\lambda$ , where  $\lambda$  is the electron wavelength. Further, the electron velocity  $\mathbf{v}$  is:  $\mathbf{v} = \hbar \mathbf{k} / m$ . Eq. 10 describes the distribution of the energies of particles in a many-particle system that obey the Pauli Exclusion Principle, or that no two particles can occupy the same energy state. Often,  $\mathbf{H}=0$ , and thus we will drop this term subsequently.  $\mathbf{H} \neq 0$  leads to effects such as the Hall and Nernst effects. In steady state with weak and spatially uniform temperature gradients and electric fields,  $\partial g / \partial t$  is much smaller than its derivative in space, thus  $\partial g / \partial t \approx 0$ . We further assume an energy dependent relaxation time where the scattering probability  $W_{\mathbf{k}, \mathbf{k}} \sim e^{-t/t_0} / \tau(\mathbf{k})$ . Here,  $\tau = \tau$

$(\varepsilon(\mathbf{k}))$ , but henceforth will be written as  $\tau$  for clarity. These approximations lead to a static nonequilibrium distribution function:

$$g = f + \left( -\frac{\partial f}{\partial \varepsilon} \right) \tau \times \mathbf{v}(\mathbf{k}) \cdot \left( -q\mathbf{E} - \nabla E_F - \frac{\varepsilon(\mathbf{k}) - \mu}{T} \nabla T \right). \quad (11)$$

The electric current density is the integral over the phase space of the electronic distribution function multiplied by velocity:

$$\mathbf{j}^q = -q \int \frac{\mathbf{v}(\mathbf{k}) g}{4\pi^3} D(\mathbf{k}) d\mathbf{k}. \quad (12)$$

Where a  $D(\mathbf{k})$  has been added as the density of available states between  $\mathbf{k}$  and  $\mathbf{k} + d\mathbf{k}$ .

Defining  $\boldsymbol{\sigma}$  as the conductivity tensor  $\mathbf{j}^q = \boldsymbol{\sigma} \mathbf{E}$  it follows from Eqs. 11 & 12 that :

$$\boldsymbol{\sigma} = -\frac{q^2}{4\pi^3} \int \mathbf{v}^2(\mathbf{k}) \tau \left( -\frac{\partial f}{\partial \varepsilon} \right) D(\mathbf{k}) d\mathbf{k}. \quad (13)$$

Here, we have assumed  $\nabla T = 0$  and uniform  $\varepsilon_F$ .

As an analog, the electronic thermal conductivity is calculated with  $\mathbf{E} = 0$ . First, the number density  $\mathbf{j}^n$  is just Eq. (12) divided by  $-q$  and energy density  $\mathbf{j}^\varepsilon$  is Eq. 12 multiplied by  $-\varepsilon(\mathbf{k})$ :

$$\mathbf{j}^n = \int \frac{\mathbf{v}(\mathbf{k}) g}{4\pi^3} D(\mathbf{k}) d\mathbf{k} \quad \& \quad \mathbf{j}^\varepsilon = \int \frac{\mathbf{v}(\mathbf{k}) \varepsilon(\mathbf{k}) g}{4\pi^3} D(\mathbf{k}) d\mathbf{k} \quad (14)$$

The thermal current density follows using the 2<sup>nd</sup> law of thermodynamics:

$$\mathbf{j}^t = \frac{1}{4\pi^3} \int \mathbf{v}(\mathbf{k}) [\varepsilon(\mathbf{k}) - \varepsilon_F] g D(\mathbf{k}) d\mathbf{k} \quad (15)$$

Here  $g$  is as defined in Eq. 11 with both nonzero  $\mathbf{E}$  and  $\nabla T$ . The nonzero  $\mathbf{E}$  arising from  $\nabla T$  is known as the Seebeck effect. Eq. 15 includes the Peltier effect, a heat transport possible under zero  $\nabla T$ .

Combining Eqs. 12 & 15 leads to coupled equations which are an example of the Onsager reciprocal relations:<sup>22</sup>

$$\begin{pmatrix} \mathbf{j}^q \\ \mathbf{j}^t \end{pmatrix} = \begin{pmatrix} L_{11} & L_{12} \\ L_{21} & L_{22} \end{pmatrix} \begin{pmatrix} E \\ -\nabla T \end{pmatrix} = \begin{pmatrix} L_{ee} & L_{eq} \\ L_{qe} & L_{qq} \end{pmatrix} \begin{pmatrix} E \\ -\nabla T \end{pmatrix}. \quad (16)$$

Where the L's are defined:

$$L_{11} = \frac{q^2}{4\pi^3} \int \left( -\frac{\partial f}{\partial \varepsilon} \right) \tau \mathbf{v}^2(\mathbf{k}) D(\mathbf{k}) d\mathbf{k} \quad (17)$$

$$L_{12} = \frac{q}{4\pi^3} \int \left( -\frac{\partial f}{\partial \varepsilon} \right) \tau \mathbf{v}^2(\mathbf{k}) [\varepsilon(\mathbf{k}) - \varepsilon_F] D(\mathbf{k}) d\mathbf{k} = \frac{1}{T} L_{21} \quad (18)$$

$$L_{22} = \frac{1}{4\pi^3 T} \int \left( -\frac{\partial f}{\partial \varepsilon} \right) \tau \mathbf{v}^2(\mathbf{k}) [\varepsilon(\mathbf{k}) - \varepsilon_F]^2 D(\mathbf{k}) d\mathbf{k} \quad (19)$$

The 'e' and 'q' subscripts in Eq. 16 are included to detail another naming convention. It follows that  $L_{11} = \sigma$ , or  $\mathbf{j}^q = L_{11}\varepsilon$ . The thermal conductivity  $\kappa$  can be found by setting  $\mathbf{j}^q=0$  in Eq. 16 and solving for  $\mathbf{j}^t = \kappa \nabla T$

$$\kappa = L_{22} - \frac{L_{21}L_{12}}{L_{11}}. \quad (20)$$

Ignoring the thermoelectric effects in Eq. 20 (the 2<sup>nd</sup> term) leads us to the Wiedemann-Franz law.

$$\kappa = L_{22} = \frac{\pi^2}{3} \left( \frac{k_B}{q} \right)^2 T \sigma \quad (21)$$

This leads to the definition of the free electron Lorenz number  $L_0 = \pi^2/3 \left( \frac{k_B}{q} \right)^2$ . This number is valid in the case of purely elastic electron scattering, but varies in most

materials. Next, the Seebeck coefficient is the generated electric field under no current flow.

$$\alpha = \frac{E}{\nabla T} = \frac{L_{12}}{L_{11}}. \quad (22)$$

Lastly, the Peltier effect occurs under zero  $\nabla T$  and the Peltier coefficient  $\Pi$  follows:

$$\Pi = \frac{\mathbf{j}^t}{\mathbf{j}^q} = \frac{L_{21}}{L_{11}}. \quad (23)$$

From Eq. 18,  $L_{12}T=L_{21}$ ; the Peltier and Seebeck coefficients are related:

$$\Pi = \alpha T. \quad (24)$$

Hereafter, we perform a transformation of variable from k-space to energy space. The density of states for a 3D parabolic electron band is:

$$D(\varepsilon) = \frac{(2m^*)^{3/2}}{2\pi^2\hbar^3} \sqrt{\varepsilon - \varepsilon_0}, \quad (25)$$

where  $\varepsilon_0$  is the band edge energy and  $m$  is the electron effective mass. We will discuss electronic band structure and the implications of effective mass in detail in Chapter 4j.

$$\alpha = \frac{1}{qT} \left( \varepsilon_F - \frac{\int \left( \frac{\partial f}{\partial \varepsilon} \right) \tau \varepsilon^2 D(\varepsilon) d\varepsilon}{\int \left( \frac{\partial f}{\partial \varepsilon} \right) \tau \varepsilon D(\varepsilon) d\varepsilon} \right) \quad (26)$$

With the earlier relaxation time approximation assumption  $\tau=\tau_0\varepsilon^\lambda$  and substituting Eq. 25, Eq. 26 becomes for a 3D parabolic band:

$$\alpha = \frac{1}{qT} \left( \varepsilon_F - \frac{\int \left( \frac{\partial f}{\partial \varepsilon} \right) \varepsilon^{2+\frac{1}{2}+\lambda} d\varepsilon}{\int \left( \frac{\partial f}{\partial \varepsilon} \right) \varepsilon^{1+\frac{1}{2}+\lambda} d\varepsilon} \right) \quad (27)$$

Thus one can calculate the Seebeck coefficient for a metal given the electrochemical potential, the scattering mechanism ( $\lambda$ ), and the temperature. This equation is valid only for one band, however it can be generalized for multiband conduction. Thermopower in the high field limit ( $\mu B > 1$ ) is independent of any scattering processes.<sup>24</sup>

Next, we extend Eq. 16 to that involving spin transport, where the additional  $\mathbf{j}^s$  is the spin current.<sup>23</sup>

$$\begin{pmatrix} \mathbf{j}^q \\ \mathbf{j}^t \\ \mathbf{j}^s \end{pmatrix} = \begin{pmatrix} L_{ee} & L_{eq} & L_{es} \\ L_{qe} & L_{qq} & L_{qs} \\ L_{se} & L_{sq} & L_{ss} \end{pmatrix} \begin{pmatrix} E \\ -\nabla T \\ \nabla M \end{pmatrix} \quad (28)$$

In this case the heat, electrical transport, and heat transport are all couple quantities. This notion will be explored later in the text in the spin-Seebeck sections.

Following from Eq. 13, we can define the electron mobility:

$$\mu(E) = q \tau(E) \mathbf{m}(E)^{-1} \quad (29)$$

## Crystal Lattices & Electronic Band Structure

All of the materials that we studied in this dissertation are crystalline, that is the atoms are ordered in a period array. While they may be polycrystalline on a large scale, it is the

atomic ordering that generates the electronic and thermal properties of the solid, and therefore is of utmost importance when studying condensed matter.

Crystalline materials are characterized by a Bravais lattice, which describes how the units that comprise the periodic array are arranged. These units are not necessarily atoms; they could be groups of atoms. The Bravais lattice is all the points generated by

$$\mathbf{R} = n_1 \mathbf{a}_1 + n_2 \mathbf{a}_2 + n_3 \mathbf{a}_3 , \quad (30)$$

where  $n_j$  is an integer and  $\mathbf{a}_j$  are vectors, which are called the primitive vectors. The periodic array generated by the Bravais lattice vectors appears exactly the same from any perspective. Macroscopic crystals are large enough that the surface does not affect the periodicity created by the Bravais lattice.

Next, we define the primitive unit cell as the volume of space that just fits all of the space when the lattice points are translated through the primitive vectors in a Bravais lattice. The primitive cell does not need to be unique, but it has to contain one lattice point. The conventional unit cell, or unit cell for brevity, is typically an integer value larger than the primitive unit cell and has the required symmetry to just fill space when passed through a subset of the Bravais lattice. Another option, the Wigner-Seitz cell, is one with the complete symmetry of the Bravais lattice. It is the region of space surrounding a lattice point that is closer to that point than any other.

To describe a physical crystal, one needs both a lattice and a basis. A basis is the physical unit that is translated through the primitive vectors, thus generating a crystal structure. Of interest to us is the NaCl crystal structure, as this is how the Pb salts form.

It consists of equal numbers of Pb and Te/Se/S ions placed at alternating points of a cubic lattice. As such, each atom has 6 nearest neighbors, all of the other ion. An alternating description is two interpenetrating face centered cubic (fcc) lattices of each ion. A fcc lattice begins with simple cubic but adds lattice points centered on the faces of the cube, i.e. at  $(\frac{1}{2}, \frac{1}{2}, 0)$ ,  $(\frac{1}{2}, 0, \frac{1}{2})$ , etc. The Pb ions are centered at  $(0,0,0)$  and the Te/Se/S ions at  $(a/2)(\hat{x} + \hat{y} + \hat{z})$ .

If we consider an electron in the periodic field of a uniform crystal, the Hamiltonian:

$$H = \frac{\mathbf{p}^2}{2m} + U = \frac{\hbar^2 \mathbf{k}^2}{2m} + U, \quad (31)$$

where  $U(\mathbf{r})=U(\mathbf{r}+\mathbf{R})$  is the periodic potential that is invariant under any set of translations as dictated by all  $\mathbf{R}$  in the Bravais lattice,  $\mathbf{p}$  is the electron momentum, and  $m$  is the electron mass. The eigenstates of  $H$  are chosen to have the same form as the Bloch functions multiplied by a plane wave:

$$\psi = e^{i\mathbf{k}\cdot\mathbf{r}} u_{n\mathbf{k}}(\mathbf{r}), \quad (32)$$

where  $\mathbf{k}$  is a wavevector. And it follows from the periodicity of the lattice that

$$\psi(\mathbf{r} + \mathbf{R}) = e^{i\mathbf{k}\cdot\mathbf{R}} \psi(\mathbf{r}), \quad (33)$$

which is known as Bloch's theorem. Using the Born-von Karman (BvK) boundary conditions:  $\psi(\mathbf{r} + N_j \mathbf{a}_j) = \psi(\mathbf{r})$ , with  $j=1, 2, 3$ ,  $\mathbf{a}_j$  are the primitive vectors of the unit cell ( $\mathbf{R} = n_1 \mathbf{a}_1 + n_2 \mathbf{a}_2 + n_3 \mathbf{a}_3$ ), and  $N_j$  are all the integers such that  $N = N_1 \cdot N_2 \cdot N_3$  is the total number of primitive cells. Using Bloch's theorem and the BvK boundary conditions it follows that

$$\mathbf{k} = \sum_{j=1}^3 \frac{d_j}{N_j} \mathbf{b}_j, \quad (34)$$

where  $d$  is an integer and  $\mathbf{b}_j$  are the primitive vectors of the reciprocal lattice. Thus  $\mathbf{k}$  must be real. Furthermore, the number of allowed  $\mathbf{k}$  vectors is equal to the number of atomic sites in the crystal

The Fermi level is the highest filled energy level at the ground state ( $T=0\text{K}$ ). The representation of this in 3D is the Fermi surface; such that each electron's energy (in the free electron model)  $\varepsilon(\mathbf{k}) = \hbar^2 \mathbf{k}^2 / 2m$  is less than  $\varepsilon_F$ . In a crystal the energy levels do not follow the one-electron levels, but now fill up available energy positions as dictated by the crystal and are labeled with quantum numbers:  $n, \mathbf{k}$ .  $\varepsilon_n(\mathbf{k})$  need not follow the free electron parabolic form, and indeed may have some nonparabolicity involved.

Depending on where  $\varepsilon_F$  falls, the material is an insulator, semiconductor, or metal. If  $\varepsilon_F$  lies in one or more of the bands, causing that band(s) to be partially filled, then the material is a metal. The electrons near  $\varepsilon_F$  have available states that they can travel through. If the electrons fill up a band completely, such that there is an energy gap to the next available energy states, the material is considered insulating. Depending on the energy gap compared to 300K thermal energy ( $\sim 25 \text{ meV}$ ), the material is either an insulator (large band gap) or an intrinsic semiconductor (small band gap). It is possible through extrinsic doping to create conduction in insulators by selecting atoms with energy impurity levels that lie close to or in the energy bands. If the bands are partially filled, as in a metal at all temperatures or a semiconductor above 0K, a surface in  $\mathbf{k}$ -space arises (Fermi surface) that separates the unoccupied and occupied levels. This surface is

only sharp at 0K, at  $T > 0K$  it will have thermal smearing. It is this smearing that leads to the Seebeck effect. Filled bands are inert.

We can then derive a density of states  $g(\varepsilon)$  or DOS that is the number of available states between  $\varepsilon$  and  $\varepsilon + d\varepsilon$ , or the number of states per unit volume per unit energy. Using Eq. 31 & 34 and that the volume in k-space between two spheres  $v d\mathbf{k} = 4\pi^2 |\mathbf{k}|^2 d\mathbf{k}$  leads to a density of state in k-space:  $g(\mathbf{k}) d\mathbf{k} = |\mathbf{k}|^2 L^3 \pi^{-2} d\mathbf{k}$  where the degeneracy of 2 for spin has been added. We then rearrange the parabolic energy relation

$$\varepsilon(\mathbf{k}) = \hbar^2 \mathbf{k}^2 / 2m , \quad (35)$$

for  $\mathbf{k}$ , differentiate both sides, and substitute  $d\varepsilon$  for  $d\mathbf{k}$  to transform the DOS to energy space. In 3D this leads to:

$$g(\varepsilon) d\varepsilon = \frac{1}{2\pi^2} \left( \frac{2m_e}{\hbar^2} \right)^{3/2} \varepsilon^{1/2} d\varepsilon . \quad (36)$$

In the case of PbTe, because the small energy gap is determined by spin-orbit interactions, the highest valence band and lowest conduction band are strongly non-parabolic and follow a Dirac-like dispersion. Therefore, a correction in the parabolic energy dispersion relation (Eq. 39) is necessary:

$$\gamma(\varepsilon) = \varepsilon \left( 1 + \frac{\varepsilon}{\varepsilon_g} \right) = \hbar^2 \mathbf{k}^2 / 2m . \quad (37)$$

where  $\varepsilon_g$  is the energy gap between the highest occupied valence band and the lowest unoccupied conduction band, and is also called band gap. In the case of Pb salts with their ellipsoidal Fermi surfaces:<sup>24</sup>

$$\gamma(\varepsilon) = \varepsilon \left( 1 + \frac{\varepsilon}{\varepsilon_g} \right) = \frac{\hbar^2}{2} \left( \frac{\mathbf{k}_{\parallel}^2}{m_{\parallel}^*} + \frac{2\mathbf{k}_{\perp}^2}{m_{\perp}^*} \right), \quad (38)$$

where  $m_{\parallel}^*, m_{\perp}^*$  are the longitudinal and transverse effective masses, respectively and  $\mathbf{k}_{\parallel}, \mathbf{k}_{\perp}$  are the wave vectors.

The effective mass is a mass that governs the kinetics of the motion of the electrons or holes in the solid. Electrons/holes respond to magnetic and electric fields as if they were particles with a certain mass, which is directionally dependent.  $m^*$  is a conceptual tool used to express the reaction than an electron will give to comply with Newton's second law  $F = \hbar d\mathbf{k} / dt = Eq$ . The periodic potential and crystal structure, along with electron interactions with phonons, electrons, etc., will affect the movement of an electron. This can be seen as the inverse of the second derivative of the dispersion relation. The velocity of an electron with wave vector  $\mathbf{k}$  is proportional to the  $\nabla_{\mathbf{k}}E(\mathbf{k})$ . Taking the time derivative of  $v(\mathbf{k})$

$$\frac{\partial v(\mathbf{k})}{\partial t} = \frac{\partial}{\partial t} \left( \frac{1}{\hbar} \nabla_{\mathbf{k}} \varepsilon(\mathbf{k}) \right) = \frac{\partial \mathbf{k}}{\partial t} \frac{\partial}{\partial \mathbf{k}} \left( \frac{1}{\hbar} \frac{\partial \varepsilon(\mathbf{k})}{\partial \mathbf{k}} \right) = \frac{qE}{\hbar^2} \left( \frac{\partial^2 \varepsilon(\mathbf{k})}{\partial \mathbf{k}^2} \right), \quad (39)$$

and

$$\frac{\partial v(\mathbf{k})}{\partial t} \frac{1}{qE} = \frac{1}{\hbar^2} \left( \frac{\partial^2 \varepsilon(\mathbf{k})}{\partial \mathbf{k}^2} \right) = (m^*)^{-1}. \quad (40)$$

Accordingly, the effective masses will increase as function of energy into the bands following approximately:

$$m^*(E) = m^*(E=0) \left( 1 + 2 \frac{E}{E_g} \right). \quad (41)$$

The density of states effective mass ( $m_D^*$ ) is the geometric average of the transverse and longitudinal masses multiplied by the number of degenerate bands raised to power 2/3.

$$m_D^* = \left( m_L^* m_T^{*2} \right)^{1/3} N^{2/3}. \quad (42)$$

Referring back to the Fermi-Dirac distribution function, Eq. 10, we see that  $f \leq 1$ . This is plotted in Figure 4a for various temperatures. We see that at  $T=0K$  this function has a sharp cutoff where  $\epsilon = \epsilon_F$ , or the Fermi energy. At higher temperatures this cutoff is smeared out. In this figure  $\epsilon_F = 200$  meV, and we define 0 meV to be the band edge. Figure 4b contains the product of the parabolic density of states times the Fermi-Dirac distribution function. The FD function envelopes the  $g(\epsilon)$ , and gives the occupancy of the band. Clearly, at higher temperatures, electron transport occurs over a wide interval of electron energies; the shaded regions in Figure 4 are  $\pm 2 k_B T$  around  $\epsilon_F$ . Normalizing by  $k_B T$  leads to the general definition that degenerate conduction occurs when  $\epsilon_F > 3 k_B T$ . Figure 4c is the density of states calculated from Eq. 36 for a parabolic band as well as taking the Kane model for nonparabolicity. In this case, results for two different band gaps (the adjustable parameter for nonparabolic bands is the energy gap, see Eq. 41) are shown. The nonparabolicity is discussed later in this text, however for didactic purposes it is included here. Energy bands in solids do not follow parabolic dispersion relations such as free electrons do except at very low energy levels (near the band edge). It is clear that the effects of nonparabolicity are small at low  $\epsilon$  near the band edge, but greatly affect the results as  $\mu$  moves into the band. Figure 4d shows the band occupancy for various degrees of nonparabolicity of the band at 300K, and shows that indeed nonparabolic bands hold more carriers for a given Fermi energy.

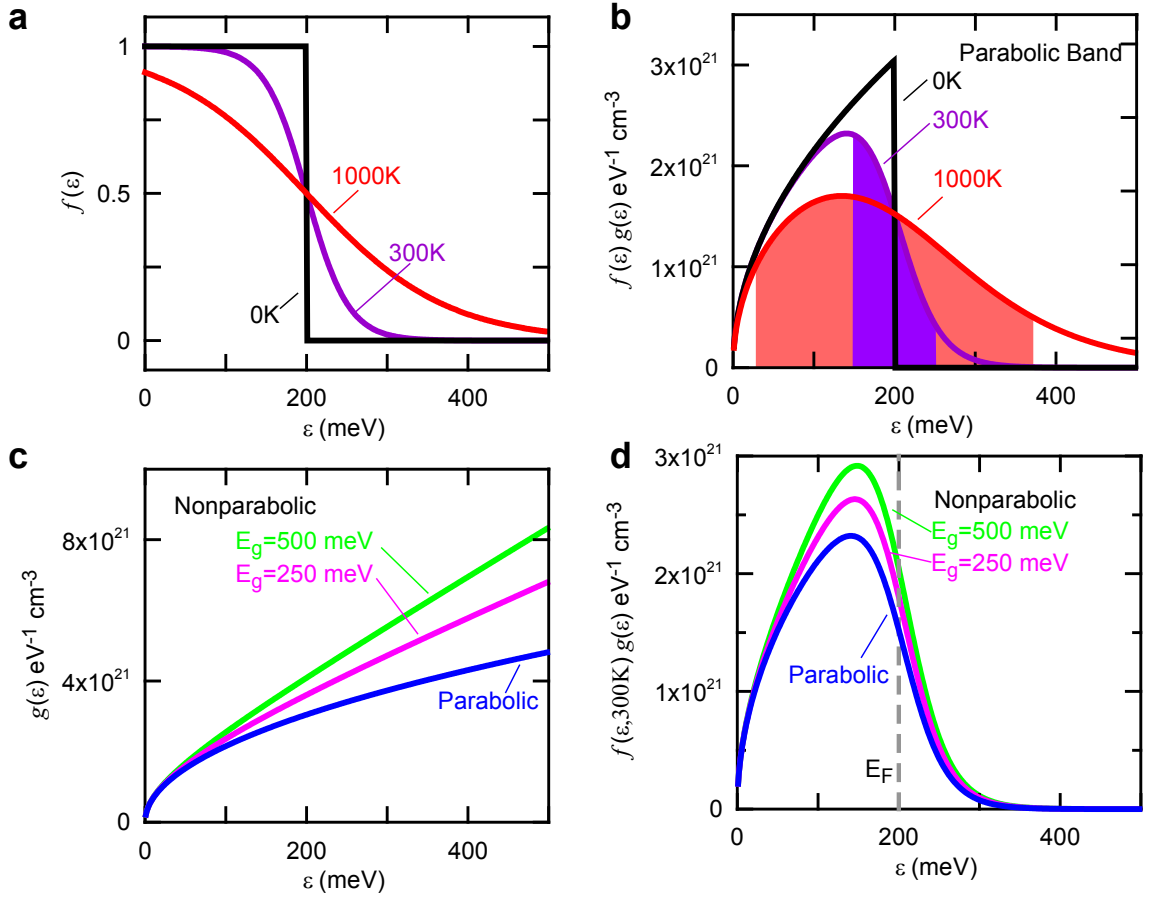


Figure 4: Fermi-Dirac statistics at various temperatures, density of states  $g(\epsilon)$  both parabolic and non-parabolic bands, the occupation of the bands at various temperatures for parabolic bands, and the comparison between band nonparabolicity.

### Resonant Levels

Before discussing the implication of resonant levels to thermoelectric technology, it is useful to transform the earlier developed equations for  $\sigma$  and  $\alpha$  to those proposed by Mott.<sup>25</sup>

$$\sigma = \int \sigma(\varepsilon) \left( -\frac{\partial f}{\partial \varepsilon} \right) d\varepsilon \quad (43)$$

$$\alpha = \frac{k_B}{q} \frac{1}{\sigma} \int \sigma(\varepsilon) \left( \frac{\varepsilon - \varepsilon_F}{k_B T} \right) \left( -\frac{\partial f}{\partial \varepsilon} \right) d\varepsilon \quad (44)$$

Here  $\sigma(\varepsilon)$  is a differential quantity and is equal to the amount of electrical conductivity of electrons with energies between  $\varepsilon$  and  $\varepsilon + d\varepsilon$ . A Bethe-Sommerfeld expansion of Eq. 44 leads to:<sup>26</sup>

$$\alpha = \frac{\pi^2}{3} \frac{k_B}{q} (k_B T) \left[ \frac{1}{n(\varepsilon)} \frac{dn(\varepsilon)}{d\varepsilon} + \frac{1}{\mu(\varepsilon)} \frac{d\mu(\varepsilon)}{d\varepsilon} \right] = \frac{\pi^2}{3} \frac{k_B}{q} (k_B T) \left[ \frac{g(\varepsilon)}{n(\varepsilon)} + \frac{1}{\mu(\varepsilon)} \frac{d\mu(\varepsilon)}{d\varepsilon} \right] \quad (45)$$

It becomes clear that the two mechanisms for increasing  $\alpha$  are either to increase  $g(\varepsilon)/n(\varepsilon)$  (resonant level) or to increase  $1/\mu(\varepsilon)(d\mu(\varepsilon)/d\varepsilon)$  (resonant scattering). Resonant impurities are capable of enhancing both, albeit at different temperatures and via different mechanisms. A resonant impurity level will introduce extra density of states in a finite energy span. This is schematically shown in Figure 5. This increased  $g(\varepsilon)$  will, if  $\varepsilon_F$  is located in the appropriate position, and provided the impurity band is capable of coupling with the host material increase the Seebeck coefficient. The second mechanism works through an increased energy dependence of  $\mu(\varepsilon)$  that has been detailed by Ravich.<sup>27</sup> Using Matthiessen's rule, it can be shown that resonant scattering is confined to low temperature application, due to the increased phonon-electron scattering at higher temperatures. The  $g(\varepsilon)$  term, however, is only temperature dependent to the order at which the energy band structure of the solid varies with temperature, which mainly arises from thermal expansion and increased phonon-electron interactions.

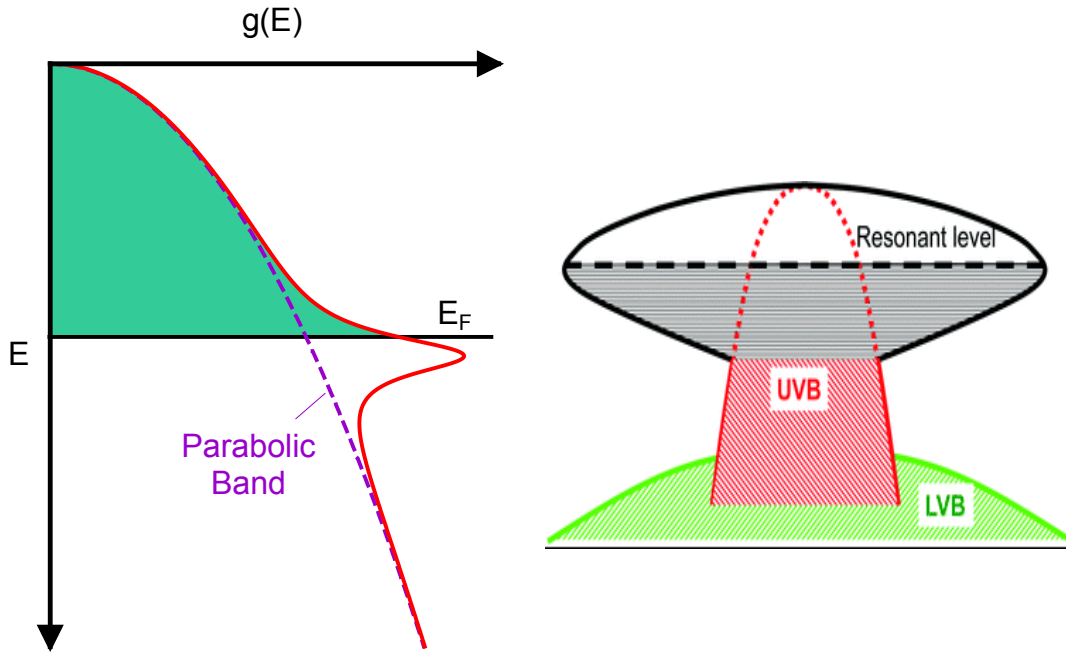


Figure 5: Left: density of states of parabolic band and a band with a resonant level. Right: energy dispersion relation for the valence band of PbTe:Tl alloys. The Tl level creates a distortion at the top of the UVB in this case.

It was shown several years ago<sup>37</sup> that the substitution of the thallium impurity for Pb in PbTe distorts the density of states (DOS) of the valence band because the Tl impurity is a resonant level in PbTe. This distortion has an energy dependence predicted earlier by Mahan and Sofo<sup>28</sup> to enhance the  $zT$  if located at the Fermi level ( $\epsilon_F$ ), because it leads to a significant enhancement in the thermoelectric power factor over that of the parent PbTe material. For an impurity energy level to enhance  $\alpha(n)$ , it is necessary but not sufficient that it contributes an enhanced DOS; for example Sb substitution for Te in PbTe:Sb was calculated to increase the DOS in the valence band, yet experimentally did not enhance  $\alpha(n)$ .<sup>29</sup> Crucial to the thermopower enhancing effect of the resonant level is the need for

it to form energy states that couple to the extended states of the solid: this is the case of Tl in PbTe and of Sn in Bi<sub>2</sub>Te<sub>3</sub><sup>30</sup>.

There are several methods to experimentally substantiate the existence of a resonant level. First, one can show a deviation in the Pisarenko relation arising from the presence of a certain impurity when compared to similarly doped samples. Further, comparisons of carrier density from Hall effect measurements to Shubnikov –de Haas measurements of the Fermi surface can indicate an additional reservoir of carriers.<sup>30</sup> This can further identify the position of the impurity level. It is necessary to determine the scattering parameter, as  $\alpha$  is a strong function of  $\lambda$ , to ensure that the deviation from Pisarenko is not a scattering effect. A strongly reduced electrical mobility is also indicative of an increased  $m^*_D$ .

## Magnetic Ordering

Numerous types of magnetic ordering have been observed in solids, due to conducting electrons, bound electrons, and unbalanced ionic charge. The magnetization, written thermodynamically, is proportional to the derivative of the magnetic Helmholtz free energy

$$M = \frac{1}{V} \frac{\partial F}{\partial H}, \quad (46)$$

where F (the Helmholtz free energy) is defined as the sum of the energies of the available states multiplied by their occupation factor:  $e^{-F/k_B T} = \sum_n e^{-\epsilon_n(H)/k_B T}$

Magnetic susceptibility follows:

$$\chi = \frac{\partial M}{\partial H}. \quad (47)$$

The interaction of the magnetic field with each electron spin is added to the Hamiltonian

$$\Delta\mathcal{H} = g_0\mu_B H\mathbf{S} \quad (48)$$

where  $\mathbf{S}=\sum\mathbf{s}$ ,  $s_x=+1/2$  or  $-1/2$ , and  $\mu_B$  is the Bohr magneton, which itself is a product of other constants:

$$\mu_B = \frac{q\hbar}{2mc}, \quad (49)$$

And  $g_0$  is the electronic g-factor ( $=2.0023$ ), and is taken to be 2 for most cases of interest.

To Eq. 37, we must add the orbital angular momentum  $\mathbf{L}$ :

$$\Delta\mathcal{H} = \mu_B(\mathbf{L} + g_0\mathbf{S}) \cdot \mathbf{H}. \quad (50)$$

When a solid is comprised of all atoms with electron shells filled, such as the Noble gas atoms, the spin and orbital momentums are zero, and thus the solid has a negative susceptibility, also known as Larmor diamagnetic susceptibility.

Paramagnetism and ferromagnetism (and its derivatives) follow from unfilled electronic levels. Hund has developed simple rules to determine the most energetically favorable population of electrons in solids based off atoms with unfilled electron shells. One can generally describe the Hamiltonian of an atom/ion with just the quantum numbers  $J, S$ , and  $L$ , where  $J$  is the total spin angular momentum ( $\mathbf{J}=\mathbf{L}+\mathbf{S}$ ). Hund's first rule states that the electrons will populate the energy shells with the same sign of spin, until that level is

full, and then will begin to fill the levels with opposing spins. Therefore, the spin angular momentum will be largest for a half filled shell, or where  $n=2l+1$ , where  $S= \frac{1}{2}n$ . Above this,  $S$  is reduced by  $\frac{1}{2}$  for every added electron. Hund's second rule determines the total orbital angular momentum  $L$ . It is equal to the sum of orbital angular momentums  $L=\sum l_z$ , and is zero for a half filled or full shell. Hund's third rule determines the value of  $J$ . If  $n<2l+1$ , then  $J=|L-S|$ , whereas if  $n>2l+1$ , then  $J=L+S$ . This occurs because less than half full shells favor antiparallel orbital and spin angular momentum, whereas greater than half full shells favor parallel orbital and spin angular momentum.

For a shell 1 electron short of being full,  $J=0$ , as with a full shell. However, this atom/ion is paramagnetic, and this special case is Van Vleck paramagnetism and the total magnetism is determined by the differences between Van Vleck and Larmor diamagnetism. If  $J\neq 0$ , then the paramagnetism is much stronger than the diamagnetism, and the shift in the Hamiltonian is

$$\Delta\mathcal{H} = \mu_B \mathbf{J} g(JLS) \cdot \mathbf{H}, \quad (51)$$

where  $g(JLS)$  is the Lande g-factor is a function of  $S, J$ , and  $L$ :

$$g(JLS) = \frac{3}{2} + \frac{1}{2} \left[ \frac{S(S+1) - L(L+1)}{J(J+1)} \right]. \quad (52)$$

Curie showed that the magnetization of a set of identical ions with the same  $J$  follows a Brillouin function. This is easiest to experimentally observe at low temperatures.

$$M = -n\mu_B g(JLS) J \frac{2J+1}{2J} \coth\left(\frac{2J+1}{2J} x\right) - \frac{1}{2J} \coth\left(\frac{1}{2J} x\right), \quad (53)$$

where  $n$  is the volumetric density of the ion. Thus, it is possible to measure concentrations of paramagnetic impurities in a diamagnetic matrix. Furthermore, the susceptibility varies with temperature, known as Curie's law:

$$\chi = -n \frac{(\mu_B g(JLS))^2 J(J+1)}{3 k_B T} \quad (54)$$

Conducting electrons will also interact magnetically with an external or internal magnetic field, and this is known as Pauli paramagnetism. The magnetic field will adjust the energy of the conducting electrons by  $\pm\mu_B H$ , depending if the electron spin is parallel or antiparallel to  $H$ . The magnetization of these electrons at low temperatures is directly related to the density of states at the Fermi energy:

$$M = \mu_B^2 g(\epsilon_F) H \quad (55)$$

The orbital motion of conducting electrons also exhibits coupling with the external magnetic field, and is diamagnetic. This is known as Landau diamagnetism, and results in a susceptibility of similar order as Pauli paramagnetism.

In the absence of any magnetic interactions, the net magnetic moment of a solid, in zero external field, will average out to zero. If, below some critical temperature  $T_c$ , there exists a non-vanishing individual vector moments, then the solid is considered to be magnetically ordered. If these individual vector moments on the ions/atoms sum to create a bulk magnetization, then the solid is considered a ferromagnet. Another case is where the individual moments sum to a zero total moment, and this is called an antiferromagnet. This occurs commonly when local moments lie on two interpenetrating sublattices in a material, such that within each sublattice each moment has the same

moment, but the two sublattices are in opposing directions. Ferrimagnets are similar to antiferromagnets; the exchange coupling between the two sublattices favors antiparallel alignment, but the moments are of different magnitude, thus summing to create to a bulk magnetization.

The temperature below where the magnetic ordering is observed is called the Neel temperature ( $T_N$ ) in antiferromagnets and the Curie temperature, ( $T_C$ ) in ferromagnets.

The magnetization obeys a power law relation against temperature:

$$M(T) = (T_c - T)^{-\delta} \tag{56}$$

Where  $\delta$  is a constant.

It can be shown through the appropriate application of quantum mechanics<sup>31</sup> that the ground state of a Heisenberg ferromagnet is one where the spins are all aligned, such as at zero temperature. This is shown in the top frame of Figure 6. However, the next higher energy level is not one spin oriented against the rest, as might be expected. The lowest state is actually a superposition of spin states such that the saturation value of the net magnetization is lowered by one unit. Furthermore, the probability of housing the misaligned spin being is the same for all locations. This is then called a magnon or spin-wave (Figure 6 lower panel), are bosons, and thus follow Bose statistics. The spin waves usually have a quadratic dispersion relation.

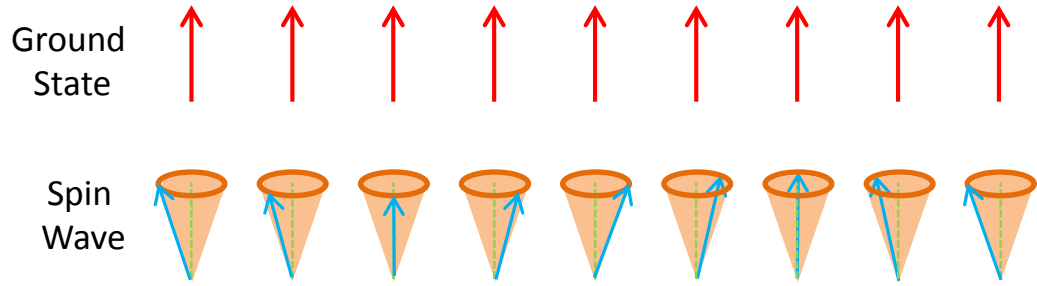


Figure 6: Ground state versus spin wave for Heisenberg ferromagnet.

## Thermal Conductivity

Total thermal conductivity ( $\kappa$ ) of the solids consists of several contributions:

$$\kappa = \kappa_L + \kappa_e + \kappa_a + \kappa_r, \quad (57)$$

where  $\kappa_L$  is the lattice contribution stemming from phonons,  $\kappa_e$  is the electronic portion as from the Weidman-Franz relation.  $\kappa_a$  is the ambipolar portion resulting from inter-band transitions, and  $\kappa_r$  is radiative conductivity from photons, and is negligible in the materials studied here.

The lattice portion from phonon heat transport can be characterized by an integral over all phonon modes, their respective velocities and relaxation lengths:

$$\kappa_L = \int C_v(q) v(q) \ell(q) dq^3, \quad (58)$$

which is sometimes simplified:

$$\kappa_L = \frac{1}{3} C_v v \ell, \quad (59)$$

where  $v$  is the sound velocity, and  $\ell$  is the phonon mean free path. The electronic portion arises as electrons (or holes) transport carry heat.  $\kappa_e$  can be calculated using the Wiedemann-Franz relation (Eq. 21), which can be written for one-directional conduction as:

$$\kappa_e = L \sigma T, \quad (60)$$

where  $L$  is the Lorenz number and is usually quoted as a ratio to the free electron Lorenz number  $L_0$ . The Wiedemann-Franz law can be derived via the Boltzmann equation as was done in Chapter 2, resulting in Eq. 21.

The ambipolar term arises from interband transitions. This can occur between two bands that have carriers of the same sign, i.e. a UVB and LVB, or between the VB and the CB. In both cases, sufficient thermal energy must exist, or the bands must be degenerate in energy, to excite electrons between the bands. This adds to  $\kappa$  as the electron-hole pairs carry a Peltier heat but no net charge current, so it doesn't improve  $\sigma$ , thus  $zT$  is diminished. The ambipolar heat is given as:

$$\kappa_a = \frac{\sigma_1 \sigma_2}{\sigma_1 + \sigma_2} (\alpha_1 - \alpha_2)^2 T, \quad (61)$$

where  $\sigma_j$ ,  $\alpha_j$  are the conductivity and thermopower of the  $j^{\text{th}}$  band. It is now apparent that two valence bands located in different regions of the Brillouin zone or that have different  $E(\mathbf{k})$  relations will have different thermopower, and thus a positive  $\kappa_a$ .  $\kappa_a$  is a major factor in picking TE materials for specific temperature ranges: SiGe's band gap allows for 1000K operation; whereas the  $zT$  of  $\text{Bi}_{0.5}\text{Sb}_{1.5}\text{Te}_3$  drops precipitously above  $\sim 400\text{K}$  due to intrinsic conduction, which also decreases thermopower.

## Lattice Thermal Conductivity

In order to analyze  $\kappa_L$  further, we must first begin with a discussion of lattice vibrations (waves), or phonons, including their behavior as modified by temperature, crystal structure, and scattering processes.

A phonon is a quantized lattice vibration that can carry heat and is statistically treated as a boson. In a macroscopic crystal comprised of one type of atom, the shortest phonon has a wavelength equal to the interatomic spacing  $a$  ( $q=\pi/a$ ) and does not propagate:  $d\omega/dq = 0$ . The longest has a wavelength equal to the length of the crystal  $N^{1/3}a$  where  $N$  is the number of atoms. In this case  $q \rightarrow 0$ , and the speed of this propagation  $d\omega/dq = v_g$  is the speed of sound. We use  $q$  for phonons and  $k$  for electrons for clarity, where both stand for wave vector and are proportional to  $\lambda^{-1}$ . Crystal momentum can be defined as:

$$\mathbf{p} = \hbar \mathbf{q} \tag{62}$$

Next, we will summarize the two types of phonon-phonon interactions: Normal and Umklapp processes. Normal processes transmit heat: they are additive and do not add to the thermal resistance of a crystal. Umklapp processes are resistive and transfer momentum to the crystal. These are shown in Figure 7 where the boxes represent a unit cell within the reciprocal lattice. In Normal processes,  $q_1+q_2$  remains inside the cell, whereas in Umklapp  $q_1+q_2$  projects outside the cell and is thus folded back by  $2\pi\mathbf{b}$  into the unit cell, where  $\mathbf{b}$  is the reciprocal lattice vector.

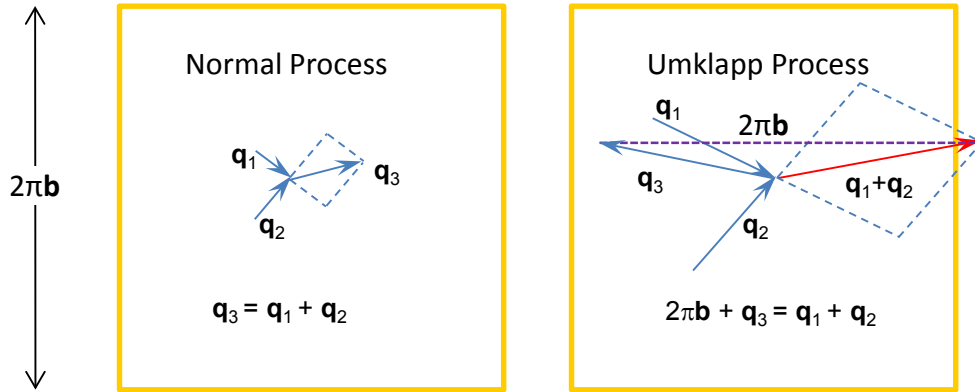


Figure 7: Schematic of the Normal and Umklapp processes. Normal are additive – leading to an infinite  $\kappa$ . Umklapp are resistive, and result in a finite  $\kappa$ . High temperature  $\kappa$  decreases as additional higher energy phonon modes are populated, thus allowing for additional Umklapp scattering processes.

Phonons begin to populate the available energy levels as  $T$  is increased from 0K. At low  $T$ , nearly all phonons have long  $\lambda$ , or small  $\mathbf{q}$ , thus most phonon-phonon interactions are Normal. This has been shown by Debye to increase as  $T^3$ , and can be seen in Figure 9 on a GaAs sample. These phonons first populate what is called the acoustic modes. They are labeled as such as they contain the long wavelength phonons that carry sound. One can treat phonons as a classic system of coupled masses and springs, and solving for the  $\omega(\mathbf{q})$  dispersion relation (the allowed energies) leads to Figure 8. The second mode is called the Optical mode because it operates at frequencies seen by optical techniques. This optical mode is dominantly a scattering mode, and the phonons from here typically undergo Umklapp processes due to their higher energies, where they can interact with an acoustic phonon, and reduce thermal conductivity.

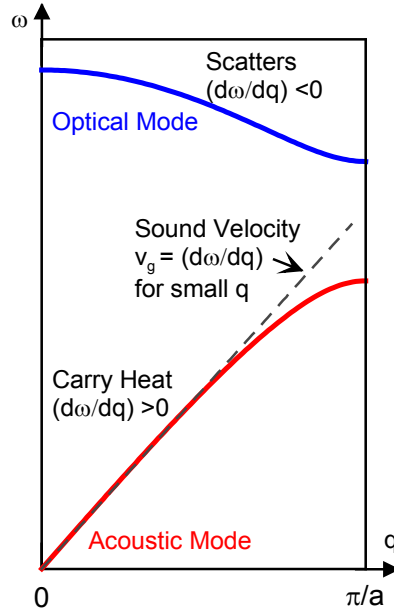


Figure 8: Schematic of the dispersion curves for a crystal showing both acoustic and optical phonon modes. In this figure we assume the longitudinal and transverse modes have the same dispersion and the crystal has two types of ions that have a mass ratio of 2. Next, we analyze the temperature dependence of specific heat  $C_p$ , which is a measurement of the number of phonons, and its influence on lattice thermal conductivity. Figure 9 contains experimental data taken on a GaAs sample. At temperatures below the peak of  $\kappa(T)$ , it increases because the number of phonons increases. According to the Debye theory, the number of phonons (which is proportional to  $C_p$ ) increases as  $T^3$ ; here  $C_p$  increases slightly faster at intermediate temperatures. This can occur because the different acoustic modes – the two transverse acoustic (TA) and single longitudinal acoustic (LA) will not have the same Debye temperatures nor dispersion relation, and thus will populate their energy levels at some pace around  $T^3$ .  $\kappa$  increases slightly slower than a  $T^3$ , possibly from increased scattering as  $T$  is increased. The peak in  $\kappa$  occurs because of two competing phenomena – increase in the number of phonons at low  $T$ , and

an increase in resistive or Umklapp processes at high temperatures. As  $T$  is decreased from 300K, phonons do not have enough momentum to scatter into the next Brillouin zone, and thus collisions become elastic and additive. However, crystal defects will still scatter, and thus the mean free path will saturate at some finite value, even if it is the size of the sample.

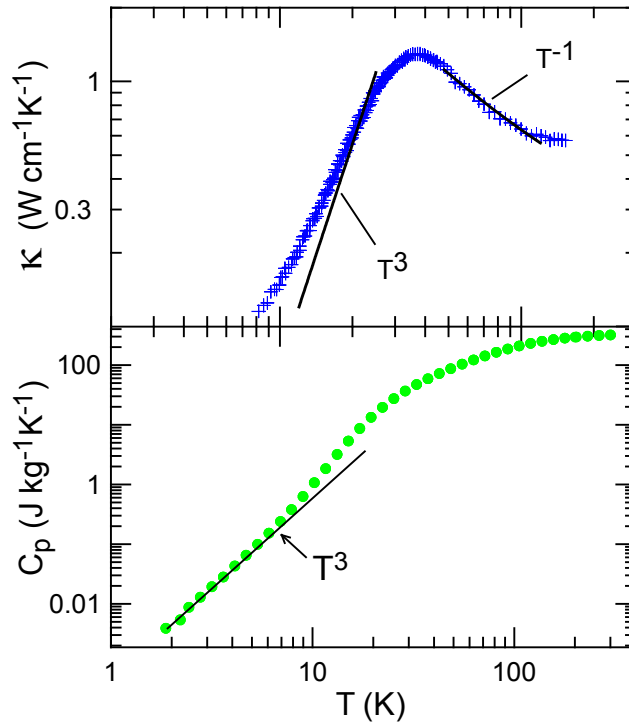


Figure 9: Thermal conductivity and specific heat for a GaAs bulk sample.

### Phonon Drag

Phonons are able to impart momentum to electrons and magnons. This is a non-equilibrium process. This is easiest seen in an excess in thermopower at lower temperatures. It occurs when the selection rules allow the interaction of phonons and electrons: the momentum of an interacting phonon must be such that it is able to scatter an electron from the Fermi surface to the Fermi surface.

At higher temperature, thermopower can be described by the Boltzmann equation and has linear temperature dependence in accordance with the Mott relation. The  $\nabla T$  only slightly disturbs the Fermi distribution function; phonons and electrons are constantly brought back to equilibrium by collisions. At sufficiently low  $T$ , when phonons do not have enough momentum to scatter with each other in Umklapp processes, they can impart a momentum to the electrons in a process that peaks at a temperature where the momentum of the phonons coincides with the size of the Fermi surface. This moves the electron distribution away from equilibrium and the effective mass of the charge carriers is increased. A resulting electric field ensues to balance out this additional momentum, and the thermopower is enhanced. At lower temperatures, the number of phonons decreases and thus phonon-electron drag drops. The peak is located  $T \sim \theta_D/5$ , where  $\theta_D$  is the Debye temperature.

While the case of phonon-electron drag has been studied extensively, phonon-magnon (PM) drag has received less attention. Similarly, the driving force for PM drag is the temperature difference between the phonons and magnons. We will address this further in Section 5.

## Galvanomagnetic and Thermomagnetic Effects

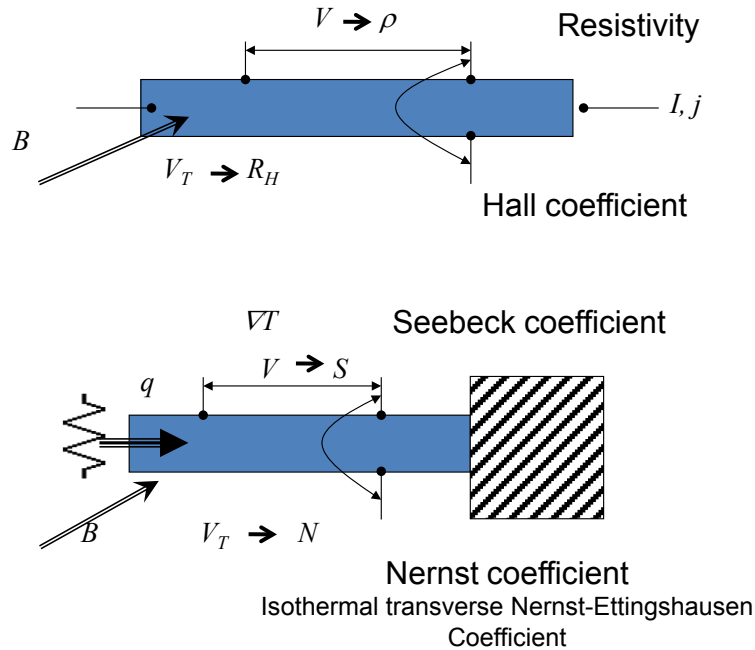


Figure 10: Schematic of measurement geometry in cryostat of the four measured properties: electrical resistivity, Hall coefficient, Seebeck and Nernst-Ettingshausen coefficients that are the standard measurements performed.

Electrons entering a material in magnetic field do so at the Hall angle, which is the ratio between the Hall  $E_y$  and resistive  $E_x$ . If, while traveling in the  $x$  direction they are subjected to a transverse magnetic field ( $z$ -direction), they are deflected by the Lorentz force in the  $y$ -direction, thus setting up an excess of electrons on one side of the sample. An  $E_y$  is thus generated to balance the Lorentz force as shown in Figure 11. This resistance  $\rho_{xy}(B_z)$  is termed the Hall resistance and the Hall coefficient is defined as:

$$R_H = \frac{E_y}{j_x B_z}. \text{ This is of great interest as the slope of } R_H(B) \text{ tells the sign of the carrier.}$$

Further, an expression for the carrier density can be derived,  $n = A/R_H q$ , where A is the Hall prefactor. This prefactor can, to a first approximation, be set to unity in some materials. A detailed discussion of this will follow.

The Nernst-Ettingshausen (Nernst) effect is used to measure the dominant scattering processes in a material. Under the influence of  $\nabla_x T$ , electrons (or holes) diffuse to the cold side of the sample. In a  $B_z$ , the Lorentz force deflects the carriers, setting up a transverse electric field. This is known as the Nernst effect and is depicted in Figure 11. As the slow moving (colder) charge carriers spend more time experiencing the Lorentz force, they are deflected more, and this creates an  $\nabla_y T$ , the Righi-Leduc effect. From the Seebeck effect, this also generates an additional  $E_y$  that is added (or subtracted) to the Nernst  $E_y$ . Therefore, the Nernst isothermal-adiabatic correction factor is used.<sup>32</sup> Conversely, one can measure  $\Delta T_y$  and using the known value of S, subtract the Righi-Leduc  $\Delta V_y$ . The sign of the Nernst is not sensitive to the sign of charge carrier. The

Nernst coefficient is defined as  $N = \frac{E_y}{\nabla_x T B_z}$  The magnitude of the Nernst coefficient can

used to calculate the dominant scattering mechanisms if we assume a power law energy dependence to the scattering mechanisms and thus relaxation time:  $\tau = \tau_0 E^{\lambda-1/2}$ , where  $\lambda=2$  for ionized impurity scattering, 0 for acoustic phonon scattering, and 1 for optical phonon scattering. In a conductor dominated by ionized impurity scattering, higher energy electrons will have a longer relaxation time as they are less influenced by the ion. Conversely, in an acoustic phonon dominated conductor, higher energy electrons will experience a greater rate of scattering due to increased phonon-electron collisions. This

can be understood as the larger momentum of higher energy electrons allows for an increased probability of scattering with phonons. Reflecting on Eq. 27, we see that a larger scattering parameter will lead to an increased thermopower, as the higher energy electrons will be preferentially less scattered.

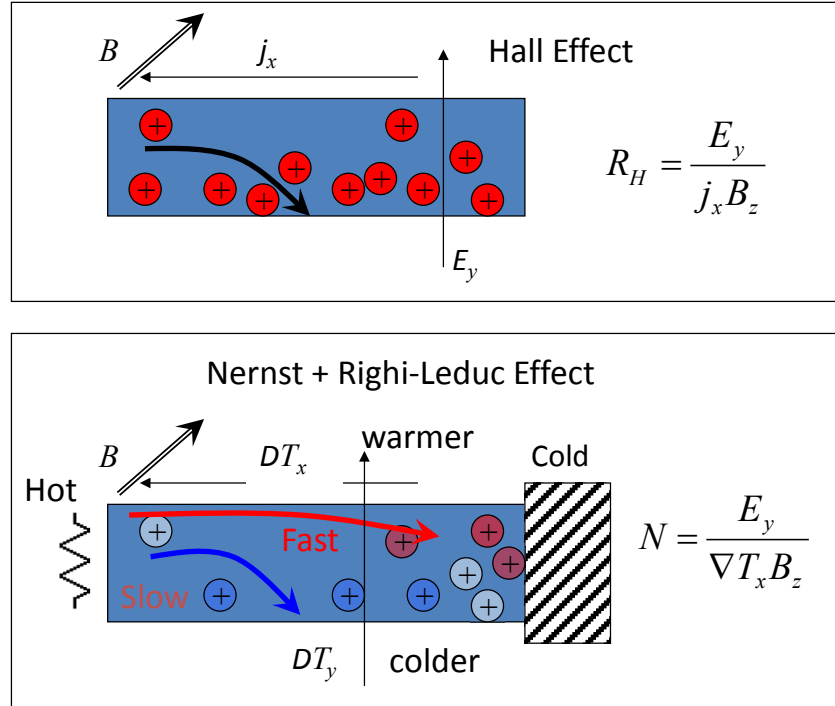


Figure 11: Schematics of the Hall, Nernst, and Righi-Leduc effects

## Hall Effect and Hall Prefactor

The Hall coefficient is related to the electron/hole density:

$$n = \frac{r_H(\lambda, K)}{R_H q}, \quad (63)$$

where  $r_H(\lambda, K)$  is the Hall prefactor. This is a function of the general band structure  $r_H(K)$  and the details of the dominant scattering mechanisms  $r_H(\lambda)$ . For this equation to hold,

there must only be one type of carrier present. The first element in the Hall prefactor is the mass anisotropy factor:

$$r_H(K) = \frac{3K(K+2)}{(2K+1)^2}, \quad (64)$$

where  $K = \frac{m_{\parallel}^*}{m_{\perp}^*}$ .  $r_H(K)$  is strictly less than 1. In a spherical Fermi surface,  $K=1$  and thus  $r_H(K)=1$ . However, for ellipsoidal pockets, such as the (upper valence band) UVB and lowest conduction band (LCB) in PbTe,  $K=10 \pm 1.5$  for the LCB and  $K=14 \pm 2$  for the UVB<sup>24</sup>. This leads to  $r_H(K)=0.82$  for n-type and  $r_H(K)=0.80$  for p-type, which are essentially the same, given experimental uncertainties.  $K$  for the lower valence band (LVB) in PbTe is experimentally unknown.

The second element in the hall prefactor is a statistical averaging of the relaxation time:

$$r_H(\lambda) = \frac{\langle \tau^2 \rangle}{\langle \tau \rangle^2}, \quad (65)$$

where

$$\langle \tau \rangle = \frac{\int_0^{\infty} \tau (-df/d\varepsilon) k^3 d\varepsilon}{\int_0^{\infty} (-df/d\varepsilon) k^3 d\varepsilon}. \quad (66)$$

It then follows assuming anisotropic scattering:

$$r_H(\lambda) = \frac{3}{2} \frac{2\lambda + 3/2}{(\lambda + 3/2)^2} \frac{F_{2\lambda+1/2}(\varepsilon_F) F_{1/2}(\varepsilon_F)}{[F_{\lambda+1/2}(\varepsilon_F)]^2}. \quad (67)$$

If, for instance, acoustic scattering dominates as is typical in PbTe,  $r_H(\lambda) = 3\pi/8 \approx 1.18$ . In this case, for PbTe,  $r_H(K, \lambda) \approx 1$ . For ionized impurity scattering,  $r_H(\lambda) = 1.9$ .  $F_i$  is the Fermi integral.<sup>24</sup>

If there is a second carrier present, then the simple Hall formula (Eq. 48) does not hold. The Hall prefactor is only reliant on the general band structure and dominant scattering mechanisms, so this is not necessarily modified by the presence of a second carrier, such as if one were to analyze PbTe in the intrinsic regime with an extrinsic dopant. The modification of the Hall formula, assuming acoustic scattering in PbTe, thus  $r_H(K, \lambda) \approx 1$ :

$$R_H = \frac{\mu_p^2 p - \mu_n^2 n}{(\mu_p p + \mu_n n)^2} \frac{1}{q} \quad (68)$$

and total electrical conductivity:

$$\sigma = q\mu_p p + q\mu_n n = \sigma_p + \sigma_n, \quad (69)$$

where the  $p$  is the concentration of holes,  $n$  the concentration of electrons, and their respective mobility:  $\mu_n$ , &  $\mu_h$ . As there are now more unknowns than equations, we must use the magnetic field dependence of  $\rho_{xx}(B_z)$  and  $\rho_{xy}(B_z)$ , the transverse magnetoresistance and Hall resistance. Inverting the measured data and using the longitudinal and transverse resistivities:

$$\rho_{xx} = \frac{\sigma_{xx}}{\sigma_{xx}^2 + \sigma_{xy}^2} \quad \text{and} \quad \rho_{xy} = \frac{\sigma_{xy}}{\sigma_{xx}^2 + \sigma_{xy}^2}, \quad (70)$$

where for two carrier conduction:

$$\sigma_{xx}(B_z) = \frac{n \cdot q \cdot \mu_n}{1 + \mu_n^2 B_z^2} + \frac{p \cdot q \cdot \mu_p}{1 + \mu_p^2 B_z^2} \quad \text{and} \quad \sigma_{xy}(B_z) = \frac{n \cdot q \cdot \mu_n^2 B_z}{1 + \mu_n^2 B_z^2} + \frac{p \cdot q \cdot \mu_p^2 B_z}{1 + \mu_p^2 B_z^2}. \quad (71)$$

Fitting this data allows for the calculation of the concentration of holes, electrons, and their respective mobility. Obviously, this can be extended to carrier of the same sign but from different bands, as long as two carrier mobilities are sufficiently different in magnitude.

Furthermore, this is possible in Pb salts and InSb because of their cubic symmetry<sup>33</sup> and the solely even nature of  $\rho_{xx}$  and solely odd nature of  $\rho_{xy}$ : in rhombohedral materials, such as Bi<sub>2</sub>Te<sub>3</sub>, this is not possible.

### **Shubnikov - de Haas (SdH) Oscillations**

Measurements of transport properties in magnetic field will, under specific conditions, contain oscillations that are related to the shape of the Fermi surface. At low temperatures, where the Fermi function (Eq. 10) is sharper and when  $\mu B > 1$  so that electrons in a magnetic field pass through complete cyclotron orbits (complete helicoidal paths in real space), the energy levels (density of available states) are redefined to be<sup>21</sup>:

$$\gamma(\varepsilon) = \frac{\hbar^2 k_z^2}{2m^*} + (i + \frac{1}{2})\hbar\omega_c + g s_z \mu_B B_z \quad (72)$$

Note the distinction from the 3D case where  $\gamma(\varepsilon) \sim \sqrt{\varepsilon}$ . Here  $\omega_c = qB/m^*c$ ,  $\mu$  is electron mobility,  $s_z = \pm 1/2$  is the spin quantum number,  $g$  is the g-factor or dimensionless magnetic moment, and  $\mu_B$  is the Bohr magneton. The quantum number  $i = 0, 1, 2, \dots$  and  $k_z$  takes values as allowed by the crystal lattice. This motion by electrons is allowed as it is normal to the Lorentz force, i.e. the direction of electron motion is along the external

magnetic field. Thus, the level  $i = 1$  is known as the 1<sup>st</sup> Landau level, and so on and a schematic is shown in Figure 12. The available orbital energy levels tracks linearly with external magnetic field  $B$ . This quantization of available energies creates cylinders known as Landau tubes along the direction of magnetic field. Thus, as the field is increased, the available levels (tubes) will move through the Fermi surface. Thus the contribution to the  $g(\varepsilon)$  from the  $i$ th orbital will have a peak whenever  $\varepsilon$  is equal to the energy of the extremal orbit.

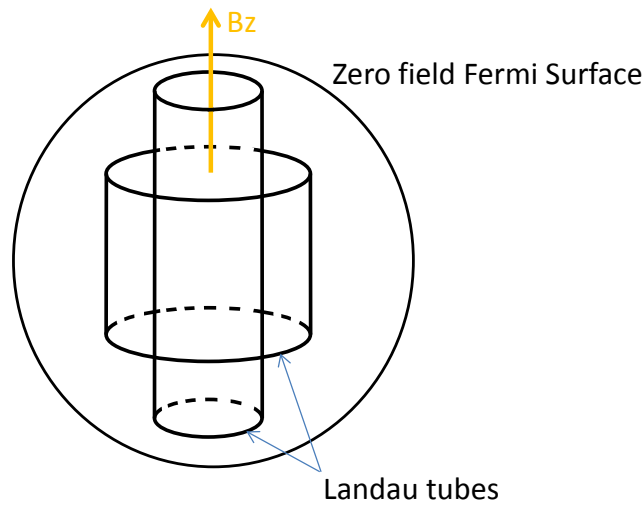


Figure 12: Variation of Fermi surface in a quantizing magnetic field.

The time for an electron to complete one orbit around a Landau tube can be calculated:

$$t = \frac{2\pi}{\omega_c} = \frac{\hbar}{qB} \oint v_c^{-1} dk \quad (73)$$

Where  $v_c$  is the velocity of the electron normal to  $B$ . This time will not change for different orientations of magnetic field for a spherical Fermi surface, but will for

ellipsoidal and other shapes, which is very useful for mapping Fermi surfaces. Solving for cyclotron frequency in Eq. 73

$$\omega_c = \frac{2\pi q B}{\hbar} \frac{1}{\oint v_c^{-1} dk} \quad (74)$$

Now electron velocity is proportional to  $\nabla \varepsilon(\mathbf{k})$  so a small change in energy  $\Delta \varepsilon$  leads to a small change in k-space  $\Delta k = \frac{\Delta \varepsilon}{\lambda v_c}$ , leading to a new orbit located at  $\varepsilon + d\varepsilon$ . Thus

$\oint v_c^{-1} dk \sim \Delta A_F$ , or the area of the Fermi surface between  $\varepsilon + d\varepsilon$ , or  $k + dk$ . Solving for cyclotron frequency:

$$\omega_c = \frac{2\pi q B}{\hbar^2} \frac{\partial \varepsilon}{\partial A_F} \quad (75)$$

Using Eq. 72 where it was supposed that energy is quantized into Landau tubes, the area of the orbit becomes quantized in units of  $\frac{2\pi q B}{\hbar}$ . For the area enclosed by orbit  $E_i$ , we

$$\text{find: } A_i = \frac{2\pi q B}{\hbar} (i + 1/2)$$

It then follows that the period of oscillation when plotted against  $1/B$  is related to the area of the Fermi surface

$$\Delta \frac{1}{B} = \frac{2\pi q}{\hbar A_F} \quad (76)$$

As a tube sweeps through the Fermi surface (by increasing  $B$ ), the number of electrons locally near  $\varepsilon_F$  is increases as the  $g(\varepsilon)$  has a peak imposed by the quantization conditions (developed earlier) when  $\varepsilon = \varepsilon_i$ . As the next tube approaches the Fermi level, additional

states become available as the magnitude of the tube's area is proportional to the magnetic field. This then leads to an oscillation in  $1/B$  of the  $g(\epsilon)$  near  $\epsilon_F$ , and thus, in measurable thermomagnetic and galvanomagnetic transport properties.

The last term in Eq. 72 is related to the electron spin as collapsed into the g-factor. This spin splitting of the Landau levels effectively doubles the number of oscillations. By rotating the direction of the crystal with respect to the magnetic field, it is possible to map out the Fermi surface in 3D by taking enough cross sections.

Next, we show an example measurement of SdH and the data treatment to determine the area of the Fermi surface. Figure 13 shows electrical resistivity in a cubic crystal at low temperatures that exhibits SdH oscillations. The raw data is in panel a; panel b has subtracted a parabolic background (as magnetoresistance in a cubic crystal is proportional to  $B^2$  and thus even symmetric in field). Next, the data in panel b is plotted vs.  $1/B$ , and then Fourier transformed. This allows the identification of peaks in frequencies in units of  $1/B$ . The results of this are shown in panel c, which clearly show a maximum at approximately  $1.15 \text{ T}^{-1}$ . With the known band structure and crystal orientation of this solid, one can then calculate  $k_F$  (the Fermi wave vector), and subsequently the number of electrons (or holes).

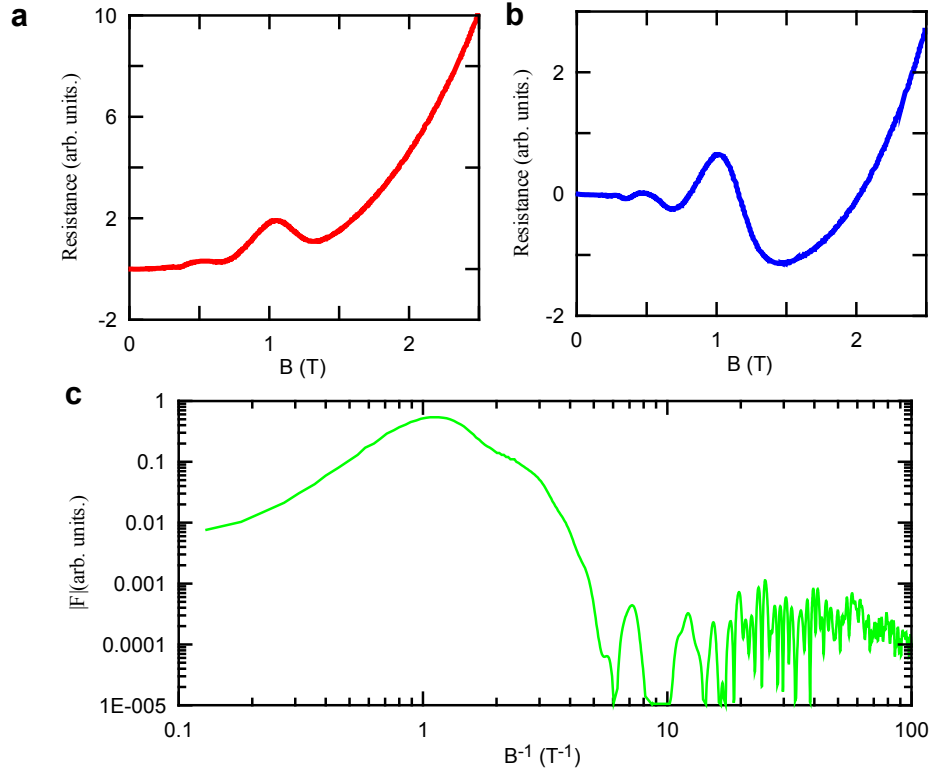


Figure 13: a) Electrical resistivity of a sample as a function of magnetic field at low T showing clear oscillations. b) trace in (a) with parabolic background subtracted. c) inverse Fourier transform of data in b) vs  $1/B$ . with a maximum  $\sim 1.15\text{T}^{-1}$ .

### Inverse Spin-Hall Effect

The spin-Hall effect was first experimentally discovered in 2003.<sup>34</sup> It consisted of a spin accumulation on the edges of a sample with spin-polarized current flowing through. Most importantly, the signs of the spin on each surface have opposite direction. This occurs in the absence of magnetic field. Essentially, a spin current flows in a transverse direction to the spin-polarized electrical current. There are two types of spin Hall effect: extrinsic and intrinsic.

The inverse spin Hall effect is used to measure the spin Seebeck effect as shown in Figure 14. Pt strips are deposited onto the ferromagnet. The Pt strips act as a spin-polarization detector based on the ISHE and the measured voltage, or integrated electric field  $E_{ISHE}$ , is a measure of the vertical flux of number, orientation, and transfer efficiency of the spin-polarized particles that reach from the ferromagnetic layer into the Pt:

$$E_{ISHE} = D_{ISHE} (\overline{J}_S \times \overline{\sigma}), \quad (77)$$

where  $\sigma$  is the spin orientation,  $J_S$  is the spin current,  $D_{ishe}$  is the ISHE coefficient of platinum.

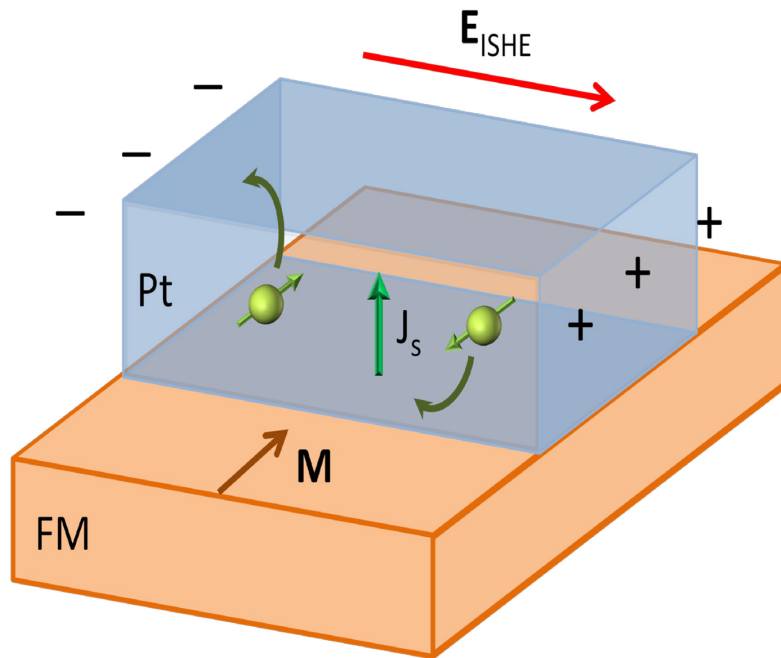


Figure 14: Schematic of the inverse spin Hall effect. The ferromagnet (FM) inject spin into the normal metal (Pt). The spin current is deflected preferentially via skew scattering or side jump, and results in a transverse flow of charge. In open circuit conditions, this creates an electric field  $E_{ISHE}$ .

## Chapter 3: Experimental Techniques

### Thermoelectric Methods

To prepare a thermoelectric material, such as  $\text{PbCh:X}$  ( $\text{Ch}=\text{Te, Se, S}$ ,  $\text{X}=\text{Na, Tl, Al}$ ) stoichiometric amounts of the starting elements ( $\text{Pb, Te, Al, S, Se, Na, Tl}$ , all  $\geq 5\text{N}$  purity) were loaded into carbon coated quartz ampoules in an argon filled glovebox. The ampoules were sealed with a propane torch at pressures less than  $10^{-6}$  torr.  $\text{PbTeS:Na}$  samples were heated to 1373K and annealed at 1100K,  $\text{PbTe:Al}$  samples were heated to 1273K and annealed at 1073K,  $\text{PbTeS:Tl}$  materials were heated to 1273K and annealed at 1100K, and  $\text{PbTeSe:Tl}$  samples were heated to 1273K and annealed at 773K. These annealing temperatures are chosen to maximize the solubility of the dopant in the  $\text{PbTe}$  matrix, to relieve mechanical stress resulting from cooling, or in the case of  $\text{PbTeS}$  material, to allow for a single phase between  $\text{PbTe-PbS}$ .

After removal from the ampoule, the ingots are cut on a diamond wire saw. Parallelepipeds measuring approximately 1-2mm x 1-2mm x 5-7mm are used for measurements of  $S$ ,  $\rho$ ,  $N$ , and  $R_H$ , which are taken simultaneously between 2-420K. Measurements of  $S$  and  $\rho$  at elevated temperatures ( $>420\text{K}$ ) are on parallelepipeds approximately  $2 \times 2 \times 15 \text{ mm}^3$ . Specific heat is measured on samples weighing approximately 50 mg  $2\text{K} < T < 800\text{K}$ . Disks between 1-2 mm thick are used for thermal diffusivity at  $T \geq 300\text{K}$ . Powder XRD is performed to ensure the correct crystal structure, lattice parameter, and single phase nature of the synthesized material.

From 80-420K,  $S$ ,  $\rho$ ,  $N$ , and  $R_H$ , are measured in custom systems utilizing a conventional flow liquid nitrogen non-optical cryostat. Magnetic fields are generated using an iron pole electromagnet between  $\pm 1.8$  T or  $\pm 1.5$ T, depending on the cryostat used. Thermopower (3% error) and Nernst effect (5% error) are measured in a static heater and sink method with differential type T-thermocouples (GaAlAs diodes on the cryostat provide the absolute T) with 0.025 mm diameter copper-constantan wires providing  $\Delta T_x$ , and the same copper wires are used for  $\Delta V_x$ , or the Seebeck voltage as shown in Figure 15. Transverse leads ( $V_T$ ,  $V_B$ ) are attached for the  $\Delta V_y$  Nernst measurement. Electrical resistivity (10% error, mainly from measurements of sample geometry) is measured in a 4-point configuration using an AC bridge, with current leads attached to the ends of the samples, and utilizing the thermocouple copper wires for voltage leads. Similarly, the Hall resistance (5% error) is measured using the same leads for Nernst voltage. The Hall and Nernst coefficients are defined as the low field slope of the Hall resistance and Nernst voltages, once properly normalized. Furthermore, the standard correction factor to convert from adiabatic to isothermal Nernst voltage is used to remove the Righi-Leduc effect.<sup>32</sup>

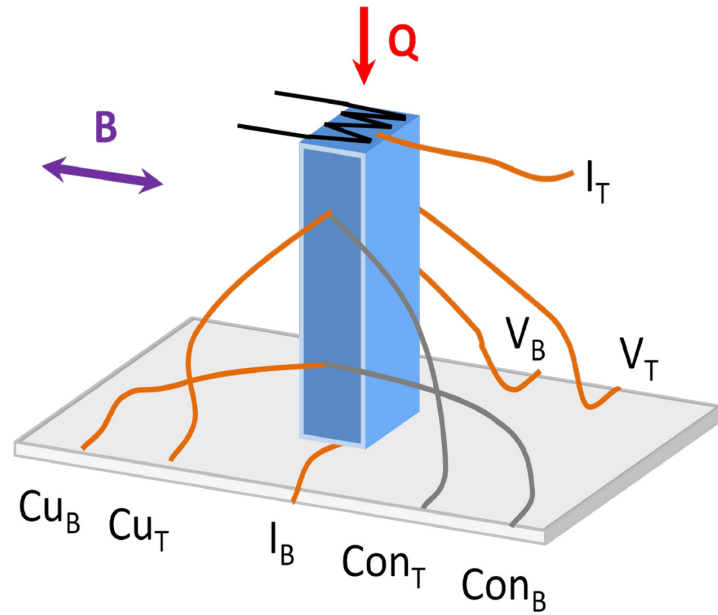


Figure 15: Measurement schematic in home built cryostats.

From 2-300K a Quantum Design Physical Properties Measurement System is used to measure  $R_H$ ,  $S$ ,  $\rho$ ,  $\kappa$  in the Thermal Transport Option (TTO) and AC Transport Option (ACT). This machine is cooled by liquid helium, and has a bipolar superconducting magnet capable of 7T. The TTO (Figure 16) uses user-calibrated Cernox thermometers attached to gold plated copper leads to determine  $\Delta T_x$ . These same leads provide  $\Delta V_y$ , and are the voltage leads for the 4-wire AC resistance measurement. The TTO uses a proprietary Quantum Design “two-tau” measurement routine to determine  $\kappa$  and  $S$  and can measure while sweeping cryostat temperature using the standard heater and sink method. Hall coefficient is measured in the ACT in a similar manner to the home built cryostats.

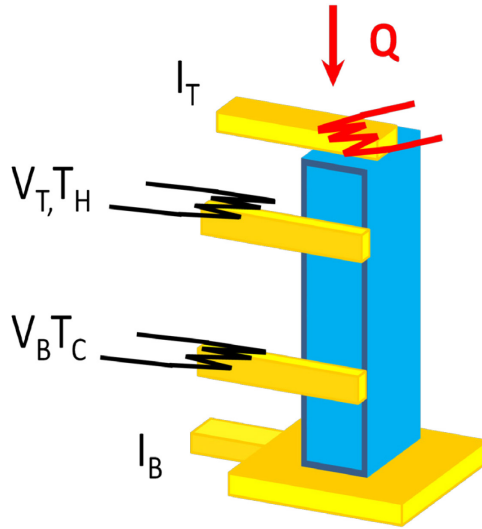


Figure 16: Measurement setup in the Thermal Transport Option.

For the PbTeS:Na samples, high temperature measurements were measured at Oak Ridge National Laboratory in a ULVAC ZEM-2 under -0.09 MPa static helium using R-type thermocouples and Ni electrodes. Thermopower was measured using a static DC method, (<5% error) and  $\rho$  using the standard 4-wire method with an AC bridge (<6% error).

Thermal diffusivity is measured between 300-800K on an Anter Flashline 3000 using a xenon lamp and liquid nitrogen cooled InSb detector. Specific heat is measured from 2-300K in the PPMS on the Heat Capacity Option, and from 300-800K in a modulated Differential Scanning Calorimeter from TA Instruments. Mass density is measured using both geometrical and Archimedes' method, and literature coefficient of thermal expansion values are used to correct for the temperature dependence. These are combined for thermal conductivity yielding an error of 10%.

## Spin-Seebeck Effect Methods

The samples measured are epitaxial  $\text{Ga}_{1-s}\text{Mn}_s\text{As}$  grown on semi-insulating [001] GaAs substrates using a Veeco Gen II MBE system by Roberto C. Myers and Shawn Mack. While we repeated the measurements several times on various samples, the sample studied in greatest detail is a 30-nm GaMnAs grown at 150 °C and with  $s=0.158$ . The Mn concentration was calibrated using GaAs and MnAs RHEED oscillations. This sample was grown with substrate rotation to prevent any gradients across the sample and the As:Ga flux ratio was carefully calibrated using low temperature stoichiometric non-rotated growth calibrations,<sup>35</sup> where the As:Ga ratio and therefore the stoichiometry of the films can be fine-tuned. The samples exhibited in-plane easy axes. Additional samples were grown and tested and exhibit similar behavior as the one shown here. Sample magnetic characterization was performed in a superconducting quantum interference device (SQUID) magnetometer. The magnetic field was oriented parallel to uniaxial and cubic switching directions. Magnetization hysteresis loops and  $M(T)$  were recorded. We subtracted the diamagnetic background of the GaAs substrate using the high field slope of  $M(B)$ .

The wafers are cleaved into samples 3-5 mm wide (along  $y$ ) by 10-25 mm long (along  $x$ ) with  $x$  oriented along either  $[110]$  or  $[1\bar{1}0]$  crystal directions. A layer of Ti less than 1-nm thick was deposited onto the GaMnAs for adhesion followed by 10 nm of Pt in an electron beam evaporator through a shadow mask. These strips are deposited along the  $y$ -axis at varying  $x$  positions and are approximately 0.25 mm wide. I-V curves between Pt

strips show the contacts are ohmic. A schematic of the sample geometry is shown in Figure 17.

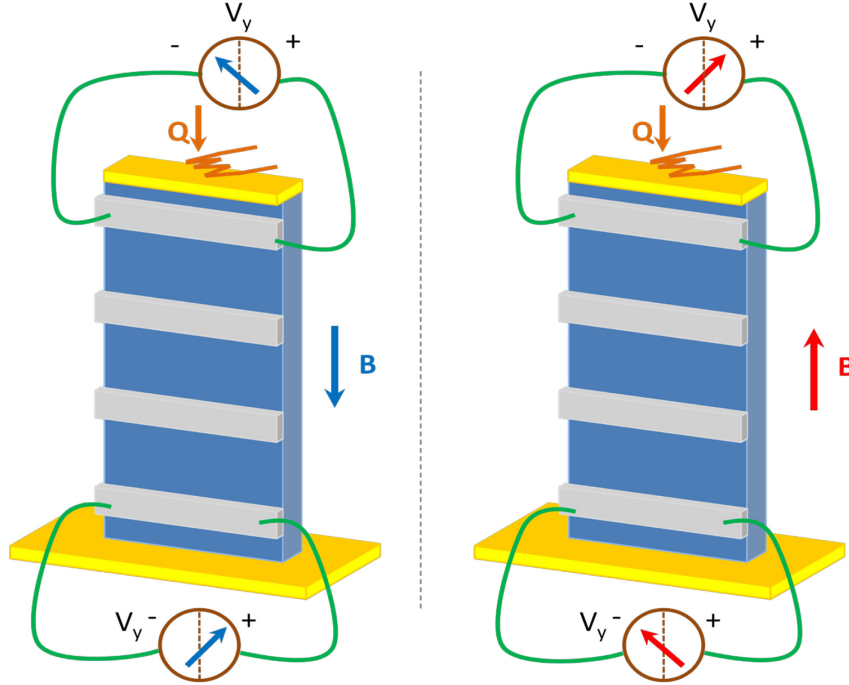


Figure 17: Measurement setup for spin-Seebeck experiments. Not to scale. Voltages shown for ferromagnets.

The samples were measured over the temperature range 2-300K under high vacuum using the Thermal Transport Option (TTO) in a Quantum Design Physical Properties Measurement System. Cernox thermometers attached to gold plated copper leads (not shown in Figure 4) are used to determine longitudinal temperature difference ( $\Delta T_x$ ). Out-of-plane temperature gradients are avoided by the use of bulk samples with minimized heat leaks through contacts (40  $\mu\text{m}$  copper wires silver epoxied to the Pt bars or soldered to the In point contacts as voltage leads), radiative or convective losses (fully gold-plated cryopumped sample chamber). Variations in contact size generate error as the length

used in the normalization process varies. We step temperature and heater power, and after sufficient stabilization time ( $\sim 1$  hr) record  $\Delta T_x$  and  $V_y$  using a Keithley 2182A nanovoltmeter while sweeping magnetic hysteresis loops. The background voltages and EMF pickup are removed and the signal is centered at zero. We are forced to sweep magnetic field, instead of stepping and averaging  $V_y$ , in order to remove the effect of thermal drift on background voltages. Field is swept at an average rate of 13 Oe/s, the minimum value obtainable in our machine. We measure with and without the thermometry attached, with no change in signal sign or magnitude. The differences in the magnetization data and spin-Seebeck data coercive fields could arise since these measurements were performed in different instruments, using different sweep methods (step for magnetization and sweep for spin-Seebeck), along with delay from the 2182A 100 millisecond integration time. Measurements on the strips nominally have an RMS noise of 10-15 nV. A report of zero  $S_{xy}$  means that  $\Delta V_y$  is less than the noise. Error in this study stems not only from the signal to noise ratio, but also from the thermometry error in  $\Delta T_x$ , which increases at low T. The extremely high thermal conductance of the GaAs substrates makes establishing a sufficient temperature gradient to allow measurement difficult, and the power one can dissipate in the heater is limited by the ability of the cryostat to maintain a stable temperature. We estimate error by dividing the RMS noise by  $\Delta T_x$ . This is added to the thermometry uncertainty for each point, and thus yields error bars for each data point. Charge Seebeck ( $\alpha_{xx}$ ) is measured using the same setup in continuous mode with a sweep rate of 1 K  $m^{-1}$ .

For InSb, the samples used were cleaved from a Te-doped bulk InSb wafer. Parallelepipeds ( $z=0.5$  mm thick,  $y=3-5$  mm wide and  $x=10-20$  mm long) were cleaved

from the same wafer along the [100] direction. For the measurements, 10 nm of Pt was deposited on top of a 1 nm thick Ti adhesion layer on the InSb;  $I/V$  characteristics at mV scale on these contacts were ohmic. All measurements are made using the same experimental apparatus as GaMnAs.  $R_H(T)$  and  $\rho(T)$  are measured using a Lakeshore 370 AC bridge in 4-point configuration. Cernox thermometry (Lakeshore CX-1050-BR) calibrated as a function of  $T$  is used instead of the standard Quantum Design Cernox thermometers in the SD packaging. For SSE measurements, we fix cryostat temperature and heater power and sweep  $B$  while recording  $V_y$  across the Pt strips using a Keithley 2182A nanovoltmeter. Relative error in  $S_{xy}(B)$  is readily apparent in the noise; the main source of absolute error is in  $\Delta T_x$ , and is individually estimated for each point.

## Chapter 4: Lead Chalcogenides

PbTe<sup>36,37</sup> and its alloys with PbS<sup>38,39</sup> are the materials with some of the highest thermoelectric figures of merit in the temperature range of 500-800 K suitable for waste heat recovery applications.<sup>40</sup> The main reason for this is the extremely low lattice thermal conductivity of even binary PbTe, mostly due to the very high anharmonicity<sup>41</sup> of the bonds, which results in very large phonon-phonon scattering at high temperature. The recently identified soft behavior of the PbTe lattice is related to this anharmonicity and is quite likely at the physical origin of this.<sup>42</sup> A phase transition of possibly a similar nature is also present<sup>43</sup> in the PbTe<sub>1-x</sub>S<sub>x</sub> alloys studied here.

In this section we begin with background of lead chalcogenides, then we continue with a discussion the valence band structure of PbTe - mainly its temperature dependence, and then finally discuss experimental results on the three material systems studied here: PbTe:Al, PbTeS:Tl, and PbTeS:Na.

### General Properties

PbTe, PbSe and PbS are cubic NaCl lattices of m3m symmetry with a face centered unit cell. It follows that the coordination number for each atom is six. The lattice constants for each are: 6.462, 6.12, 5.94 Angstroms, with PbTe the largest, PbS the smallest. The Pb ions are centered at (0,0,0) and the Te/Se/S ions at  $a/2(\hat{x} + \hat{y} + \hat{z})$ . Furthermore, mass densities are: 8.2, 8.3, and 7.6 g/cm<sup>3</sup>. Lead chalcogenides are characterized as polar semiconductors as their properties are a mixed ionic-covalent nature. The melting points are 917, 1065, and 1114°C, respectively.

By varying the metal/chalcogen ratio, it is possible to introduce a defect structure that dopes the material p-type or n-type. An excess of Pb creates Te/Se/S vacancies and dopes n-type. Excess Te/Se/S creates Pb vacancies, and dopes p-type. The exact amount of solubility of excess Pb or Te/Se/S varies as a function of temperature; this is known as the solidus line, and is well documented for Pb salts.<sup>24</sup> PbTe can reach carrier densities of  $4 \times 10^{18} \text{ cm}^{-3}$  solely from deviations in stoichiometry. Furthermore, lower temperature annealing in the presence of the appropriate vapor can lower carrier concentrations to  $10^{16} \text{ cm}^{-3}$ . The appropriate doping range for Pb salts for TE applications is in the  $10^{19} - 10^{20} \text{ cm}^{-3}$  range.

For most impurities, with the exception of Group III atoms, that act as donors or acceptors, one can determine their action by simple electron counting. Halogens (I, Cl, Br) substituting for a chalcogen dope n-type, alkali metals (Na, K) substituting for Pb are acceptors. Alkali earths for Pb do not dope; Sb & Bi for Pb are n-type, whereas Sb for Te is p-type<sup>29</sup>. Exceptions to simple electron counting are the Tl, In, Ga, Al column, as the energy levels associated with their outermost electrons lies near the band gap. Tl is an acceptor<sup>37</sup>, Al a donor; In is a donor below room temperature<sup>44</sup>, above it is a trap in the band gap. Ga is a donor<sup>45</sup>, albeit with two apparent levels, one in the conduction band, the second in the band gap. Ag substitutes for Pb as an acceptor until concentrations  $\sim 10^{19} \text{ cm}^{-3}$ , excess silver then goes interstitial and acts as a donor.<sup>46</sup>

At  $T=0\text{K}$ , the valence band of PbTe consists of a “light” upper valence band (UVB) at the four L-points of the Brillouin zone, and a “heavy” lower valence band (LVB) broadly distributed over the zone near the  $\Sigma$ -points and between the L and  $\Sigma$ -points. The UVB is

ellipsoidal, with effective masses:  $m_{//[111]}^* \sim 0.24 \pm 0.05 m_e$ ;  $m_{\perp[111]}^* \sim 0.023 \pm 0.001 m_e$  at the band edge, and thus is strongly elongated along the [111] direction.<sup>47,24</sup> The lowest conduction band (CB) is nearly symmetric with the UVB; it also consists of elongated ellipsoids,  $m_{//[111]}^* \sim 0.24 \pm 0.05 m_e$ ;  $m_{\perp[111]}^* \sim 0.024 \pm 0.001 m_e$ <sup>24</sup>. The ellipsoids in PbS are less elongated than in PbTe, the anisotropy coefficient falls from  $\sim 10$ -14 in PbTe to  $\sim 1.5$  in PbS. The UVB:  $m_{//[111]}^* \sim 0.105 \pm 0.015 m_e$ ;  $m_{\perp[111]}^* \sim 0.075 \pm 0.01 m_e$ , the CB:  $m_{//[111]}^* \sim 0.105 \pm 0.015 m_e$ ;  $m_{\perp[111]}^* \sim 0.08 \pm 0.01 m_e$ <sup>24</sup>

The direct energy gap at L-point is:<sup>48</sup>

$$\varepsilon_g = 171 + [164 + 0.19(T+20)^2]^{1/2} \text{ meV} \quad (78)$$

and increases with  $T$ . This behavior is unusual.<sup>49</sup>

PbS has a band structure almost identical to PbTe, with a slightly larger direct L-point energy gap, but a very similar temperature-dependence (as does PbSe):<sup>48</sup>

$$\varepsilon_g = 263 + [400 + 0.265 T^2]^{1/2} \text{ meV} \quad (79)$$

## Electronic Band Structure Fits

In this section, we continue my earlier developments of the electronic structure of the lead chalcogenides studied, and by fitting the experimental data we can calculate relevant material parameters, such as Fermi energy, carrier mobility, scattering parameter, effective mass or density of states. These fits are known as the method of the four coefficients:  $\alpha$ ,  $R_H$ ,  $N$ , and  $\rho$ . The fits cannot be used when there is more than one set of degenerate bands that contribute to conduction, but are suitable for solids like Ge, Si, PbTe, PbSe, and PbS where the Fermi surface consists of multiple ellipsoids. Thus it will

not work at temperatures where thermally excited intrinsic conduction exists, nor can one analyze a solid where two bands at non-symmetric regions in the Brillouin zone exist.

Repeating Eq. 38

$$\gamma(\varepsilon) = \varepsilon \left( 1 + \frac{\varepsilon}{\varepsilon_g} \right) = \frac{\hbar^2}{2} \left( \frac{\mathbf{k}_{\parallel}^2}{m_{\parallel}^*} + \frac{2\mathbf{k}_{\perp}^2}{m_{\perp}^*} \right) \quad (80)$$

It becomes useful to use normalized energy  $x = \varepsilon/K_B T$  and accordingly, its derivative

$dx = \frac{1}{k_B T} d\varepsilon$ . The number of holes/electrons is the integral of the energy dispersion

relation multiplied by the derivative of the Fermi function:

$$n = \frac{(2m^* k_B T)^{3/2}}{3\hbar^3 \pi^2} \int_0^{\infty} (\gamma(x))^{3/2} \left( -\frac{\partial f}{\partial x} \right) dx \quad (81)$$

This is an alternative method than that presented earlier which was the integral of the density of states times the Fermi function.

As developed in Ref. [50], the four measured transport properties are detailed:

$$n = \frac{(2m^* k_B T)^{3/2}}{3\hbar^3 \pi^2} \frac{q^2}{m^*} \int_0^{\infty} \frac{(\gamma(x))^{3/2}}{\gamma'(x)} \tau(x) \left( -\frac{\partial f}{\partial x} \right) dx \quad (82)$$

$$\alpha = \frac{k_B}{q} \left( \frac{\int_0^{\infty} \frac{(\gamma(x))^{3/2}}{\gamma'(x)} x \tau(x) \left( -\frac{\partial f}{\partial x} \right) dx}{\int_0^{\infty} \frac{(\gamma(x))^{3/2}}{\gamma'(x)} \tau(x) \left( -\frac{\partial f}{\partial x} \right) dx} \right) \quad (83)$$

$$R_H = \frac{3K(K+2)}{(2K+1)^2} \frac{1}{nq} \left( \frac{\int_0^{\infty} \frac{(\gamma(x))^{3/2}}{(\gamma'(x))^2} x \tau^2(x) \left( -\frac{\partial f}{\partial x} \right) dx \int_0^{\infty} (\gamma(x))^{3/2} \left( -\frac{\partial f}{\partial x} \right) dx}{\left( \int_0^{\infty} \frac{(\gamma(x))^{3/2}}{\gamma'(x)} \tau(x) \left( -\frac{\partial f}{\partial x} \right) dx \right)^2} \right) \quad (84)$$

$$N = R_H \sigma \frac{k_B}{q} \left( \frac{\int_0^{\infty} \frac{(\gamma(x))^{3/2}}{\gamma'(x)} x \tau^2(x) \left(-\frac{\partial f}{\partial x}\right) dx}{\int_0^{\infty} \frac{(\gamma(x))^{3/2}}{(\gamma'(x))^2} \tau^2(x) \left(-\frac{\partial f}{\partial x}\right) dx} - \alpha + x_F \right) \quad (85)$$

These equations are solved simultaneously to calculate the unknown parameters. In this case, as before, we have assumed that the relaxation time is related to a power law of the electron energy. These equations above are valid for both degenerate and non-degenerate doping levels.

### Doping PbTe with Aluminum

While the group III elements have been extensively studied in PbTe<sup>39,44,45</sup>, including in this dissertation with Tl, transport studies of Al substituted for Pb are missing, prior to this work. A literature search only found that the Al impurity level in PbTe has been seen optically 300 meV above the conduction band edge at low temperature.<sup>51</sup> Thus, we synthesize and analyze the behavior of Al in PbTe substituted for Pb. Material preparation techniques are discussed in the Thermoelectric Methods section. The samples are Pb<sub>1-x</sub>Al<sub>x</sub>Te<sub>1</sub> with x=0.125%, 0.25%, 0.5%, & 1%.

Galvanomagnetic and thermomagnetic data of the samples are shown in Figure 18 as a function of temperature at zero magnetic field. We will begin our interpretation of the data with  $n$ , which is calculated here from the  $R_H$  assuming a hall prefactor of unity,  $n=1/eR_H$ . As discussed previously, the hall prefactor is a function of the dominant scattering mechanism, which in these samples changes over temperature. This causes the

slight temperature dependence of  $n$ . For  $x=0.125\%$  (or  $1.85 \times 10^{19}$  Al atoms per  $\text{cm}^3$ ),  $x=0.25\%$ , and  $0.5\%$ , the doping efficiency is approximately 2 electrons for 3 Al atoms (inset). However, above  $x=0.5\%$ , the hole concentration saturates. The cut surface and powder of the  $x=1\%$  ingot reacted and turned black upon cutting in water, presumably from reacting excess non-bonded Al or  $\text{Al}_2\text{Te}_3$ , which indicates that the solubility limit of Al in PbTe is between  $0.5\%$  and  $1\%$ .

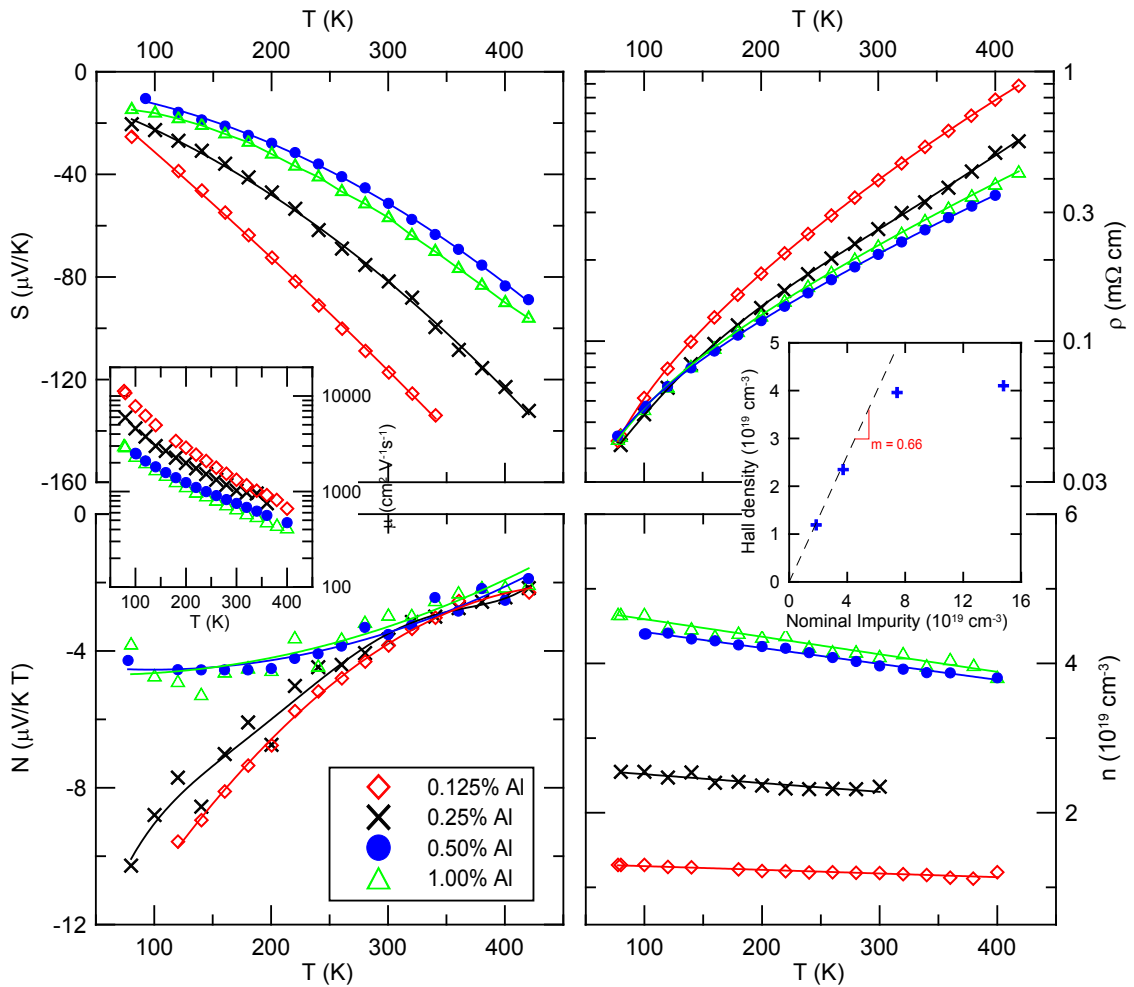


Figure 18:  $\alpha$ ,  $\rho$ ,  $N$ , and  $n$  of  $\text{Pb}_{1-x}\text{Al}_x\text{Te}$ . The inset shows the carrier concentration from Hall measurements as a function of nominal Al concentration. Symbols are experimental points; lines are added to guide the eye.

The electrical resistivity at 300K monotonically decreases Al concentration. Electrical mobility deduced from  $n$  and  $\rho$  at 300K is quite high,  $1300 \text{ cm}^2/\text{Vs}$  for  $x=0.125\%$ , and dropping to  $750 \text{ cm}^2/\text{Vs}$  for  $x=0.5\%$  (see inset). This is preliminary evidence for lack of a resonant level, as electrical mobility is a strong function of  $m^*_D$  and these values are too high for an increase in of  $m^*_D$  over the conduction band of PbTe at 300K<sup>39</sup>. In contrast, PbTe:TI has a 300K  $\mu \sim 30 \text{ cm}^2/\text{Vs}$ , because TI is a known resonant level. Interestingly,  $\rho$  for all samples converges at low temperature.  $\alpha$  above 200K is approximately linear with temperature, as expected from the metallic resistivity and the Mott relation for degenerate semiconductors. Below 200K, we note nonlinearity in  $\alpha$ , which can possibly be ascribed to change from mostly acoustic phonon scattering at low temperature toward more optical phonon scattering at high  $T$ ; however this also occurs at the temperatures where  $\rho$  converges. The magnitude of  $\alpha$  decreases with increasing electron density, as expected. Furthermore, a line drawn through high temperature slope of  $\alpha$  does not pass through zero at 0K, which probably arises from the previously discussed reasons for the nonlinearity in  $\alpha$ . Nernst has two distinct temperature dependences, split between low and high amounts of Al impurity and has a similar magnitude to other similarly doped n-type PbTe.<sup>29</sup> Figure 19 plots the Pisarenko relation at 300 K. The full line is calculated for optical phonon scattering and the  $m^*_D$  of the L-point in the conduction band of PbTe. The data points for Al-doped samples lie on the calculated line, and the enhancement of  $\alpha$  customarily observed for resonant levels<sup>37,30</sup> is thus not present.

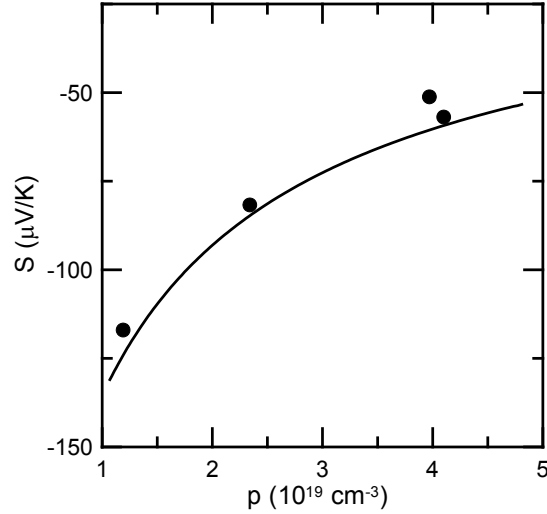


Figure 19: Pisarenko plot for  $\text{Pb}_{1-x}\text{Al}_x\text{Te}$ . Symbols are experimental points, the solid line is calculated for the lowest conduction band in PbTe.

Further analysis of the data is possible using the “method of the four coefficients” using degenerate statistics as discussed previously and results are shown in Figure 20. The Fermi energy  $\varepsilon_F$  from transport results reported here lies well below the optical measurement that place the Al level at 300 meV above the bottom of the conduction band. The effective mass in Figure 17 is, if anything, a little lighter than  $m^*_{D}$  of the CB of undoped PbTe ( $m^* \sim 0.28 m_e$  at  $n=2 \times 10^{19} \text{ cm}^{-3}$  and  $m^* \sim 0.32 m_e$  at  $n=4 \times 10^{19} \text{ cm}^{-3}$ ).<sup>47</sup> This slightly smaller  $m^*_{D}$  correlates well with the PbTe:Al samples lying just under the calculated Pisarenko relation  $\alpha(p, \lambda)$ . The scattering parameter  $\lambda$  is indicative of optical phonon scattering, but much lower than expected for resonant scattering.<sup>52</sup>

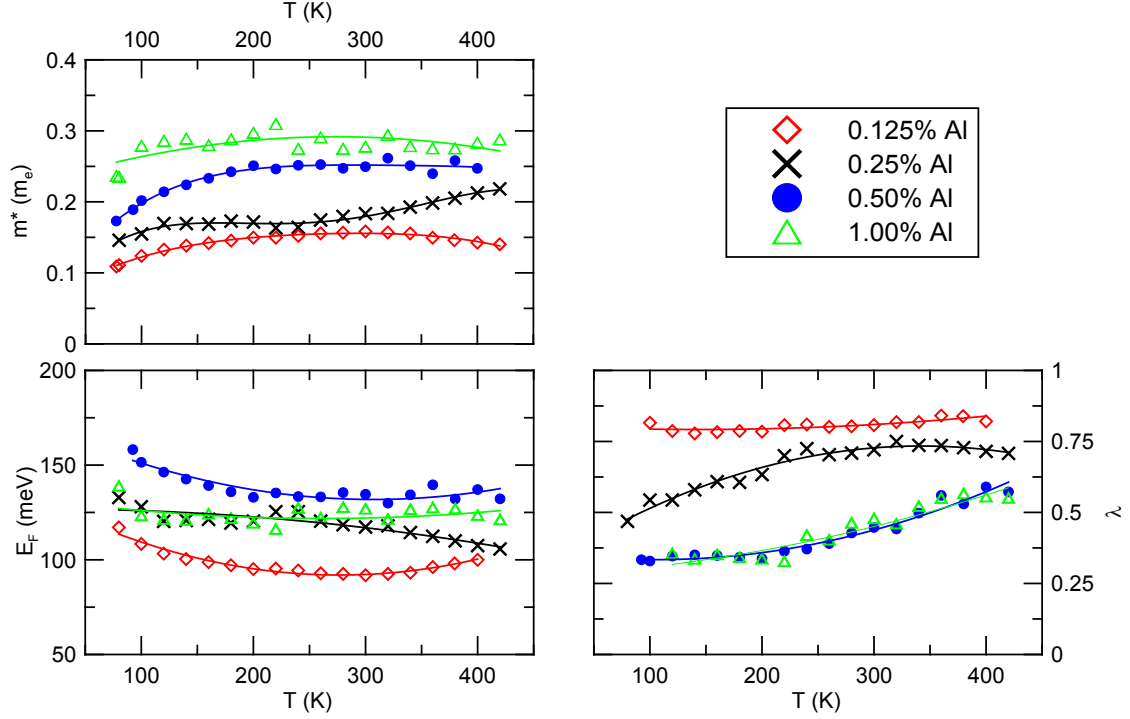


Figure 20: Effective mass, Fermi level and scattering parameter for  $\text{Pb}_{1-x}\text{Al}_x\text{Te}$ .

In summary, Al is a nearly-monovalent donor, whose energy level lies deep in the conduction band and does not increase the thermopower over the Pisarenko relation. If it is a resonant level at all, Al concentrations far above the solubility limit need to be used to place the Fermi level near the Al impurity level. We cannot rule out the possibility of resonant behavior at high temperature; as indium leaves the PbTe conduction band at  $\sim 300\text{K}$ , the Al impurity level likewise may move lower into an energetically favorable position with respect to the Fermi level at higher temperatures. Double doping with another n-type dopant such as iodine would be required. In general, the mobility of Al-doped material is quite good, so that it might prove a practical donor as a replacement for the typical halogen donors.

## PbTe: Upper/Lower Valence Bands Temperature Dependence

The established literature<sup>24,53</sup> reports a crossing of the light and heavy hole bands of PbTe below the operating temperature range of thermoelectric devices; it is this crossing that has been invoked<sup>36</sup> to explain the high  $\alpha^2\sigma$  in *p*-type PbTe, even though no equivalent band exists to explain the favorable  $\alpha^2\sigma$  of *n*-type material.<sup>54</sup> It is possible, however, that the reason for similar *zT* performance in *n*-type and *p*-type material is the loss in thermopower in the *p*-type material at elevated temperature from interband scattering, which we subsequently show can indeed cause the thermopower in *p*-type PbTe alloys to go negative. We present new experimental transport data that sheds light on the nature of this crossing.

In PbTe at low temperature ( $T < 80\text{K}$ ), the energy separation between the maxima of the UVB and the LVB is  $\Delta\varepsilon_v(0\text{ K}) = 160\text{-}180\text{ meV}$ .<sup>55,56</sup> Because it consists of many local minima distributed over the Brillouin zone, the density of states of the LVB is much higher than that of the UVB, with a DOS mass of the order of  $m_{DOS-\Sigma}^* \sim 0.6\text{ to }2.5 m_e$ <sup>47</sup> (which is at least double the UVB at L-point). However, due to the highly distorted and anisotropic nature of the UVB, characterizing a  $m_{DOS}^*$  is conceptually misleading. This gives the LVB holes a higher thermopower than the UVB holes, and is favorable to *zT* to have the Fermi level ( $\varepsilon_F$ ) in the LVB. It is clear that at operating temperatures of thermoelectric devices near 600-800 K, the LVB of heavily-doped ( $p > 5 \times 10^{19}\text{ cm}^{-3}$ ) PbTe is populated, and contributes to the high *zT* of the material at these temperatures.

The position of the LVB in PbS is less well established than for PbTe, and estimated at  $\Delta\varepsilon_v > 300$  meV at 0 K,<sup>56</sup> we know of no data on the  $T$ -dependence of the LVB edge with respect to the UVB edge in PbS.

The transport properties of the valence band of heavily  $p$ -type doped PbTe have been extensively investigated,<sup>57,58,59,60,61</sup> and are summarized in Ravich<sup>24</sup> and Khoklov.<sup>62</sup> The temperature-dependence of  $\Delta\varepsilon_v(T)$  is such that at  $T$  above some temperature  $T_0$ , defined by  $\Delta\varepsilon_v(T_0) = 0$ , PbTe turns into an indirect gap semiconductor with the CB minimum at L-point and the maximum of the valence band is the LVB near  $\Sigma$ -points. In the older literature, two very different temperature dependences for  $\Delta\varepsilon_v(T)$  above about 80K (bands move little with  $T < 80$ K because the thermal expansion becomes small) are reported (Figure 21). Allgaier and Houston<sup>63</sup> suggest and Rodgers<sup>64</sup> reformulates<sup>57</sup>:

$$\Delta\varepsilon_v(T) \sim 0.16\text{eV} - 2.2k_B T = 160 - 0.19 T \text{ meV}, \quad (86)$$

and apparently independently Airapetyants<sup>57</sup>:

$$\Delta\varepsilon_v(T) \sim 180 - 0.2 T \text{ meV} \quad (87)$$

while<sup>24,65,66</sup> suggest:

$$\Delta\varepsilon_v(T) \sim 170 - 0.41 T \text{ meV} \quad (88)$$

If Eqs. 85-86 hold,  $T_0 \sim 800$ K and the band crossing is not important in the  $zT$  of  $p$ -type PbTe at operating temperatures, although the concentration of thermally-induced or chemically-placed holes in the LVB is still very important at  $T > 600$  K; if Eq. 87 holds  $T_0 \sim 415$ K, and PbTe is an indirect-gap semiconductor in the relevant  $T$  range. Curiously, the values of  $(d\Delta\varepsilon_v/dT)$  vary by a factor of two, with Eq. 87 having the same temperature coefficient as the direct gap (Eq. 66):  $(d\Delta\varepsilon_v/dT) \sim (d\varepsilon_g/dT)_{T < 420 \text{ K}}$ ; this coincidence is

counter-intuitive, because  $\varepsilon_g$  is dominated by spin-orbit interactions, and is of very different physical origin than the LVB structure. We now critique the existing experimental literature cited in support of either Eqs. 86-87 or Eq. 88.

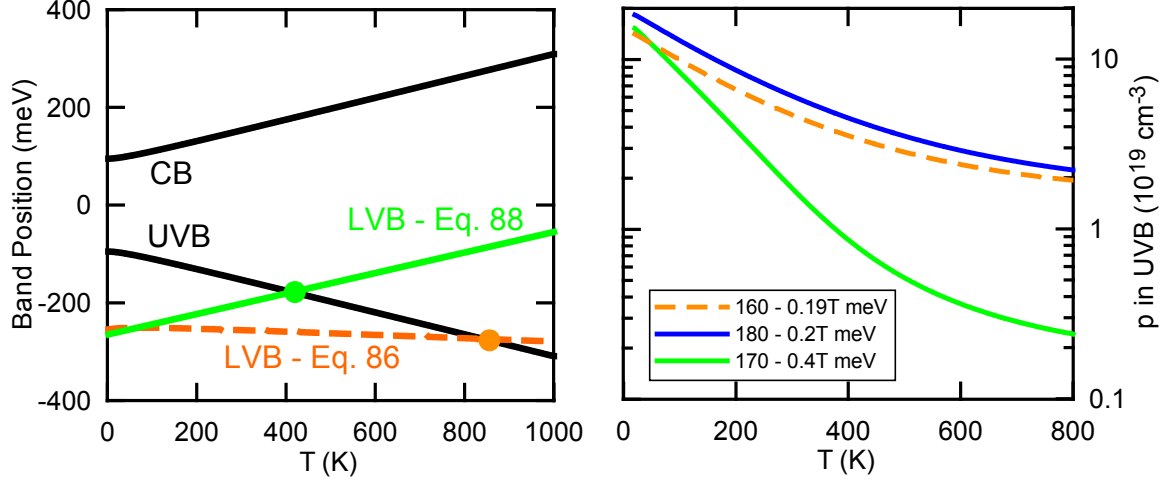


Figure 21: (left panel) Proposed band structure of PbTe based on contradicting literature and UVB hole density availability for the two  $\Delta\varepsilon_v(T)$ . (right panel) The curves are the number of holes in the UVB at the location where  $E_F$  crosses into the LVB.

There is an abundant literature summarized in compilations in Landolt-Börnstein<sup>47</sup> and Ravich<sup>24</sup> that implies  $T_0 \sim 420$  K. The experimental evidence appears strong, because it consists of two independent measurements: optical measurements by Tauber<sup>65</sup> and a strongly  $T$ -dependent Hall coefficient  $R_H$  ( $T > 80$  K) which was confirmed experimentally by several manuscripts. In Ref. [65] high-temperature optical absorption data versus wavelength were extrapolated to zero, and these intercepts were interpreted as giving a net optical energy gap. This gap then appears to be  $T$ -dependent following Eq. 66 up to about 400 K, above which the  $T$ -dependence appears to vanish:<sup>67</sup> so for  $T_0 \sim 400$  K,  $(d\varepsilon_g/dT)_{T>T_0} = 0$ , while  $(d\varepsilon_g/dT)_{T<T_0} = 0.43 \pm 0.02$  meV K<sup>-1</sup>, supporting Eq. 76. This

interpretation was influenced by the behavior of  $R_H(T)$  near the same temperature, which is discussed below. However, because of (1) Fermi surface smearing, (2) the effect of indirect (L- $\Sigma$ ) optical transitions which require electron-phonon interactions, and (3) the non-parabolicity of the bands (Eq. 46), the high-temperature energy-dependent absorption curves become very difficult to interpret; simply picking a slope through them and extrapolating that as is done in Ref.[65] is not conducive to unambiguously determine  $\varepsilon_g$  and  $\Delta\varepsilon_v$ , as these values depend very strongly on the energy range selected for the extrapolation. Furthermore, in other very old literature on optical absorption,<sup>68</sup> the optical absorption spectra of PbTe, PbSe and PbS all three show a similar temperature-dependence, yet only in PbTe are the results interpreted as above. Finally, accepting Eq. 88 requires ignoring other experimental results such as the dielectric measurements of Dixon and Riedel.<sup>69</sup> Very recently, Ekuma et al,<sup>70</sup> calculate several properties of PbTe using first principles and critique portions of the literature that we have; they suggest that the old optical measurements do not correctly reflect the behavior of the energy gap

Equation 86 is based on earlier work by Dixon and Riedel<sup>69</sup> who report that the second hole band is still 80 meV below the UVB at 300 K, and Allgaier and Houston,<sup>63</sup> and Rodgers<sup>55</sup> explain how the optical data of Tauber et al.<sup>65</sup> are in fact compatible with a slope of  $d\Delta\varepsilon_v(T)/dT = -0.2 \text{ meV K}^{-1}$  if one takes into account the temperature dependence of the effective mass, and arises from the non-parabolicity (Eq. 46) and the temperature-dependence of the direct L-point gap, Eq.66. These calculations are prone to large error,

however, as the authors estimate only 10-20% of the carriers are in the LVB in their specimens.

Turning now to the use of  $R_H(T)$  to justify (76), there are several difficulties. Firstly, there are extensive discussions in the old literature on the strange variations of  $R_H(T)$ , especially in Na-doped PbTe, and many alternative conclusions are suggested such as the possible existence of Na-Te vacancy complexes. Secondly, the literature used for  $R_H(T)$  does not specify what field the Hall resistances were measured at, only that it is fixed  $\pm$ -fields. This will give some measurements a negative hall slope if  $B < 0.5T$  at elevated  $T$ , but a positive slope if  $B > 1.5T$ . Thirdly, the Hall coefficient  $R_H$  is related to the carrier concentration  $p$  through the Hall prefactor  $r_H$  in the relation  $R_H = r_H / p \cdot q$ . The prefactor  $r_H$  is rarely independently experimentally determined, one article does<sup>71</sup> in the group IV-VI rocksalt semiconductors: it has been shown to vary between near unity and 0.6 (in heavily  $p$ -type SnTe), and to have a very strong and non-monotonic dependence on doping level. A discussion of  $r_H(p, T)$  is given by Allgaier.<sup>61</sup> Most important, however, is the nature of the maximum in  $R_H(T)$  at  $\sim 480K$  that is used<sup>24</sup> to justify the LVB and UVB band crossing. A maximum in  $R_H(T)$  in a 2-band system will occur when the conductances of the two bands are equal. It is not clear why the two bands conductances would be equal at  $\Delta\varepsilon_v = 0$  as the conductances of the LVB and UVB are functions of carrier density, mobilities, etc – and not just band crossing. Furthermore, as is very evident in Ref [66], the maximum in  $R_H(T)$  at 480K is followed by a negative  $R_H$  above  $\sim 600K$ . This not only masks the true maximum of  $R_H(T)$  but is attributed to thermally activated electrons, which we calculate later cannot be justified. Furthermore, the equations for  $R_H(T)$  would need to be modified to account for the third conductor at high

temperature, the electron pocket and then the local maximum in  $R_H(T)$  would not correspond to  $\Delta\varepsilon_v=0$ .

Lastly, there has been discrepancy from comparing the temperature and concentration  $p$  dependence of  $R_H(p,T)$  with the thermopower  $S(p,T)$  at 300 K. Experimentally, Airapetyants<sup>57</sup> shows at 300K a deviation in the Pisarenko plot  $S(p)$  from that calculated for the UVB beginning at  $3-4 \times 10^{19} \text{ cm}^{-3}$  holes, which is fully departed  $5.5 \times 10^{19} \text{ cm}^{-3}$  holes. He assumed  $r_H=1$ , whereas Crocker and Rodgers<sup>60</sup> show that at these carrier densities,  $r_H$  is  $\sim 1.3$  (at these carrier densities, the  $r_H$  vs.  $p$  plots are very noisy, with  $1.1 < r_H < 1.7$ ). This will contradict Eq. 76 from which we calculate the UVB will hold  $1.9 \times 10^{19} \text{ cm}^{-3}$  holes at 300K (Figure 21) whereas taking the temperature dependence (74-75), we calculate that the UVB can hold  $5.2 \times 10^{19} \text{ cm}^{-3}$  holes at 300K before the Fermi level reaches the top of the LVB, thus giving further credence to  $T_0 \sim 800\text{K}$ .

If Eq. 76 holds, then LVB  $\sim 50 \text{ meV}$  from UVB at 300K, or the UVB has  $p \sim 1.2 \times 10^{19} \text{ cm}^{-3}$  holes, and a thermopower of  $\sim 120 \mu\text{V/K}$  under acoustic phonon scattering. This is not where the deviation is seen by Airapetyants; it is at  $50-55 \mu\text{V/K}$  which corresponds to  $\sim 5 \times 10^{19} \text{ cm}^{-3}$  holes and is  $\sim 100\text{meV}$  into the UVB, correlating well with Eq. (4)

### **PbTe-PbS: Tl**

Here, to increase  $zT$ , we seek to combine the enhanced power factor of  $\text{PbTe:Tl}$ <sup>37</sup> with a lattice thermal conductivity ( $\kappa_L$ ) reduced through alloy scattering of phonons by isoelectronic substitution of S for Te. V. Jovovic<sup>72</sup> investigated the substitution of Se for

Te; however he found that the necessary hole concentrations required for high- $zT$  in this system were not attainable due to chemistry issues. Thus, we synthesized  $\text{Pb}_{0.98}\text{Tl}_{0.02}\text{Te}_{1-x}\text{S}_x$  with  $0 \leq x \leq 0.16$  and performed the appropriate heat treatment to obtain solid solutions, as detailed previously. In binary PbTe, Tl was calculated to induce two specific energy levels, a hyper-deep state (HDS) and a deep state (DDS), with the latter being in the upper valence band (UVB) and enhancing the thermopower. The Tl-DDS was calculated to couple to the Te  $5p$ -states.<sup>73</sup> Here we investigate the behavior of the Tl resonant level, both experimentally and using band structure calculations, as Te is being partially substituted with S. The band structure calculations were performed by B. Wiendlocha<sup>39</sup> and are detailed below. One complication in  $p$ -type PbTe alloys is the presence of a lower valence band (LVB), which at the highest temperatures might contribute to the high  $zT$  in  $p$ -type samples doped solely with Na,<sup>74</sup> an explanation that doesn't address the experimental results on  $n$ -type PbTe can reach  $zT=1.4$  without any associated heavy conduction band.<sup>54</sup> This indicates that the main factor is the low thermal conductivity of PbTe, which itself has recently been attributed to lattice instabilities.<sup>42</sup> The Tl energy level adds  $g(\varepsilon)$  to the valence band of PbTe, but there is uncertainty in the literature about the energy at which this happens: numbers cited are about 60 meV below the top of the UVB in PbTe, 200 meV in PbSe, and 100 meV in PbS<sup>75,76</sup> (where it is degenerate with the LVB). Experimentally, these energies appear to vary with the concentration of Tl in the sample and different results are deduced from different experiments (transport, optical or tunneling). Tl substituted for Pb is reported to achieve doping levels of  $5 \times 10^{19} \text{ cm}^{-3}$  in PbS,  $12 \times 10^{19} \text{ cm}^{-3}$  in PbSe, and  $9 \times 10^{19} \text{ cm}^{-3}$  in PbTe,<sup>71</sup> values that do not scale properly

with the energy levels reported above. Here, we show that Tl contributes  $g(\varepsilon)$  starting almost at the top of the UVB.

Thermopower,  $\rho$ ,  $N$ , and the hole concentration  $p$  as calculated assuming  $p=1/R_H q$  are plotted in Figure 22. While no systematic trend in the magnitude of  $\alpha$  is observed with  $x$ ,  $\alpha$  of all samples is approximately linear in  $T$ , indicating a single carrier system.  $N$  is small and negative for all samples, which indicates that acoustic phonon scattering dominate. Samples containing sulfur have lower  $p$  than the sulfur-free samples, with  $p$  decreasing approximately monotonically with  $x$ . All samples with sulfur have lower  $\rho$  than the  $x=0$  sample at  $T < 400$  K, which seems to contradict the observed decrease of  $p$  with  $x$ ; thus hole mobility must play a dominant role. Interestingly, the temperature dependence of  $\rho$  for  $x > 0.08$  is different than for  $x \leq 0.08$ . The slight differences between the results at  $x=0$  and those in Ref. 37 are attributed to different material processing techniques: bulk ingots are used here and hot-pressed ball milled material in Ref. 37. These have different anneal schedules, which affects the solubility of Tl in PbTe and the defect concentration in PbTe.

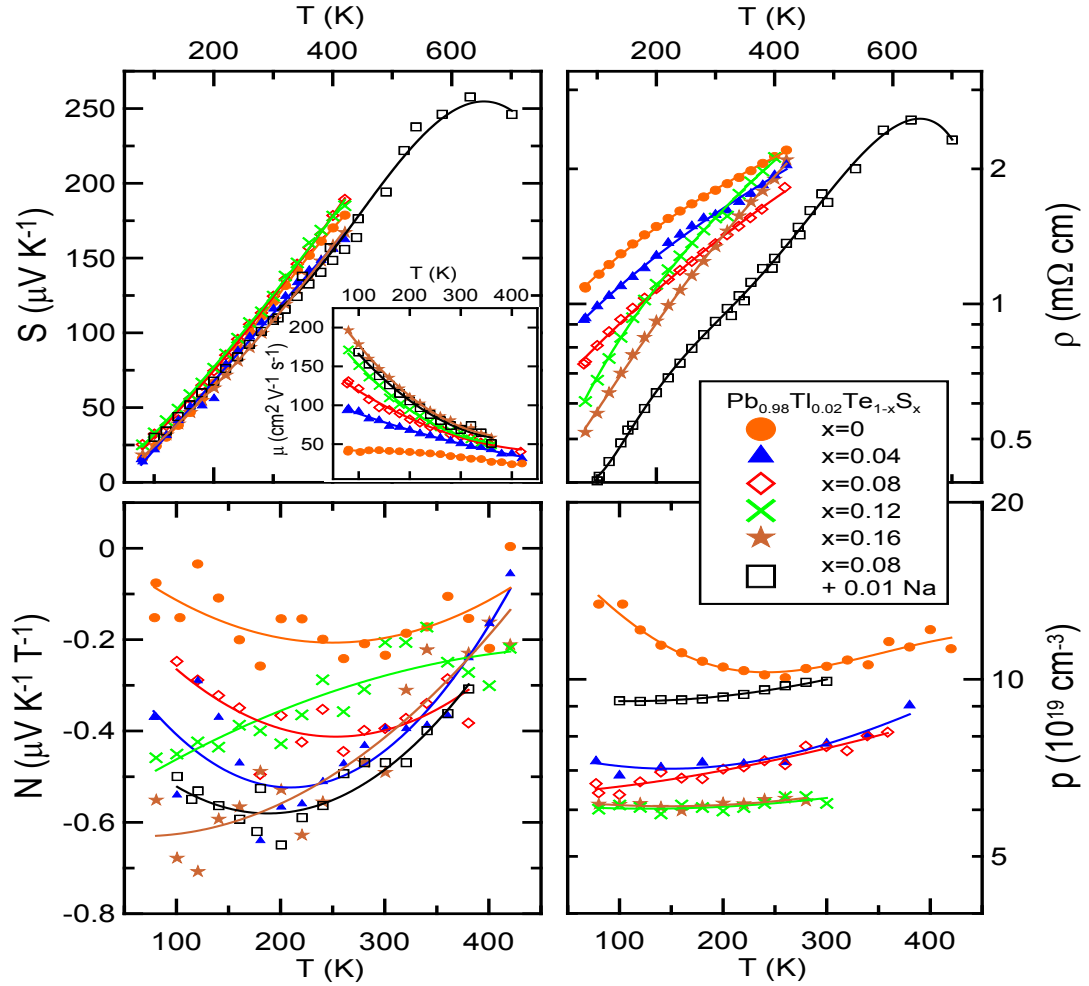


Figure 22:  $\alpha$ ,  $\rho$ ,  $N$ , and RH of  $\text{Pb}_{0.98}\text{Tl}_{0.02}\text{Te}_{1-x}\text{S}_x$ . The inset shows the carrier concentration from Hall measurements as a function of nominal Al concentration. Symbols are experimental points; lines are added to guide the eye.

Figure 23 shows the calculated  $\alpha$  vs. carrier concentration  $\alpha(n)$  or “Pisarenko” relation at 300K as a full line for the upper valence band (UVB) of PbTe; there is a heavy lower valence band (LVB) which when reached in p-type PbTe<sup>77</sup> at hole doping concentrations  $p \sim 5 \times 10^{19} \text{ cm}^{-3}$ , gives a nearly constant  $\alpha$  of  $\alpha = 50\text{--}55 \text{ } \mu\text{V/K}$  invariant of  $p$ . As in Ref. 37, the samples reported here have Seebeck coefficients shown as data points in Figure 23 to

be  $\alpha \sim 120 \mu\text{V}/\text{K}$  at 300K, far above the Pisarenko relation. We conclude that the Tl impurity maintains at least partially its resonant properties in the compositions studied.

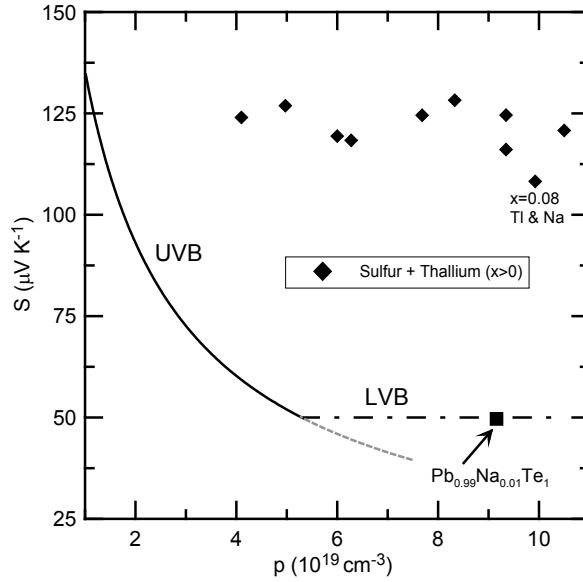


Figure 23: Pisarenko relation for PbTe-S with Tl. The UVB and LVB lines are calculated for the upper and lower valence bands of PbTe.

A quantitative analysis is made using the method of the four coefficients described previously. At low temperature, where the Nernst data are less noisy and the materials are more degenerate compared to  $k_B T$ , the four measured transport properties  $\alpha$ ,  $N$ ,  $R_H$ , and  $\rho$  are used to calculate four unknown material parameters: the Fermi level  $\varepsilon_F$ ; the scattering parameter  $\lambda$ ; the hole mobility  $\mu$ ; and the density-of-states. The latter can be expressed in terms of a density-of-states effective mass  $m_D^*$  - here in the special case of PbTe:Tl alloys, we assume the bands are locally parabolic at  $\varepsilon_F$ , which is justified by the band structure calculations below and will be discussed subsequently. The  $g(\varepsilon)$  and  $m^*$  are connected with free-electron-like formula:

$$g(\varepsilon) = \frac{(m_d^*)^{3/2}}{\pi^2 \hbar^3} \sqrt{2\varepsilon_F} . \quad (89)$$

The hole density in this method is calculated using  $\varepsilon_F$  and  $g(\varepsilon)$  and is more accurate than that determined using  $p(T)=1/R_H(T)q$  as in Figure 22. As previously discussed, the method of the four coefficients includes<sup>37</sup> the effect of the Hall prefactor  $r_H(\lambda, K)$ . In practice, for Tl-doped samples, the  $g(\varepsilon)$  is severely affected; thus using the K for the valence band of PbTe would be incorrect. With a parabolic band,  $K=1$ , and thus the small change in the values of  $\lambda$  in Table 1 lead to a temperature dependent  $r_H(\lambda)$  which is reflected in  $p(T)$  in Figure 22. The Hall prefactor is considerably more T-dependant in Na:PbTe than in Tl:PbTe as will be shown in the section on PbTe-PbS: Na alloys.

The results for  $\varepsilon_F$ ,  $\lambda$ ,  $g(\varepsilon)$  or  $m^*$  are shown in Table 1, and the following conclusions can be drawn. Most importantly, the  $g(\varepsilon)$  at  $\varepsilon_F$  for 2%Tl at  $x=0$  ( $0.18 \text{ ev}^{-1}$  per formula unit) corresponds very well to the calculated value ( $0.24 \text{ ev}^{-1}$ ) below, and to the experimental value ( $0.3 \text{ ev}^{-1}$ ) determined from electronic specific heat measurements in a PbTe sample containing 1.4% Tl.<sup>78</sup> We note that the theoretical  $g(\varepsilon)$  calculations below illustrate that a non-parabolic Kane model, which would hold for the UVB, does not apply to the Tl resonant state. Secondly, the value for the scattering exponent  $\lambda \sim -0.5$  to 0 (the relative inaccuracy is due to the noise in  $N$ ) indicates that scattering is dominated by acoustic phonons ( $\lambda = -0.5$ ) with a modest contribution of optical phonon ( $\lambda = +0.5$ ), but with no evidence for a resonant scattering mechanism which would lead to  $\lambda > 3$  to 4.<sup>52</sup> Also, since resonant scattering is expected only at the lowest temperatures<sup>52</sup> because the effects of phonon scattering increase with temperature, resonant scattering would imply that  $\lambda$  should increase with decreasing temperature, the opposite of what is observed. Thirdly,

the calculated  $\varepsilon_F$  ( $60 \pm 10$  meV) is nearly constant with S content, indicating a pinned  $E_F$ . Fourthly, all samples retain a  $g(\varepsilon)$  above that of the UVB of PbTe. In spite of the slightly larger gap of PbS compared to that of PbTe and the resulting concomitant increase of  $g(\varepsilon)$  of the UVB with  $x$  in the absence of resonant levels, a decrease of  $g(\varepsilon)$  with increasing  $x$  is observed. Finally, the low-temperature mobility (Figure 22a inset) improves monotonically with increasing sulfur content, contrary to what is expected from alloy scattering.

Table 1: Fermi level, effective mass, scattering parameter, and density of states of TI doped  $\text{PbTe}_{1-x}\text{S}_x$ .

| Sulfur %  | $\varepsilon_F$ 80K | $\varepsilon_F$ 300K | $m^*$ 80K | $m^*$ 300K | $\lambda$ 80K | $\lambda$ 300K | $g(\varepsilon)_{\varepsilon_F, 80K}$ | $g(\varepsilon)_{\varepsilon_F, 300K}$ |
|-----------|---------------------|----------------------|-----------|------------|---------------|----------------|---------------------------------------|--|
|           | (meV)               | (meV)                | ( $m_e$ ) | ( $m_e$ )  |               |                | ( $\text{eV}^{-1}$ per f.u.)          | ( $\text{eV}^{-1}$ per f.u.)           |
| Pure PbTe | 60                  | 60                   | 0.14      | 0.17       | 0.00          | 0.00           | 0.006                                 | 0.008                                  |
| 0%        | 57                  | 57                   | 1.38      | 1.33       | -0.30         | -0.06          | 0.178                                 | 0.168                                  |
| 4%        | 53                  | 55                   | 1.18      | 1.18       | -0.50         | -0.12          | 0.134                                 | 0.137                                  |
| 8%        | 64                  | 58                   | 0.92      | 1.12       | -0.10         | 0.00           | 0.100                                 | 0.128                                  |
| 12%       | 57                  | 66                   | 0.98      | 0.86       | -0.27         | 0.14           | 0.103                                 | 0.091                                  |
| 16%       | 48                  | 66                   | 1.25      | 0.94       | -0.56         | -0.06          | 0.135                                 | 0.103                                  |
| 8%+ 1%Na  | 66                  | 67                   | 1.06      | 1.15       | -0.24         | -0.01          | 0.126                                 | 0.144                                  |

Figure 24 shows thermal conductivity  $\kappa$  for the samples versus temperature. Interestingly,  $x=0$  has the lowest  $\kappa$ . While sulfur lowers  $\kappa_L$ ,  $\kappa_e$  is higher in sulfur containing samples from their lower  $\rho$ . Furthermore, the reduction in  $\kappa_L$  from alloys scattering or nanostructuring is not dramatic due to the already low  $\kappa_L$  of pure PbTe from the optical phonons and dominance of Umklapp scattering. As the best  $zT$  is observed in the highest-doped samples, and because TI has a solubility limit in PbTe, we double

doped an  $x=0.08$  sample with 1 at% Na substituted for Pb: its properties are included in Figure 22 and Table 1.  $\alpha$  and  $\rho$  are lower than for the other samples due to the increased carrier density and  $\kappa$  is slightly higher (Figure 24) due to increased electronic  $\kappa_e$ . Electronic structure calculation like those described below show that Na-doping mainly changes the position of the Fermi level, acting as a simple acceptor without modifying the general shape of  $g(\epsilon)$  near  $\epsilon_F$ . The  $zT$ , (Fig. 4d), reaches 1.6 at 700K, and illustrates that indeed the positive aspects of resonant levels work independently of the effects of alloy scattering.

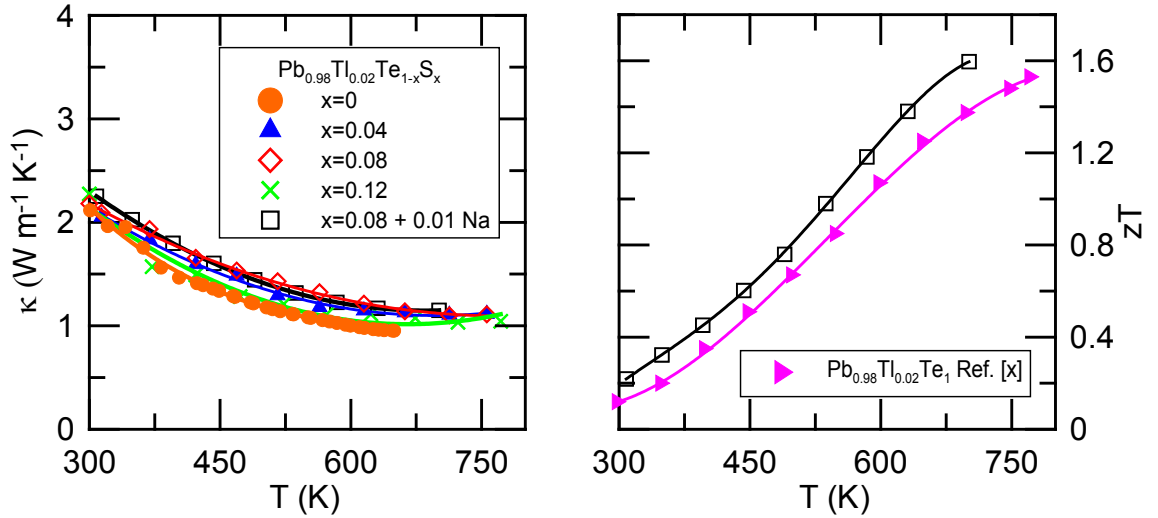


Figure 24: Thermal conductivity and  $zT$  of PbTeS:Tl alloys.

To enlighten the experimental trends in transport properties, and to clarify the criteria necessary for resonant levels to enhance  $zT$ , electronic structure calculations were performed by B. Wiendlocha using the Korringa-Kohn-Rostoker (KKR) Green function method<sup>79,80</sup> with the coherent potential approximation (CPA) used to treat disorder in

alloys. His results include both Se and S substitution and are summarized below in order to allow for a complete and coherent discussion of the experimental results.

The  $g(\varepsilon)$  was calculated for Se/S substitution for Te. The large-energy-scale effects are similar to those on PbTe:Tl; detailed changes upon S and Se doping will be discussed later. The locations of the S 3s and 3p energy bands (or Se 4s and 4p) follow those of corresponding Te 5s and 5p states. As in PbTe case<sup>73</sup> the  $g(\varepsilon)$  consists of four separate blocks: two low-lying s-like (5s electrons of Te and 6s of Pb) blocks, and valence and conduction bands (5p-Te and 6p-Pb) separated by the band gap (overestimated in our calculations by semi-relativistic approach). The Tl atoms create three sharp  $g(\varepsilon)$  peaks, corresponding to three impurity states typical for group-III elements in the lead salts. First is a semi-core d level (5d in Tl case) located about -10 eV below Fermi level. Second and third are the unusual 6s-like hyper deep (HDS, -5 eV below  $E_F$ ) and deep defect states (DDS, at  $E_F$ ), the latter being the one that influences the thermoelectric properties. The 6p Tl states are built into the valence band block lying between -5 eV and  $E_F$ . These calculations confirm an earlier report by Hoang.<sup>73</sup>

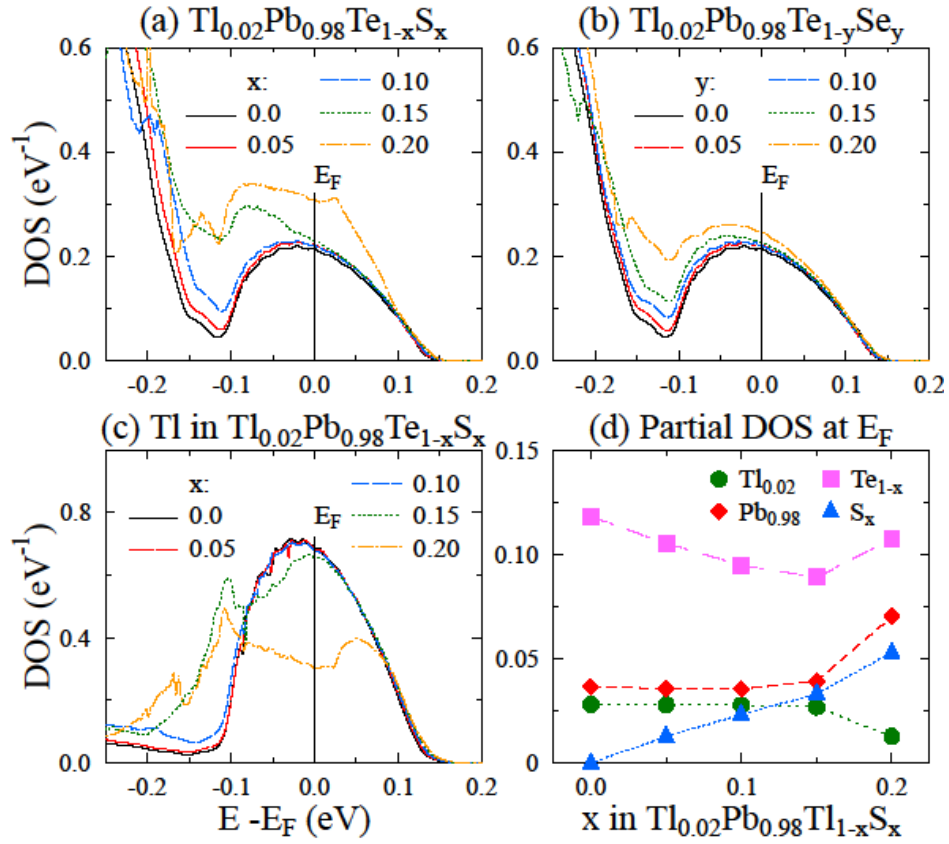


Figure 25: Density of states ( $g(\epsilon)$ ) of PbTeS-PbTeSe doped with Tl.

Both HDS and DDS states are formed by the interaction of Tl-s and Te-p orbitals, but they have different evolutions upon Te/Se and Te/S substitution. The relative contribution to the total  $g(\epsilon)$  for DDS states calculated at the Fermi level are 12% Tl, 50% Te, and 15% Pb, the rest arise from interstitial sites. The HDS is 46% Tl, 26% Te and 7% Pb. Formation of both HDS and DDS occurs only when Tl is present in PbTe, but HDS is more Tl-like and DDS is more Te-like. Because of this, Te/Se or Te/S substitution does not significantly modify the HDS, while important changes occur in the DDS.

The “hump” in  $g(\varepsilon)$ , created by the Tl atoms, is suggestive of the  $g(\varepsilon)$  for the “best thermoelectric” concept,<sup>28</sup> remains up to intermediate S/Se substitution levels. This  $g(\varepsilon)$  “hump” can be locally fitted using the square-root dependence on energy, a free-electron-like formula, but with constant factor:  $g(\varepsilon) = a\sqrt{\varepsilon_V - \varepsilon} - b$ , where  $a = 0.84 \pm 0.02$  (eV<sup>3/2</sup>),  $b = -0.1 \pm 0.005$  (eV<sup>-1</sup>). This observation justifies using the parabolic model for the four coefficients method used and reported in Table 1. The value of fitting parameter  $a$  corresponds to  $m_D^* \approx 1.5 m_e$ , which is close to the value calculated from the four coefficients method ( $m^* \approx 1.35 \pm 0.3 m_e$  for  $x = 0$ , see Table 1). Adding Tl to PbTe, in addition to doping it p-type, triggers the formation of resonant-yet-nearly-free-electron-like states, joining two features that are easily but erroneously perceived as contradictory.<sup>81</sup>

Using this equation for  $\alpha$  for degenerate bands that ignores the effect of scattering, and rewriting Eq. 45 as:

$$\alpha = \frac{\pi^2}{3} \frac{k_B}{q} k_B T \frac{g(\varepsilon_F)}{\int_{\varepsilon_F}^{\varepsilon_V} g(\varepsilon) d\varepsilon}, \quad (90)$$

gives  $90 \mu\text{V K}^{-1}$  at 300K from the  $g(\varepsilon)$  in Figure 25. This value is close to the experimental value given the simplistic formula, giving further credence to the calculated  $g(\varepsilon)$  in Figure 25.

We move now to the evolution of  $g(\varepsilon)$  with S/Te substitution. The  $g(\varepsilon)$  does not change much for  $x < 0.1$  (Figure 25); neither does the calculated Fermi level position with respect

to the valence band edge. The independence of the  $g(\varepsilon)$  on  $x$  is consistent with the constant  $\alpha$  at 300 K (Figure 23). The changes in  $g(\varepsilon)$  are visible above  $x=0.15$ , where the hump broadens and starts to join the main valence  $g(\varepsilon)$ , filling the valley which separated both regions and increasing the density of background states, which is unfavorable for  $zT$ .<sup>28</sup> Calculations (Figure 25) don't predict as abrupt a drop in total  $g(\varepsilon)$  as is shown in Table 2, but important decreases in partial  $g(\varepsilon)$  occur. Figure 25c presents the evolution of the TI partial  $g(\varepsilon)$  peak (mainly s-like) upon S/Te substitution. Starting at  $x=0.15$ , the  $g(\varepsilon)$  broadens, which causes the broadening of the whole DDS  $g(\varepsilon)$ , and the  $g(\varepsilon)$  at  $\varepsilon_F$  drops significantly for  $x=0.2$ . Figure 25d shows contributions to total  $g(\varepsilon)$  at the Fermi level coming from all the atoms, weighted by their concentrations. The Te contribution generally decreases with  $x$ , and this effect is present even if Te  $g(\varepsilon)$  is counted per atom (not multiplied by concentration). Adding the contributions of both Te and S to the  $g(\varepsilon)$  shows that the contribution of the S/Te site is constant up to  $x=0.15$ , but for  $x=0.2$  its value increases (samples with that concentrations could not be synthesized as solid solutions).

The loss of the resonant behavior of TI observed experimentally for  $x>0.08$ , is related to the broadening of the total and partial TI-  $g(\varepsilon)$ , the decrease in partial (mainly s-like) TI-  $g(\varepsilon)$  and the decrease in partial (mainly p-like) Te  $g(\varepsilon)$ . The calculations for the Se substitutions follow the experiment less well, and are included for completeness. Transport measurements by V. Jovicic<sup>39</sup> show a rapid decrease in  $g(\varepsilon)$  even at  $y=0.05$ , while in calculations results are qualitatively similar to those of S case (Figure 25b). For Se the calculated modifications to  $g(\varepsilon)$  are less pronounced and more gradual than for sulfur, which is intuitively understood since Se is chemically more similar to Te than S.

We tentatively conclude that the differences in observed experimental results between the PbTeS and PbTeSe systems may be ascribed to their different defect chemistry and anneal schedules, which allowed only for a more limited hole concentration and  $\varepsilon_F$  range to be explored in the Se/Te system.

The fundamental cause for the decreased efficiency of the Tl resonant level in boosting the thermopower as the Te concentration decreases is related to the lattice constant. B. Wiendlocha further computed  $g(\varepsilon)$  for 20% Se(S)/Te substitution ignoring changes in lattice parameter: the characteristic  $g(\varepsilon)$  hump was almost unchanged compared to the 0% Se/S case. This suggests that the decrease in lattice constant with Se or S substitution, rather than the electronegativity of the lighter chalcogens, plays a dominant role, that the effect is due to “chemical pressure”; in this model, the broadening of a thallium partial  $g(\varepsilon)$  peak is a pressure-driven enhanced hybridization of Tl s-orbitals with the valence bands of PbTe. The decrease in lattice constant affects the overlap between the Tl 6s states and the Te 5p, and thus the delicate balance between increases in  $g(\varepsilon)$  and nearly-free-electron behavior that lies at the origin of the thermopower enhancements. Since changes in lattice parameter made by Se/Te substitution are smaller, the effect made by insertion of Se atoms is expected to be weaker, at least in the spherical-potential semi-relativistic CPA calculations. He also simulated the opposite trend, i.e. performed computations for 2%Tl doped PbTe with a hypothetically larger lattice parameter (about 1.5%.) and found increases in both  $g(\varepsilon)$  and Seebeck coefficient of about 5%. This finding leaves open the possibility of a further increase in  $zT$  of the  $x>0$  alloys through usage of heat treatments designed to exploit the spinodal decomposition regime<sup>82</sup>, thus reducing

thermal conductivity via nanostructuring<sup>83</sup> instead of alloy scattering, and optimizing the lattice parameter to maximize the power factor.

The distortion in  $g(\epsilon)$  observed in  $\text{Pb}_{0.98}\text{Tl}_{0.02}\text{Te}$  is maintained for  $\text{Pb}_{0.98}\text{Tl}_{0.02}\text{Te}_{1-x}\text{S}_x$  alloys with  $x \leq 0.08$ . Tl continues to act as a resonant level, pinning the  $S$  at  $\sim 120 \mu\text{V/K}$  at 300K. The fact that the mobility in these alloys increases with  $x$  is surprising but is most likely due to the decrease in  $g(\epsilon)$  at  $\epsilon_F$  as shown in Table 1. For  $\text{Pb}_{0.98}\text{Tl}_{0.02}\text{Te}_{1-y}\text{Se}_y$  alloys, both carrier density and hole effective mass decrease with  $y$ , the Tl resonant level is partially lost, and the samples return to the Pisarenko curve for the UVB of PbTe. Electronic band structure calculations show that thallium 6s-states, coupled with Te 5p ones, create an excess  $g(\epsilon)$  in PbTe that evolves little with Se/Te and S/Te substitution for low concentrations, and dominates the thermopower at 300K. In Tl-doped PbTe and its alloys, the Tl 6s-states trigger the formation of sharp  $g(\epsilon)$  peaks, a behavior typically associated to more localized 3-d transition metal states, but with a free electron-like local energy dependence  $g(\epsilon) \sim \sqrt{\epsilon}$ . The decrease in lattice constant with the Se/Te and S/Te substitutions is calculated to be the origin of the smearing out of the Tl level at higher concentrations. The effectiveness of a resonant level in enhancing the thermoelectric power factor depends critically on the amount of overlap between the impurity states and the band structure of the host semiconductor. Too much overlap, induced here by the reduction in lattice constant, decreases the excess in thermopower; too little overlap creates states that are too localized and do not conduct well. The experimental data and corroborating theory indicate that this knowledge should be extendable to other thermoelectric materials.

## PbTe-PbS: Na

Heavily p-type doping PbTe with Na without Tl leads to an interaction between holes in the UVB and LVB; their temperature dependences have been debated in literature since they were first discovered. We present new experimental evidence about the valence band structure of PbTe and  $\text{PbTe}_{1-x}\text{S}_x$  alloys, and its effect on the thermoelectric figure of merit  $zT$ . Thermoelectric transport data on material doped by substitution of Na for Pb with  $x \leq 0.12$  are reported: consistently with other reports, heavily p-type ( $[\text{Na}] > 10^{19} \text{ cm}^{-3}$ )  $\text{Pb}_{0.99}\text{Na}_1\text{Te}_{0.92}\text{S}_8$  exhibits high power factors ( $>20 \mu\text{W}/\text{cm K}^2$ ) at elevated temperatures, a low lattice thermal conductivity, and  $zT \sim 1.55$  at 773K. The transverse Hall resistivity, when plotted as a function of magnetic field, shows a negative electron-like slope for ( $-0.5\text{T} < B < 0.5\text{T}$ ,  $T > 600\text{K}$ ); these are high-mobility electrons most likely induced in the L-point conduction band by photoconductivity. Another possibility is the relative minimum in the L6+ band between L-W in the Brillouin zone that is populated when the Fermi level reaches the LVB<sup>84</sup>. This occurs due to a change in topology in the Fermi surface between the LVB and UVB. Due to the local curvature of this band, an electron pocket should appear. However, Hall measurements taken at fixed positive and negative field do not reveal these electrons and thus give an artificially smaller Hall coefficient. This lack of knowledge leads to a misinterpretation instead as an increase in carrier concentration and results in an incorrect model for the relative positions of the heavy and light valence bands over temperature.

Selected temperatures of  $\rho_{xyz}(B)$  on  $\text{Pb}_{0.99}\text{Na}_{0.01}\text{Te}_{1-x}\text{S}_x$  are shown in Figure 26. At low  $T$ ,  $\rho_{xyz}(B)$  is clearly linear. However, at  $T \geq 600\text{K}$ , low field  $\rho_{xyz}(B)$  is negative ( $x=0.08$ )

or has a plateau, thus creating a nonlinearity. High field  $\rho_{xyz}(B)$  remains positive from the high density heavy holes. Hall is the most sensitive transport property studied here to high mobility carriers, as it is the mobility of the carrier squared that enters the multi-band Hall equation. Indeed, this low field regime of  $\rho_{xyz}(B)$  will adversely affect the calculation of carrier concentration or band structure at high temperature if its effects are not properly taken into account.

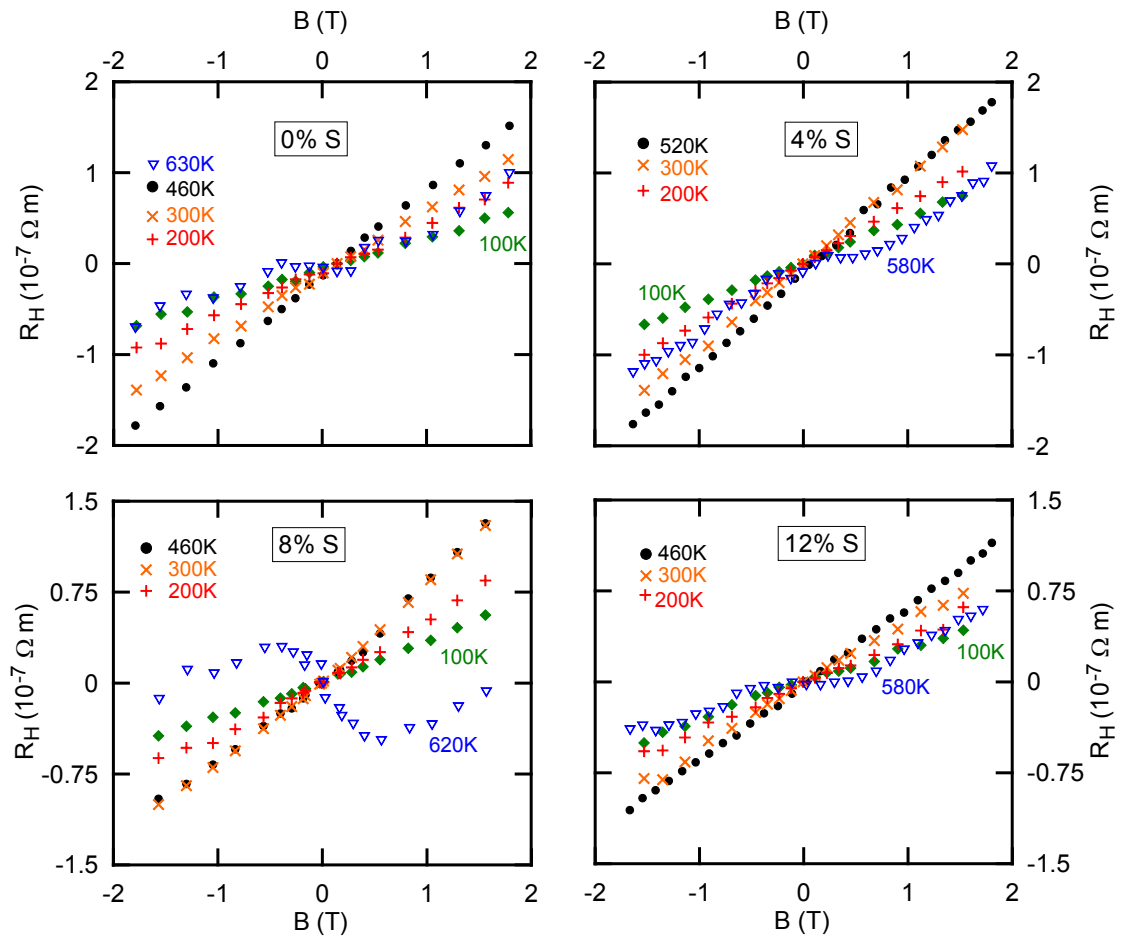


Figure 26: Hall resistances as a function of magnetic field for  $\text{Pb}_{0.99}\text{Na}_{0.01}\text{Te}_{1-x}\text{S}_x$ .

While we have experimentally shown an electron like behavior in  $\rho_{xyz}(B)$  at elevated temperatures, it remains an open question of how these electrons populate the CB.

Andreev<sup>58</sup> reports these electrons may be thermally activated, while we posit that these electrons are photo-induced carriers from the walls of the cryostat. Using Planck's law for black body radiation assuming that every photon with  $\varepsilon > \varepsilon_g(T)$  is absorbed by the PbTe thus creating an electron hole pair:

$$\int_{\varepsilon_g(T)}^{\infty} \frac{2\pi}{c^3 h^3} \frac{\varepsilon_p^2}{e^{\frac{\varepsilon_p}{k_b T}} - 1} \frac{A_s}{V_s} d\varepsilon_p, \quad (91)$$

we calculate in Figure 27 the photo-induced electron carrier density as a function of temperature. Here  $\varepsilon_p$  is the energy of the photon,  $A_s$  is the surface area of the sample, and  $V_s$  is the volume of the sample. Also on this plot is the low field slope of  $\rho_{xyz}(B)$  of  $x=0.08 + 0.01\text{Na}$  converted to a carrier density using  $n=1/R_H q$ , which is not very accurate. This falls within an order of magnitude of the calculations.

To accurately calculate the intrinsic electron carrier density as a function of extrinsic hole density and temperature we use the statistics laid forth by Blakemore<sup>85</sup> and by using the previously discussed Kane model account for the changes in  $m^*_D(p, T)$  and  $\varepsilon_g(T)$ . The results at various temperatures are shown in Figure 27, and show that even at 800K with an extrinsic hole carrier density  $\sim 10^{20} \text{ cm}^{-3}$  the density of thermally activated electrons is no greater than  $10^{16} \text{ cm}^{-3}$ , at 600K it is at least four orders of magnitude less than the optically excited carriers. This result contradicts previous reports of intrinsic conduction.<sup>58,24</sup>

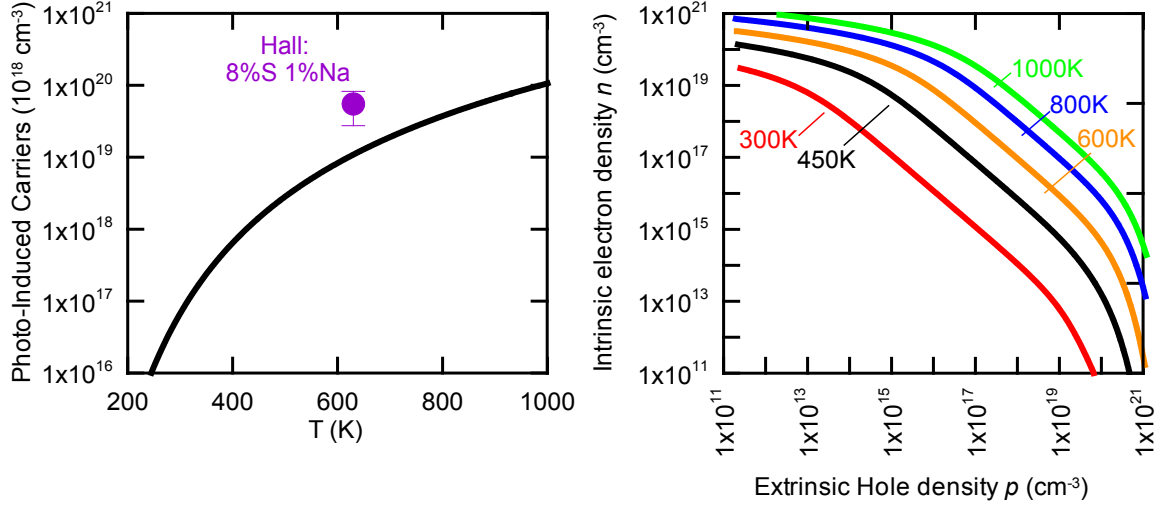


Figure 27: Calculated photo-excited electron density (Eq. 91) vs. temperature and calculated thermally excited electron density at various temperature as a function of hole carrier density.

We show the galvanomagnetic and thermomagnetic properties from 80-420K in Figure 28 on the samples with  $[\text{Na}]=0.01$ . There is a large temperature dependence of  $R_H$  for all samples with a plateau at low  $T$ , with a very similar trend to earlier reports.<sup>86</sup> At 80K, taking  $r_H=0.65$ ,<sup>60</sup>  $p = r_H/R_Hq = 1.4 \times 10^{20} \text{ cm}^{-3}$  for  $x=0.08$ , yielding a doping efficiency of nearly unity. This varies slightly for the other samples with different  $x$ . As  $p > 10^{20} \text{ cm}^{-3}$ , we conclude that  $\varepsilon_F$  for all samples is in the LVB at all  $T > \sim 100\text{K}$ , as can be seen from Fig 3a inset. The temperature dependence mirrors Ref. [87], with a low field slope that increases from 100K-460K, and then turns negative. This is in sharp contrast to the resonant PbTe-PbS:Tl alloys where  $R_H$  has a different temperature dependence (almost none at the measured  $T < 420\text{K}$ ) as previously shown in Figure 22. There is no systematic trend in the magnitude of  $R_H$ ; this most likely arises from unavoidable small variations in sample preparation due to the high reactivity of sodium and the anneal at 1100K that achieves single phase material. Crocker<sup>59</sup> experienced similar issues when annealing at

1073K. Due to the lack of a systematic trend in  $R_H$  between samples, it would be remiss to compare absolute values of  $\rho$  or  $\mu$  between the samples as  $\mu$  is a function of both  $x$  and  $p$ . We note that  $x=0$  & 0.04 have different temperature dependences than  $x=0.08$  & 0.12 at low  $T$ , with the former having a sharp drop in  $\rho$  at  $\sim 60$ K.

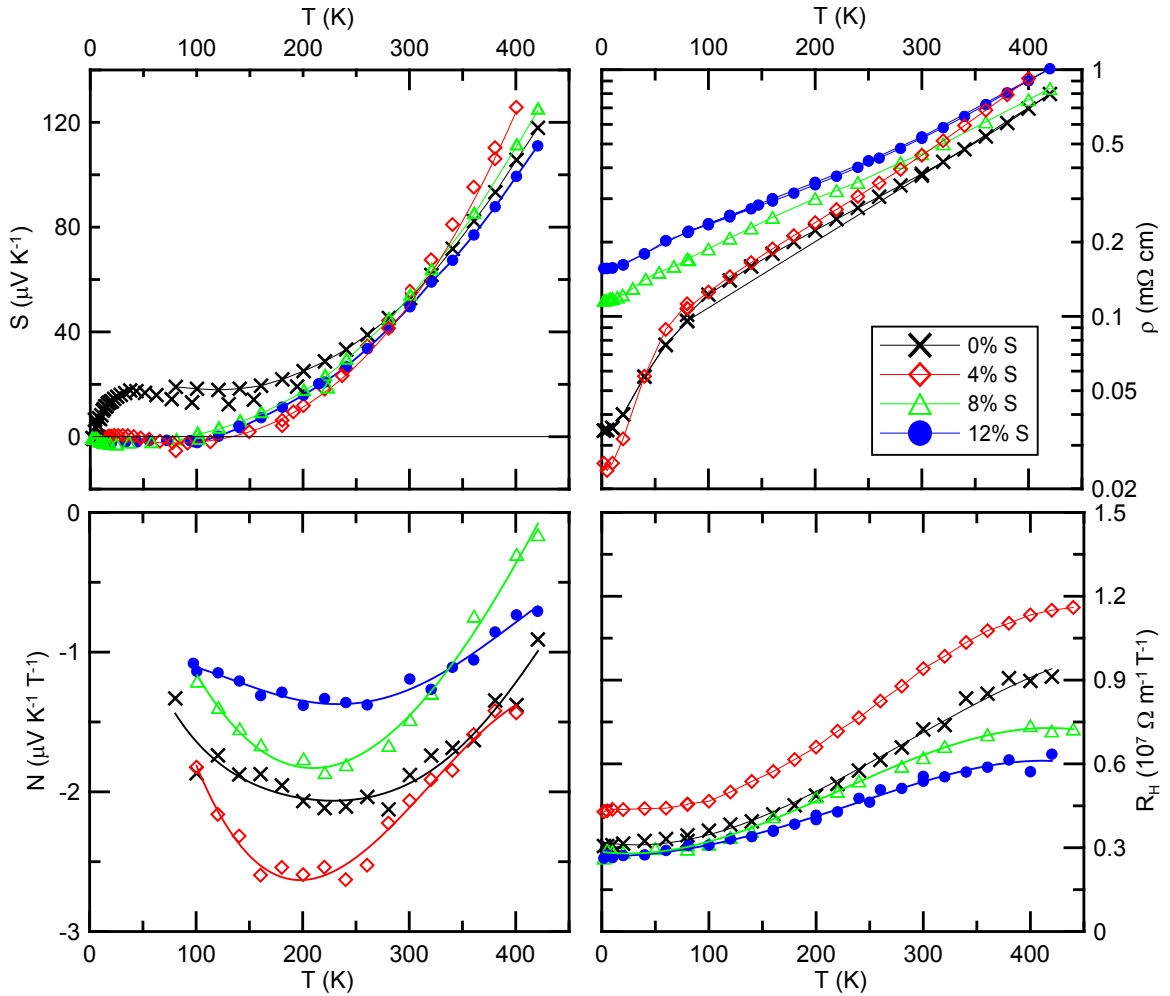


Figure 28: Low temperature electrical properties of 1% Na doped samples. a) Seebeck coefficient, b) Nernst coefficient, c) electrical resistivity, and d) Hall coefficient from 2-420 K. The symbols are experimental points; the lines are added to guide the eye.

Moving to  $\alpha$ , we note unique temperature dependence: the sign changes from positive to negative in samples with sulfur as  $T$  is lowered. This can occur if carriers of an opposite

sign appear; however,  $R_H(B)$  remains very linear and indicates that this is a heavily doped  $p$ -type semiconductor, and as such,  $\alpha$  should remain positive as  $T$  approaches 0K. An option is interband scattering as it has a negative scattering parameter and can thus force  $\alpha$  to the opposite sign of the dominant carrier. Geballe reports similar behavior in heavily doped Si, and attributes this to impurity band conduction.<sup>88</sup> As  $\varepsilon_F$  is in the LVB, all samples have very similar  $\alpha$  at 300K of 49-51  $\mu\text{V/K}$  similar to earlier reports<sup>57</sup>. The effects of optically induced conduction are also witnessed in higher temperature  $\alpha$ , which remains approximately constant at higher temperature (Figure 30). We will further address the low temperature regime of  $\alpha$  subsequently. Nernst coefficient is large for a heavily doped semiconductor, and negative.  $N$  with  $x>0$  monotonically decreases in magnitude, while the magnitude of  $x=0.04$  is larger than  $x=0$ . Rogers<sup>87</sup> also reports on  $N$  for a PbTe sample heavily doped with Na that has similar 77K  $R_H$  values as here; while the temperature dependence is very similar to ours the magnitude is slightly off, with Rogers'  $N$  roughly double. Rogers does not mention if he took the Righi-Leduc effect into account, which may explain this discrepancy.

I further investigate  $\alpha$  of the samples with  $x=0, 0.04,$  and  $0.12$  at lower temperature and in zero and high magnetic field and plot the results in Figure 29. A strong magnetic field measurement of thermopower is independent of scattering effects.  $\alpha$  of  $x=0$  is positive at all temperature, and has a phonon-drag peak, reaching 18  $\mu\text{V/K}$  at 40K in zero field before dropping to 12  $\mu\text{V/K}$  at 120K.  $\alpha$  of  $x=0.12$  changes sign at  $\sim 110\text{K}$  in zero field and at  $\sim 60\text{K}$  in 7T.  $x=0.04$  switches negative at  $\sim 135\text{K}$ , and with 3.5T and 7T external field  $\alpha$  remains positive at all temperature. Furthermore,  $x=0.04$  exhibits a phonon-drag effect in  $\alpha$ , which is clearly seen at  $T<30\text{K}$ . This increase is smaller than in  $x=0$ , as

expected due to the reduced  $\kappa$ . In zero field, this phonon-drag actually switches sign of  $\alpha$  again to positive at  $\sim 30\text{K}$ . As the effect of phonon-drag on thermopower will be greatest on the majority carrier, this is another indication that negative thermopower does not arise from electrons. Furthermore, the large phonon drag in  $x=0$  prevents the negative Seebeck; it is only in the presence of sulfur with the reduced thermal conductivity does the thermopower switch sign.

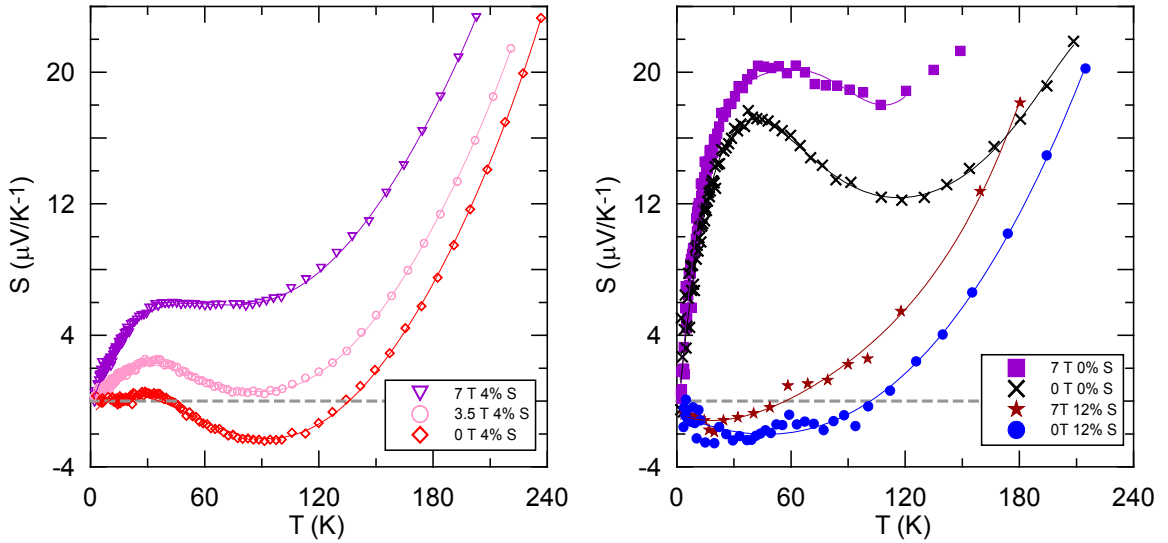


Figure 29: Seebeck coefficient from 2-240K for  $[\text{Na}]=0.01$ . The top plot depicts  $x=0$  &  $x=0.12$  in 0 & 7T field; the bottom contains  $x=0.04$  in 0, 3.5T & 7T field. The symbols are experimental points; the lines are added to guide the eye.

To ascertain if indeed the negative Seebeck is a scattering effect, we synthesize and measure low temperature  $\alpha$ ,  $N$ , and  $R_H$  of  $\text{Pb}_{1-y}\text{Na}_y\text{Te}_{0.92}\text{S}_{0.08}$  with  $y=0.01, 0.005, 0.0025$ . This is done to place  $\epsilon_F$  at different locations in the valence band, and thus change the relative importance of interband scattering between different samples, thus allowing a

contrast over temperature. Table 2 is a comparison of the [Na] and hole concentrations, with  $r_H$  taken from Ref [60]. We see that for  $y=0.01$  &  $0.005$ , the calculated  $p$  using literature  $r_H$  matches up quite well with [Na], whereas for  $y=0.0025$   $r_H=1$  appears more appropriate. The temperature where Nernst has a maximum decreases monotonically with increasing [Na]; this is expected as  $p$  increases the temperature at which the optimal  $p_{UVB}/p_{LVB}$  to maximize interband scattering decreases. As a consequence (Figure 29),  $\alpha$  of  $y=0.005$  is negative in a temperature range that is higher than  $y=0.01$ .  $\alpha$  for  $y=0.0025$  does not go negative as  $\epsilon_F$  does not reach the LVB until high temperature and thus interband scattering is reduced. Again,  $\alpha$  in 7T field for the  $y=0.005$  is positive at all temperatures, the temperature for  $y=0.01$  is reduced to  $\sim 20$ K.

Due to the two carrier nature of this system, we can only use the method of the 4 coefficients on  $y=0.0025$  and only at low  $T$ . The fits indicate that the scattering parameter ( $\lambda$ ) increases monotonically with  $T$ , is negative at 80K ( $\lambda \sim -0.6$ ) from interband scattering, and is positive above 200K; mostly acoustic phonon scattering with some optical phonon contribution. This theoretically confirms the magnetic field measurements and explains the  $T^2$  relation of  $\alpha$ : one  $T^l$  is a result of the  $T$  in Mott relation and the second  $T^l$  stems from the increasing  $\lambda$ , which factors into the Mott relation. Furthermore,  $\epsilon_F(80\text{K}) = 83$  meV and  $m_D^* = 0.22 m_e$ , both in close accordance with the reported values for the UVB<sup>48</sup> and the measured hole density.

Table 2. Comparison between nominal sodium composition and measured Hall coefficients in  $\text{Pb}_{1-y}\text{Na}_y\text{Te}_{0.92}\text{S}_{0.08}$ .

| Nominal Na | [Na]                      | $R_H$                        | $p=1/R_{Hq}$              | $r_H$<br>(Ref.87) | $p=r_H/R_{Hq}$            | $R_H(300)/R_H(80)$ |
|------------|---------------------------|------------------------------|---------------------------|-------------------|---------------------------|--------------------|
|            | $10^{19} \text{ cm}^{-3}$ | $10^7 \Omega\text{m T}^{-1}$ | $10^{19} \text{ cm}^{-3}$ |                   | $10^{19} \text{ cm}^{-3}$ |                    |
| 0.25%      | 3.72                      | 1.96                         | 3.19                      | 1.4               | 4.1                       | 1.7                |
| 0.50%      | 7.44                      | 0.52                         | 12.0                      | 0.65              | 7.8                       | 2.3                |
| 1.00%      | 14.88                     | 0.29                         | 21.5                      | 0.65              | 14                        | 2.1                |

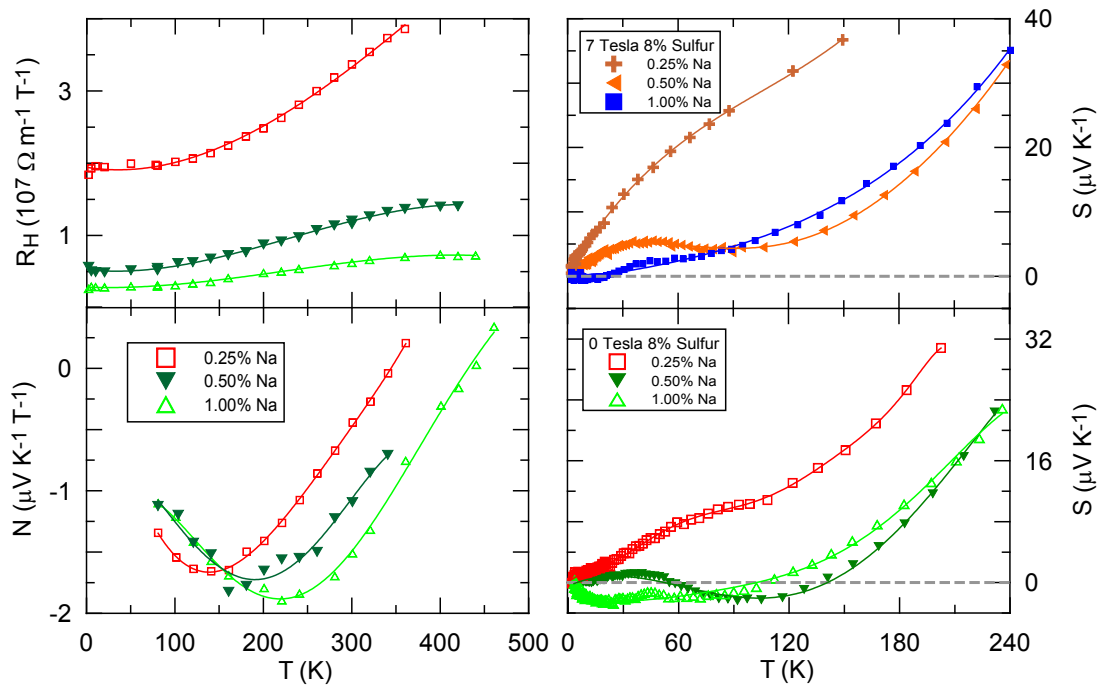


Figure 29: Low temperature electrical properties of 8% S samples with different dopant concentrations. a) Hall coefficient b) Nernst coefficient c) and d) Seebeck coefficient in 0, 7T external field for 8% S and various [Na]. The symbols are experimental points; the lines are added to guide the eye.

Measurements on  $x=0.08$  &  $0.12$  up to  $800\text{K}$  of  $\alpha$ ,  $\rho$ ,  $\kappa$ , and  $zT$  are shown in Figure 30.

The two samples have similar Seebeck coefficients, which are linear with respect to temperature, peak at  $\sim 280\mu\text{V/K}$  at  $650\text{K}$  and then remain flat. We attribute this to the

appearance of optically excited electrons, which is also witnessed in  $\rho$  and directly reflected in Hall coefficient. Airapetyants<sup>57</sup> saw very similar behavior in his high temperature thermopower.  $\rho$  remains low, and peaks at  $\sim 4.5$  m $\Omega$ -cm for  $x=0.12$ . Thermal conductivity shows a monotonic decrease with increasing sulfur content, as expected. This decrease stems from the reduction in lattice thermal conductivity, as the samples have similar  $\rho$ .  $zT$  reaches a value of  $\sim 1.55$  at 700K and remains above 1 at  $T > 500$ K. These values are, within errors, very similar to previous reports on PbTe alloys.<sup>36,38,39</sup>

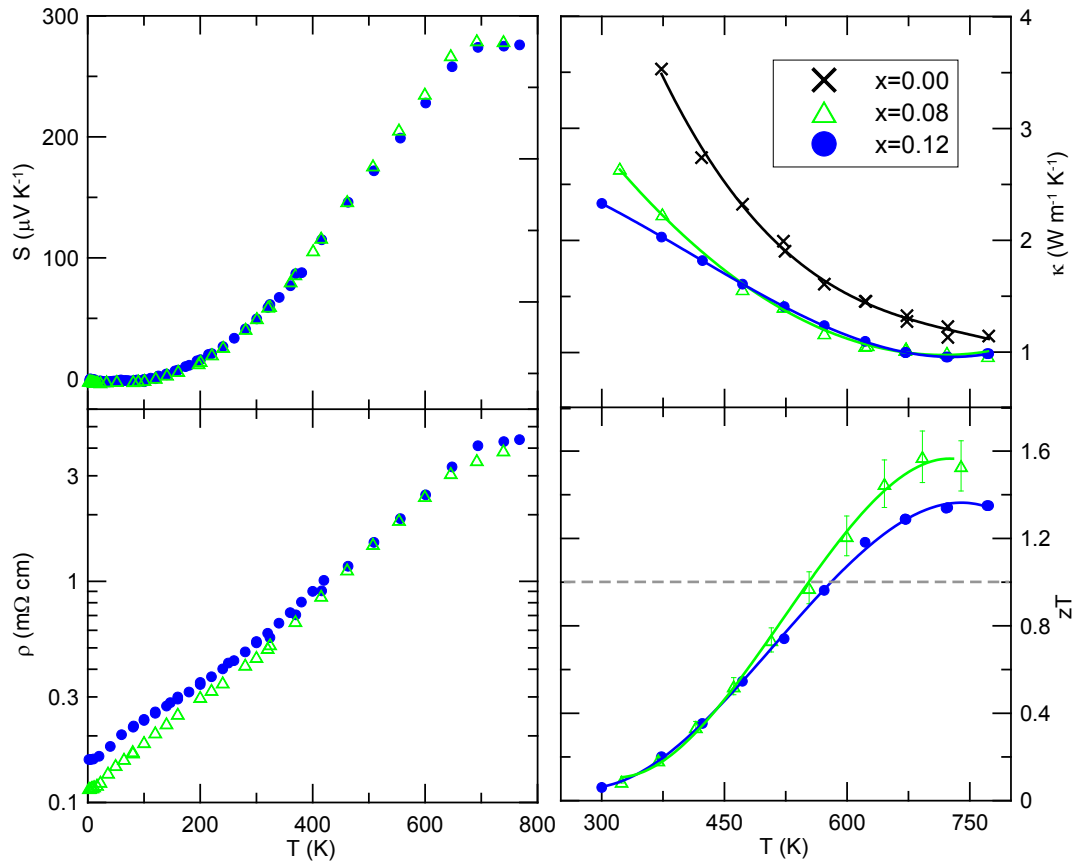


Figure 30: Seebeck coefficient, electrical resistivity, thermal conductivity and  $zT$  for samples with  $[\text{Na}] = 0.01$ . The symbols are experimental points; the lines are added to guide the eye.

In conclusion, we have demonstrated that the band crossing at  $\sim 420\text{K}$  is improbable and the temperature dependence posited by Allgaier and Houston<sup>63</sup> is more likely: the LVB and UVB cross at or above  $800\text{K}$ . This does not mean that the LVB doesn't contribute to transport; clearly with thermal smearing and appropriate chemical doping a portion of the holes populate the LVB. The low temperature thermopower clearly shows the interaction between holes in the LVB and UVB when  $\varepsilon_F$  is placed in the LVB.  $zT$  reaches  $\sim 1.55$  at  $700\text{K}$  and thus we have reached similar material efficiencies without the usage of Tl in PbTe alloys and have reduced the amount of Te necessary to make an efficient thermoelectric module. Here, we show new data (Figure 26) that illustrate that at  $T > 500\text{K}$  the measurements of  $R_H$  must be made as a function of magnetic field, not only using two fixed fields of opposing polarity, because that procedure may mask the existence of photo excited electrons, and creates a large error in the carrier concentration numbers thus rendering band structure vs.  $T$  incorrect.

## Chapter 5: Spin-Seebeck Effect in Semiconductors

In this section we detail the measurements that we have performed of the spin-Seebeck effect in GaMnAs and InSb. The section is split up to have the initial observations and establishment of the effect GaMnAs first, followed by further analysis of how temperature, substrate condition and electrical communication affects the spin-Seebeck effect. We follow with measurements in a new class of material: nonmagnetic InSb.

The spin-Seebeck effect was first reported as an electrical measurement of a redistribution of spins along a millimeter long thin film of a ferromagnetic metal (NiFe) induced by a  $\nabla T$ .<sup>1</sup> This was quite unexpected, as the length scales involved in the distribution of spins are orders of magnitude longer than the spin diffusion length. We then began my study of the spin-Seebeck effect on thin films of a ferromagnetic semiconductor (GaMnAs). Simultaneously, Uchida was studying a ferromagnetic insulator, (yttrium iron garnet, YIG).<sup>4</sup> Coincidentally, we published our results at the same time in the same journal.<sup>3</sup>

### Gallium Manganese Arsenide

#### Material Background

GaAs is a semiconductor with a direct band gap of 1.4 eV at 300K. It crystallizes in the zinc blend in  $F43m$  group. When doped with Mn, at high enough concentration, the material becomes a ferromagnet, and the Curie temperature thus far is always below room temperature, the highest reported is 173K.<sup>89</sup>  $T_c$  scales with hole density. Thus far,

GaMnAs is grown via low temperature molecular beam epitaxy (MBE). Mn incorporates into the lattice in two ways interstitial and substitutional for Ga. The substitutional Mn acts as an acceptor, however the interstitial is a donor and thus compensates the holes.  $T_c$  can be raised by annealing at a proper temperature, thus it is thought that this anneal drives the interstitial Mn out of the lattice to the surface.

The magnetism is hole mediated – the Mn atom enters the lattice as  $Mn^{2+}$  with a spin quantum number of  $S=+5/2$  and no orbital moment ( $L=0$ ). The hole in the GaAs valence band that is locally attracted to this Mn atom is antiferromagnetically coupled. The hole then aligns any Mn atoms within the extent of its wave antiparallel to its spin, and these Mn atoms are then locally ferromagnetically aligned. Their corresponding holes then spatially extend the magnetic orientation. As the holes propagate throughout the materials, any Mn atoms visited by the holes align ferromagnetically. Increasing the hole density to sufficiently high levels creates a long-range ferromagnetic ordering.  $T_c$  is thus related to a prefactor multiplied by the hole density raised to power 1/3:  $T_c \sim p^{1/3}$ .

GaMnAs allows for increased flexibility in its magnetization direction, with easy and hard axes aligned along crystallographic directions  $[1\bar{1}0]$  and  $[110]$ , respectively. These are also cleavage planes. A third magnetic easy axis lies along  $[100]$ , or  $45^\circ$  off the cleavage planes. Furthermore, it is possible to force magnetization axis out of plane  $[001]$  by growing on relaxed InGaAs on GaAs substrate. This allows for observation of the conventional Nernst effect.

An in-plane temperature gradient ( $\nabla_x T$ ) was applied to the sample as depicted in Figure 31. The geometry of NiFe and YIG experiments are the same as here. The sample

magnetization ( $\mathbf{M}$ ) and therefore the spin polarization vector ( $\boldsymbol{\sigma}$ ) can be controlled using an applied magnetic field ( $\mathbf{B}$ ). Pt bars are deposited on the sample, which serve as local spin current detectors: when subjected to  $\nabla_x T$ , a flux of spins ( $\mathbf{J}_S$ ) diffuse along the  $z$  direction into the strips generating an ISHE voltage,  $\frac{V_y}{W} \hat{\mathbf{E}}_{\text{ishe}} = \mathbf{E}_{\text{ishe}} = D_{\text{ishe}} (\mathbf{J}_S \times \boldsymbol{\sigma})$ , where  $D_{\text{ishe}}$  is the ISHE coefficient of platinum and  $W$  is the strip width.

I now summarize the highlights of my measurements of the spin-Seebeck effect in GaMnAs, and subsequently will detail the experimental results, control tests, and the theoretical understanding that our group has developed. First, the electric field in the Pt strips  $E_{\text{ISHE}}$  is antiparallel on hot/cold ends of the sample, mirroring the NiFe work. This electric field tracks and switches sign with magnetization of the sample, thus it has an odd dependence. The positional dependence of the sample is fitted accurately with a  $\sinh(x)$  function, which is cognizant of the temperature difference between magnons and phonons.<sup>94</sup> The reversal in  $E_{\text{ISHE}}$  at the coercive field is not observed above the Curie temperature of the GaMnAs. There is a peak in spin-Seebeck coefficient at a temperature close to the peak in substrate thermal conductivity, near the temperature where phonon-magnon drag effects are maximal; below this temperature the number of phonons decreases, above this temperature increased phonon-phonon scattering begins to dominate. The effect is maintained without electrical communication between ends of the sample. Finally, on samples with magnetic axis out of plane, the spin-Seebeck effect is not present due to collinear spin flux and spin orientation leading to a zero cross product.

## Temperature and Positional Dependence

Magnetometry on SQUID indicates that  $[1\bar{1}0]$  and  $[100]$  are easy axes and  $[110]$  is a uniaxial hard axis. This is shown in Figure 31c-d and a schematic of the fluxes and crystallographic directions is included in panel b; panel a depicts the sample geometry, as discussed in the Methods section. Figure 31e shows  $V_y$  measured on two platinum bars (hot and cold end) while sweeping  $B_x$  in a hysteretic fashion along  $[1\bar{1}0]$  magnetic easy axis. As the charge carrier spins (holes) are exchange coupled to the local Mn magnetic moments ( $\sigma // \mathbf{M}$ ) any transverse spin Hall voltage ( $V_y$ ) due to a local spin current along the  $z$ -axis ( $\mathbf{J}_S // z$ ) switches sign as the magnetization switches with applied field. The magnitude of the switch is  $\Delta V_y$ , and is actually twice the voltage generated by ISHE, as  $\mathbf{M}$  reverses direction; this is corrected in the definition of the spin-Seebeck coefficient. The sign of  $\Delta V_y$  switches between the hot and cold sides, revealing a spatial dependence to the sign and magnitude of  $\mathbf{J}_S$ . This spatial dependence distinguishes the spin-Seebeck effect from all other known thermomagnetic transport phenomena. Thermopower does not show any steps at the coercive field. When  $x // [110]$ , the magnetic hard axis, a sharp switching of  $V_y$  is observed at small field following the magnetization switching along the  $[100]$  easy axis (Figure 31d), which lies  $45^\circ$  off of the applied field. As the magnetic field is further increased,  $V_y$  shows an opposite field dependence similar to the hard axis magnetization saturation.

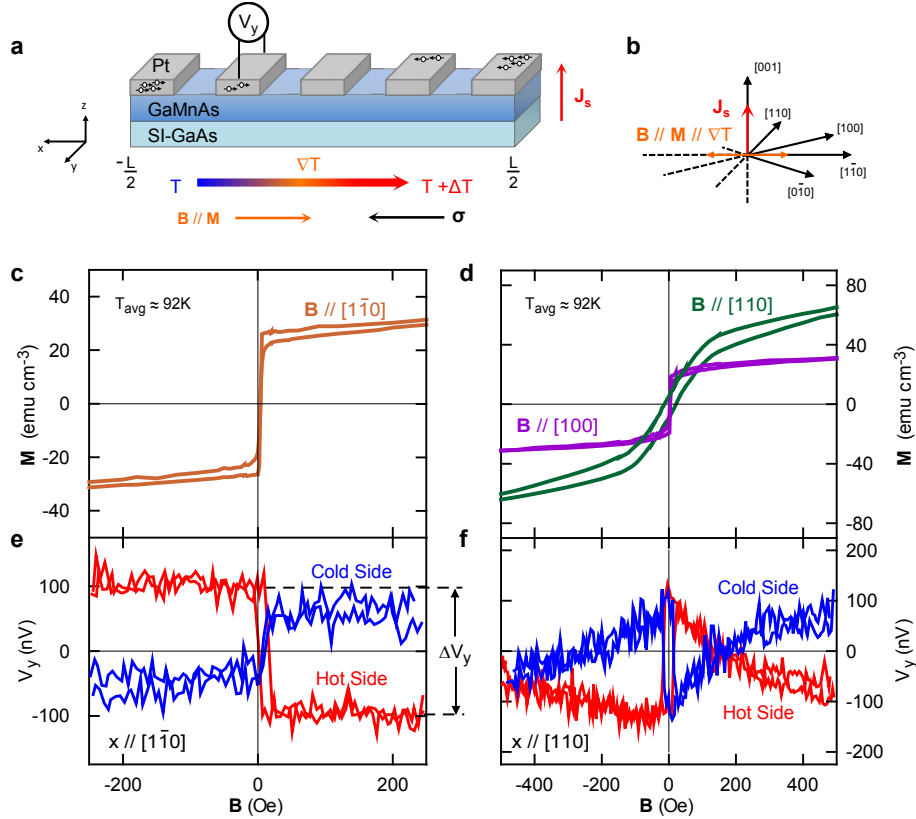


Figure 31: Measurement schematic and raw voltage traces in two different crystallographic directions. **a**, Measurement geometry (not to scale). **b**, Crystal directions in GaMnAs. **c** and **d**, Magnetization,  $\mathbf{M}$ , as a function of applied magnetic field,  $\mathbf{B}$  oriented along the easy  $[1\bar{1}0]$ ,  $[100]$ , and hard  $[110]$  axes. **e** and **f**, Transverse voltage,  $V_y$  as a function of  $\mathbf{B}$ , along the easy  $[1\bar{1}0]$  and hard  $[110]$  axes with an applied  $\Delta T_x$  of 1.77 K and 3.13 K, respectively. Data are shown on strips near the hot and cold ends of the sample.

The change in transverse voltage,  $\Delta V_y$  as defined in Figure 31e, is measured at nine positions along the sample ( $L=12.6$  mm) with  $x // [1\bar{1}0]$  and plotted in Figure 32 revealing a linear dependence on the applied thermal gradient,  $\Delta T_x$ . These data were taken at 53K. From the slope of the line we initially obtain the spin-Seebeck signal

$(\Delta V_y/2) / \Delta T_x$ . In order to express it as a function of the fluxes, we define the spin-Seebeck coefficient as:

$$S_{xy} \equiv \frac{E_y}{\nabla_x T} = \frac{L\Delta V_y}{2w\Delta T_x} \quad (92)$$

$S_{xy}$  has the same units as thermoelectric power.  $L$  is the distance between the thermometers, and  $w$  is the width of the sample.

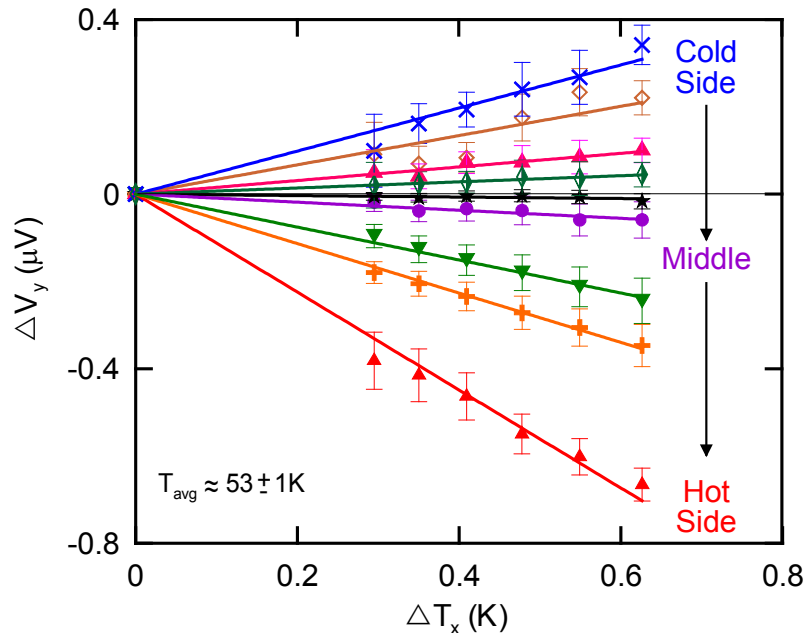


Figure 32:  $\Delta V_y$  vs  $\Delta T_x$  shows linear behavior at 6 different  $\Delta T$  values on all nine strips, and  $\Delta V_y=0$  at zero gradient.

Figure 33 plots the temperature and spatial variation of  $S_{xy}$  determined by measuring  $V_y$  versus  $B_x$  and  $\Delta T_x$  at various temperatures on the nine contacts across the sample. The spin-Seebeck coefficient tracks a  $\sinh(x)$  function, though the data points have a slight offset from the mid-point ( $x = 0$ ) of the sample (not perfect symmetry). Normalizing by

the maximum value of  $S_{xy}$  reveals that the spatial distribution has nearly the same form at the temperatures studied. This spatial dependence is in contrast to  $\alpha_{xyz}$  (or Nernst coefficient), which is independent of  $x$ , and follows the relation:

$$S_{xy}(L) = A \sinh\left(\frac{x}{L} - b\right) \quad (93)$$

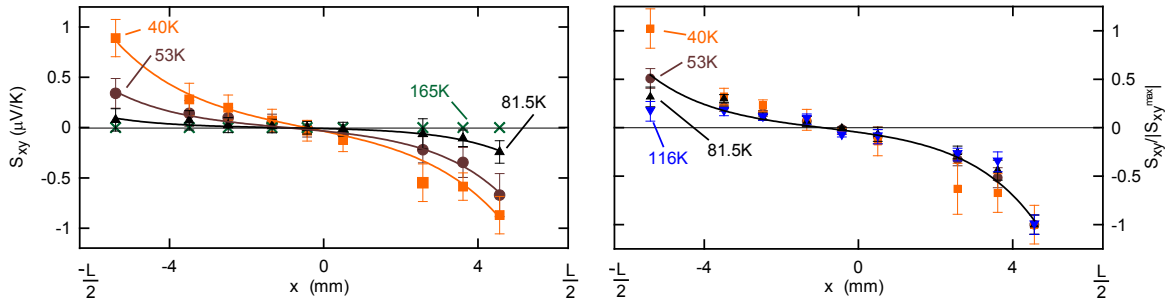


Figure 33: a) Positional dependence of  $S_{xy}$  at various temperatures.  $S_{xy}$  varies via a  $\sinh(x-L/2)$  around the midpoint of the sample. b) Normalized  $S_{xy}$  at various temperatures.  $S_{xy}$  at each strip has been divided by the maximum  $S_{xy}$  at each respective temperature.

Table 3 Fitting parameters for experimental data in Figure 33 to Eq. 93.

| Sample Temperature | L    | A     | b     |
|--------------------|------|-------|-------|
| 81.5K              | 1.53 | -0.01 | -0.72 |
| 53K                | 1.81 | -0.06 | -0.52 |
| 40K                | 2.09 | -0.16 | -0.21 |

The temperature dependence of  $S_{xy}$  shown in Figure 34 reveal that  $S_{xy}$  disappears above  $T_C$ , but otherwise its temperature-dependence is quite different from that of the magnetization as well as that of  $\alpha_{xx}$ . Thermopower follows that of a degenerate semiconductor at higher temperatures ( $>100\text{K}$ ), with the onset of phonon-electron drag at lower temperatures resulting in a broad hump in  $\alpha$ . The measurements of spin-Seebeck

effect on Pt strips repeat on a second sample (different Mn concentration) as shown in Figure 35.  $\nabla T_x$  is along  $[1\bar{1}0]$  (stoichiometric direction) and  $V_y$  is measured along  $[110]$ . Strip 1 is the hottest, and strips 2 and 3 are mirrored around the center, with the temperature of strip 3 the coldest. Figure 35c shows the raw voltage traces at each contact for differing  $\Delta T_x$  values with an average sample temperature of 98K. Figure 35b plots  $\Delta V_y$  vs.  $\Delta T_x$  for the data in Figure 35c and repeats the linear behavior.,  $\Delta V_y$  vs.  $\Delta T_x$  traces at other average sample temperatures also have the linear behavior and pass through the origin and are not shown.  $S_{xy}$  as a function of temperature is shown to be zero above  $T_c$ , and increases in magnitude with decreasing temperature. All features (temperature and positional dependence) of the spin-Seebeck coefficients repeat on this sample.

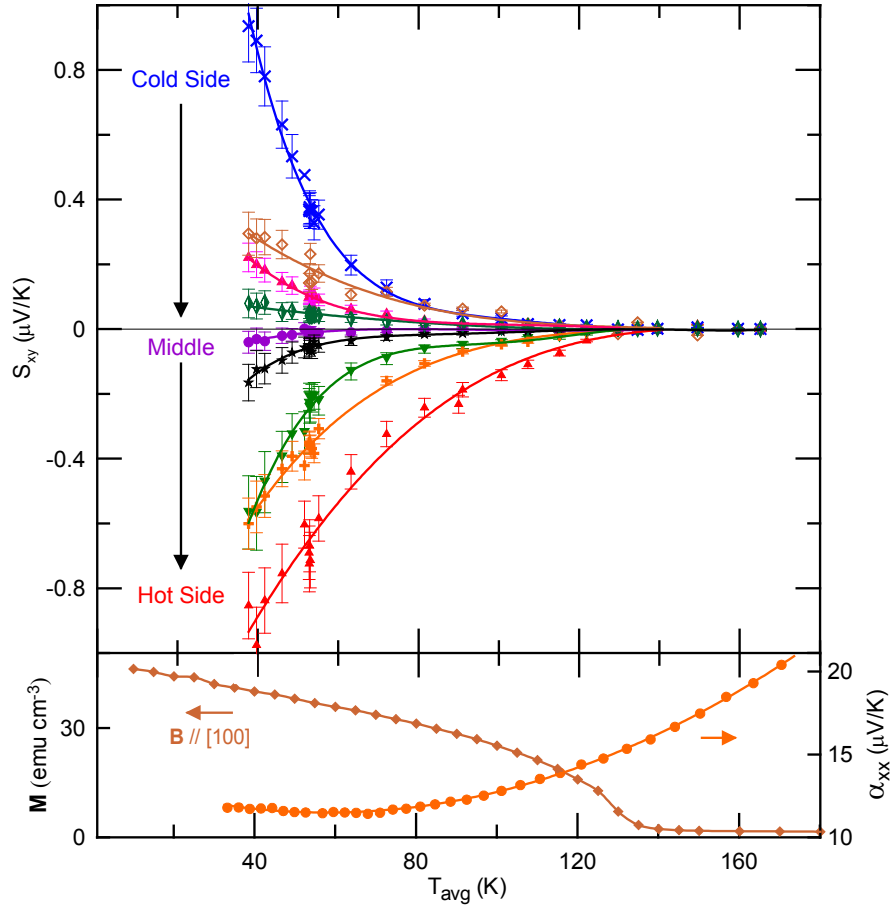


Figure 34: a) Temperature dependence of various Pt strips across the GaMnAs sample.  
 b) Magnetization showing ferromagnetic behavior and thermopower  $\alpha_{xx}$ .

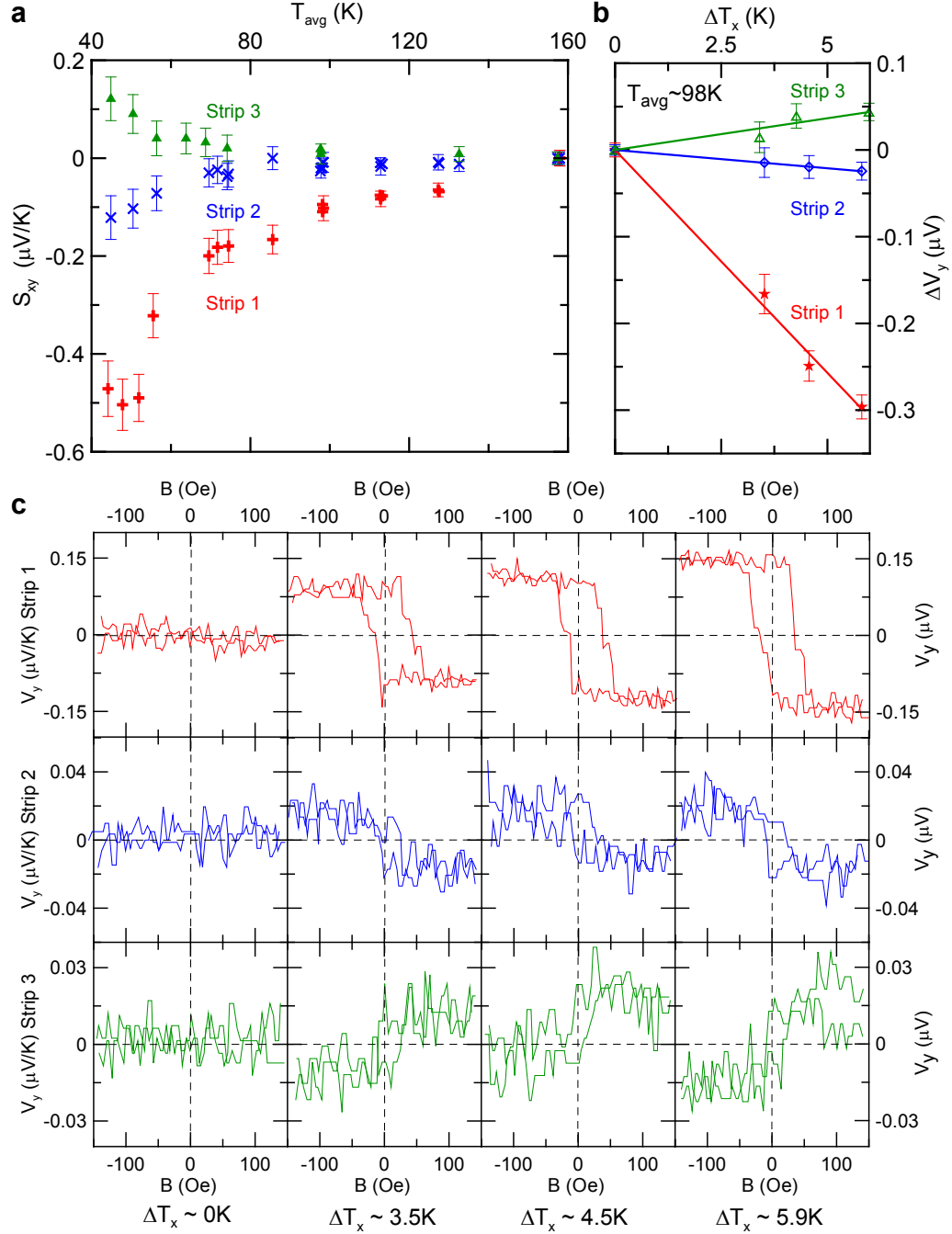


Figure 35: Repeat of spin-Seebeck effect in a 2<sup>nd</sup> GaMnAs sample. Data was measured on a thin film GaMnAs sample on a GaAs wafer with in-plane magnetization and  $s=0.16$ . **a**,  $S_{xy}$  as a function of temperature for three Pt strips. Strip 1 is at the hot end, strips 2 and 3 are centered around the midpoint of the sample. **b**,  $\Delta T_x$  vs.  $\Delta V_y$  at  $T \sim 98\text{K}$  **c**, Raw traces with background voltages subtracted.

### Scratch Test

We directly test for a macroscopic spin/charge current along  $x$  by polishing away 0.35-mm wide regions of GaMnAs with sandpaper, thereby severing electrical contact (the 2-point resistance between strip contacts increased from  $500 \Omega$  to over  $3 \text{ M}\Omega$ ). If  $S_{xy}$  were induced by a longitudinal spin current ( $J_S // x$ ) or macroscopic spin flux accompanying a flux of the charge carriers, then scratching the sample in half would result in two independent samples, creating a  $V_y > 0$  above the scratch and  $V_y < 0$  immediately below the scratch. We would then expect hysteresis loops of  $V_y$  versus  $B_x$  exhibiting steps,  $\Delta V_y$ , with different sign above and below the scratch. Figure 36a shows hysteresis loops from a strip contact before and after a scratch, exhibiting no qualitative change. This contact is approximately 0.3-mm distant from the scratch. The spatial dependence of  $S_{xy}$  is plotted in Figure 36b revealing no qualitative change in signal resulting from the scratch. More importantly, the two inner contacts within 0.3 mm of the scratch exhibit no change. The temperature dependence of  $S_{xy}$  at each contact, comparing Figure 34c with Figure 36c, is unaffected by the scratch. This demonstrates that the spin-Seebeck signal in GaMnAs does not result from a macroscopic, longitudinal spin-current  $J_{Sx}$ . We suggest that it originates from a perturbation of the statistical distribution function of the spin-polarized charge carriers induced by the temperature gradient. Since charge/spin carriers cannot cross the scratch, the macroscopic spatial distribution of  $S_{xy}$  (Figure 36) can only be explained by an interaction insensitive to the scratch, for instance thermal coupling through the substrate in which the heat is carried by phonons.

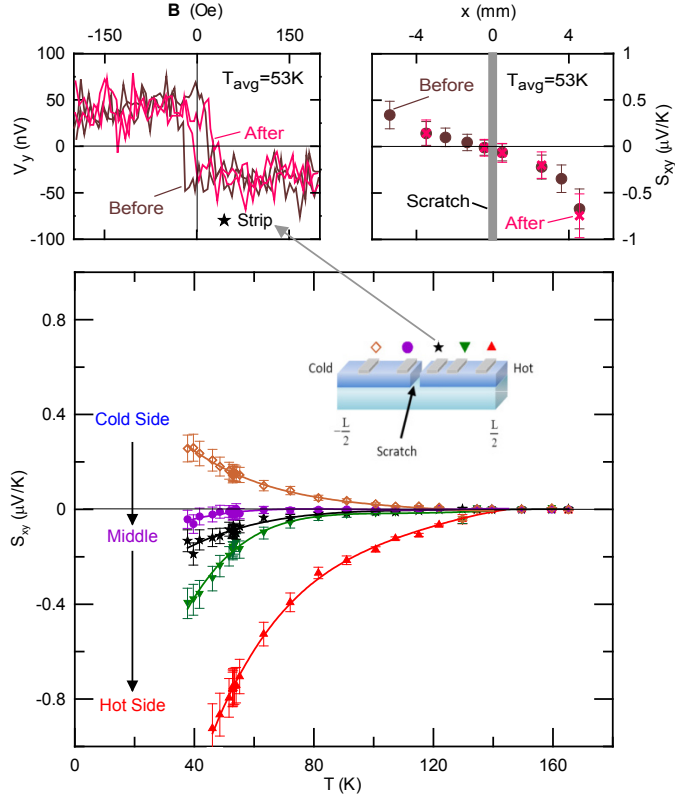


Figure 36: Severance of electrical communication: the scratch test.

We repeat the test for a macroscopic spin/charge current along  $y$  by first shortening a different sample with  $s=0.158$  about 15% and then polishing away a 0.35-mm wide region of GaMnAs with sandpaper in the middle of the sample, Figure 37(Case 2). After repeating the measurement, a second scratch of equal width is added just below the hot side Pt strip (Case 3). Figure 37b shows hysteresis loops from the hot-side contact before and after each scratch, exhibiting no quantitative change. The temperature dependence of  $S_{xy}$ , is likewise unaffected by the presence of scratches, Figure 37c. Further,  $S_{xy}$  at the top edge of the sample shows no dependence on the overall length of the sample, confirming our normalization procedure. Obviously, changing the length of sample will change the

midpoint of the sample, and thus affect the  $\Delta V_y$  in these regions. This repeats the results shown in Figure 34 on a different GaMnAs sample confirming that the spin-Seebeck effect does not depend on longitudinal electrical communication.

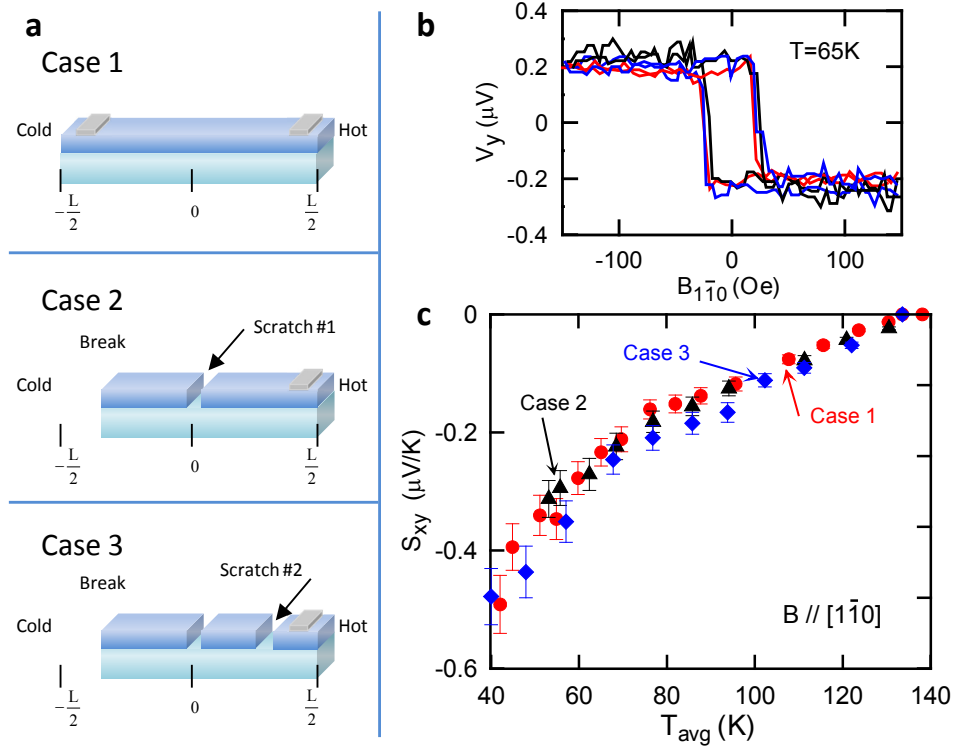


Figure 37: Repeat of scratch test and the spin-Seebeck effect's dependence on temperature gradient. **a**, Schematic for Case 1 (intact sample), Case 2 (sample was shortened 15% and a strip of GaMnAs was scratched away from the center of the sample), Case 3 (a second scratch was added). **b**,  $V_y$  was recorded during hysteresis loops from the hot-side contact before and after each scratch.  $V_y$  was normalized by the temperature gradient, which changed in each case. **c**, Spin-Seebeck coefficient.

### Point Contacts: Nernst Effect

Lastly, we repeat the spin-Seebeck measurements with  $\mathbf{M}$  oriented in-plane, but instead of platinum strip contacts, we use point contacts. Unlike the strip contacts, which short out any transverse voltages in GaMnAs, point contacts directly sample the electric field

within GaMnAs. Thus,  $V_y$  voltages induced by other thermomagnetic transport effects, like the planar Nernst effect  $\alpha_{xy}$ , are also expected to be included. Raw voltage traces (Figure 38a) reveal an  $x$  dependence similar to the strip contact measurements on the same sample (Fig. 1 & 2), though without a change in sign between the hot and cold ends.  $\Delta V_y$  is linear in  $\Delta T_x$  within the experimental error bars (Figure 38b). All this suggests that the signal contains contributions of both the  $x$ -dependent  $S_{xy}$  spin-Seebeck and the  $x$ -independent  $\alpha_{xy}$  planar Nernst effects. Because this signal is a mixture of  $S_{xy}$  and  $\alpha_{xy}$ , we label it  $S\alpha_{xy}$ , and measure and normalize it in the same manner as  $S_{xy}$ , previously described. The  $T$  dependence of  $S\alpha_{xy}$  measured for various contacts (Figure 38c) demonstrates that  $S\alpha_{xy}$  goes to zero above  $T_C$ , but exhibits an intermediate behavior between the temperature dependence of the  $S_{xy}$  on the strip contacts (Figure 38c) and that of  $\alpha_{xy}$ , which follows the magnetization [11]. This  $S\alpha_{xy}$  also reproduces the results of the scratch test performed on the strip contacts. We attempt to separate the spatially independent component of this mixed signal by averaging  $S\alpha_{xy}$  across the sample, which should be proportional to  $\alpha_{xy}$  (magenta circles panel d). Subtracting this average value reveals the spatially dependent component arising from  $S_{xy}$ , plotted as a function of temperature at different positions along the sample.

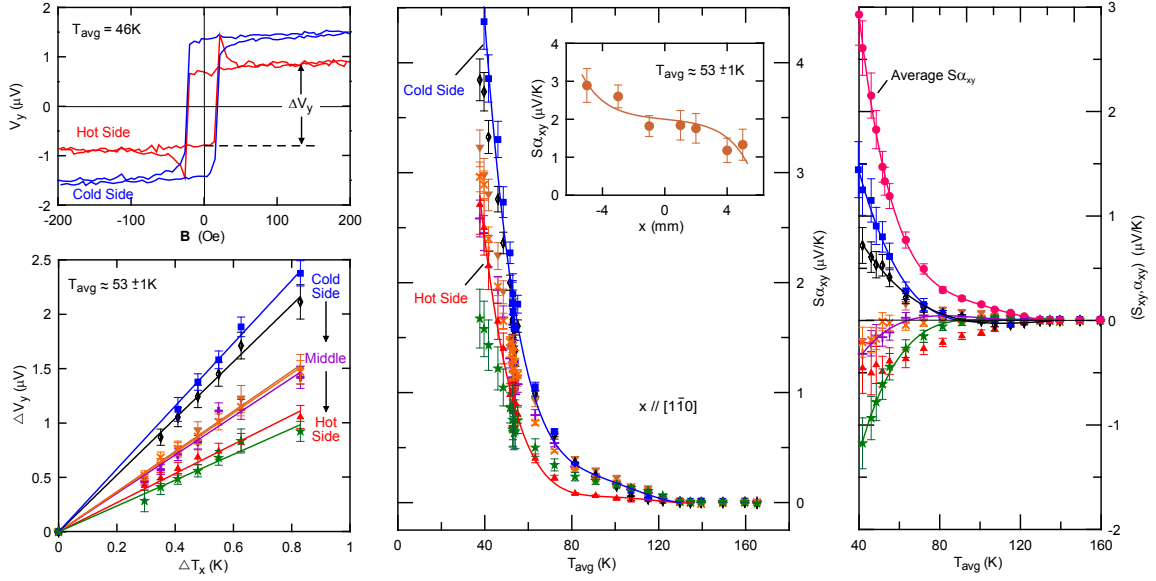


Figure 38: Spin-Seebeck in GaMnAs mixed with planar/anomalous Nernst effect. Point contacts were used as shown in the schematic (not to scale) with  $x \parallel [1\bar{1}0]$ . **a**, Transverse voltage,  $V_y$  as a function of applied magnetic field,  $\mathbf{B}$  at the hot and cold ends of the sample with an applied  $\Delta T_x$  of 0.67 K. **b**, The change in transverse voltage,  $\Delta V_y$  as a function of the applied thermal gradient,  $\Delta T_x$ , for strips along the length of sample. **c**,  $S\alpha_{xy}$  as a function of the sample temperature for differently positioned contacts. Inset plots the spatial dependence of  $S\alpha_{xy}$  at a selected temperature.

In the absence of strip contacts, which act as spin-current sensors, detection of a spin-Seebeck signal is unexpected. It may arise from GaMnAs acting as its own spin-current transducer. The  $V_y$  values observed in point contacts are experimentally independent from those in the strip contacts because in the absence of ISHE strip contacts simply act as electrical shorts to any  $V_y$  in the sample.  $V_y$  measured in strip contacts with M oriented in-plane therefore originate solely from ISHE in the platinum strips. Similarly, the spin-Seebeck component of the signal in point contacts could be due to a self-ISHE occurring in GaMnAs. We note that a similar  $V_y$  was also observed in  $\text{Ni}_{81}\text{Fe}_{19}$

with point contacts,<sup>90</sup> though of much smaller magnitude than in platinum strips. Here we observe  $S_{xy}$  of similar magnitude in strip and point contacts; this may be possible as GaMnAs has a much higher fraction of spin polarized carriers (>85%) than NiFe (~35%).

As a control test and to further ascertain the origin of the spin-Seebeck signal, we measure a GaMnAs sample with  $s=0.056$  and  $x \parallel [110]$  that has magnetic easy axis out-of-plane, along  $[001]$ . In this geometry, we expect no inverse spin Hall voltage in the platinum strip contacts because  $\mathbf{J}_s \parallel \boldsymbol{\sigma}$ , however the GaMnAs film is now expected to develop a transverse electric field,  $E_y$ , due to the transverse Nernst-Ettingshausen effect, which is proportional to the temperature gradient and to the out-of-plane magnetization. In contrast to the spin-Seebeck signal, the Nernst voltage exhibits no spatial dependence. To measure it, we place point contacts using silver epoxy along the length of this sample and tilt it  $6^\circ$  off of the  $xy$ -plane, thereby allowing the applied field  $\mathbf{B}$  to flip  $M_z$  Figure 39. The out-of-plane moment  $M_z$  is obtained by growing stressed GaMnAs on relaxed InGaAs, exhibiting easy axis behavior along  $[001]$ . As expected, the point contacts show a transverse Nernst signal, shown in Figure 39 with  $\mathbf{B}$  multiplied by  $\sin(6^\circ)$  to obtain  $B_{001}$ . Importantly,  $\Delta V_y$  does not exhibit a difference between the hot and cold ends of the sample. Platinum strip contacts show no signal (green and orange data) proving that (i) as expected, there is no spin-Hall effect when  $\mathbf{J}_s \times \boldsymbol{\sigma} = 0$ , and (ii) the strip contacts short out  $V_y$  generated by the Nernst effect in the GaMnAs layer. We detail in Figure 40 the temperature dependence of the Nernst-Ettingshausen effect defined as  $\alpha_{xyz} = \frac{E_y/B_z}{\nabla_x T}$  and a

schematic is shown in the inset of Figure 40. Again this signal goes to zero above  $T_C$  as  $M_z = 0$ , and increases in magnitude as the temperature is lowered.

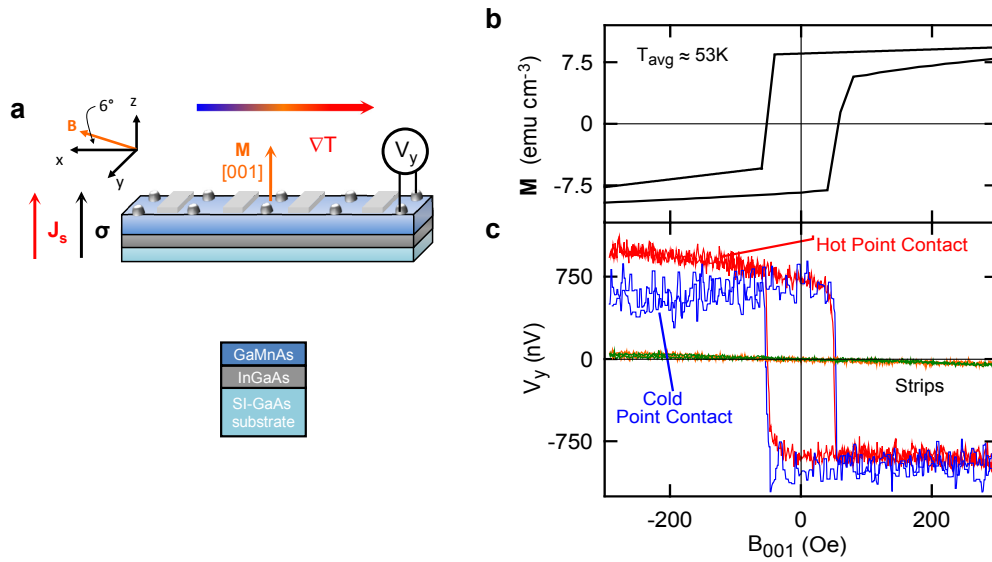


Figure 39: Measurements with out-of-plane magnetization. a, Sample layout (not to scale). Strained GaMnAs on InGaAs results in an out-of-plane magnetic easy axis [001]. b, Out-of-plane magnetization,  $M$  as a function of magnetic field,  $B$ . c, Transverse voltage,  $V_y$  versus  $B_{001}$  measured on point contacts (the transverse Nernst-Ettingshausen effect) and on strip contacts with  $B$   $6^\circ$  tilted from the  $xy$ -plane.

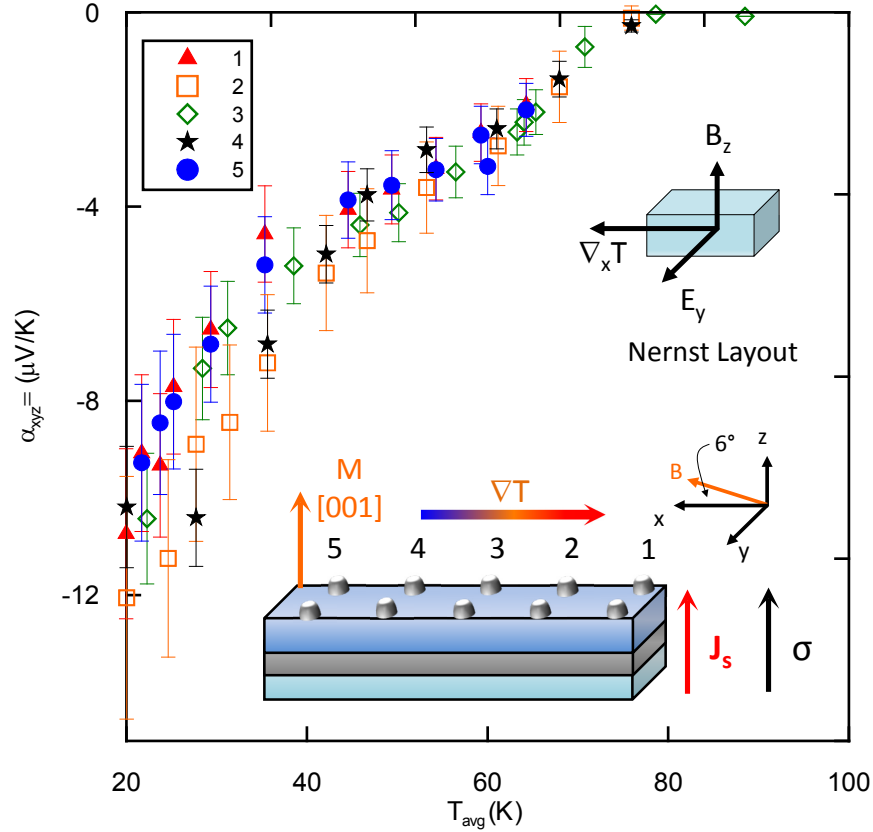


Figure 40: Nernst coefficient versus temperature. Point contact #1 is at the hot end, and the numbers monotonically increase toward the cold end. The insets include a schematic of the Nernst effect field and flux directions, as well as a schematic (not to scale) of the sample measured in this study. The externally applied magnetic field is approximately  $6^\circ$  off the  $xy$ -plane.

These results show that the spin-Seebeck effect generates spin-distributions and local spin currents from thermal gradients in ferromagnetic semiconductors.

### Substrate Thermal Conductivity and Low Temperature

At this point in time (early 2011), theoretical developments<sup>91,92,93</sup> were not been able to explain simultaneously the combination of the persistence of the effect after the severance of electrical communication, the positional dependence, and the temperature dependence. Here we provide a detailed characterization of the temperature dependence

of the spin-Seebeck coefficient ( $S_{xy}$ ), magnetization ( $M$ ), and thermoelectric power (thermopower or  $\alpha_{xx}$ ) of the ferromagnet, alongside the thermal conductivity ( $\kappa$  and specific heat ( $C_p$ ) of the substrate. The measurements reveal a direct correlation with the amplitude and temperature dependence of the spin-Seebeck coefficient in multiple samples from which we conclude that the spin-Seebeck effect is driven by phonons. We developed a simple phenomenological model involving magnon-phonon drag that explains the general features of the temperature dependence and the spatial dependence of the spin-Seebeck effect in GaMnAs.

Here we concentrate on the magnitude  $S_{xy}$  on a cold-side contact near  $x=-L/2$ , where it is maximal, thus allowing for the best signal to noise ratio. The experimental methods and sample preparation are the same as described before but we modified the cryostat to enable a better heat sinking of the heat applied to the sample during the measurements, thus allowing lower temperature measurement. The data were measured on two samples  $4 \times 12 \text{ mm}^2$  of 30 nm thick  $\text{Ga}_{0.0842}\text{Mn}_{0.158}\text{As}$  (Figure 41) and  $5 \times 15.5 \text{ mm}^2$  100 nm thick  $\text{Ga}_{0.084}\text{Mn}_{0.16}\text{As}$  (Figure 42) both with a magnetic easy axis along  $[\bar{1}10]$ .

In Figure 42 we show  $S_{xy}(T)$ , the magnetization  $M(T)$  and the thermopower (or “charge Seebeck coefficient”)  $\alpha_{xx}(T)$  of one GaMnAs sample (green stars) alongside the sample substrate’s thermal conductivity  $\kappa(T)$ . The substrate’s specific heat  $C_p(T)$  is given in the inset to Figure 41a, and portions of  $S_{xy}$  and  $\kappa$  data are fitted to power laws. The measured  $\kappa$  and  $C_p$  are actually the sum of the contributions of both the GaAs substrate and the GaMnAs film, but in practice the 0.5 mm-thick substrate phonons dominate both because the film is only 30nm thick. The magnetization shows a ferromagnetic behavior with

$T_c \sim 135\text{K}$ . We note four distinct temperature regimes, separated by vertical dashed lines, in the spin-Seebeck effect in Figure 41.

- (1) Above the Curie temperature ( $T_c$ ) of 135 K the sample is a paramagnet, and  $S_{xy} = 0$ .
- (2) Between 85-135K both  $M$  and  $S_{xy}$  show an order parameter behavior  $(T_c - T)^{-\gamma}$ .  $S_{xy}$  increases in magnitude with decreasing  $T$  to  $|S_{xy}| \sim 0.25\mu\text{V/K}$ , demonstrating the dependence on the GaMnAs magnetization. The thermal conductivity of the substrate increases with decreasing  $T$  but much more slowly than either  $M$  or  $S_{xy}$ . The thermopower  $\alpha_{xx}$  is proportional to  $T$  as expected in a degenerately-doped semiconductor.
- (3) Between 85K and the maximum in both  $S_{xy}$  and  $\kappa$  at 35K, the magnetization varies more slowly with temperature. The thermal conductivity of the substrate increases with decreasing  $T$  as a  $T^{-1}$  law, characteristic of anharmonic phonon-phonon Umklapp scattering, then reaches a maximum at 35 K. The spin-Seebeck signal  $|S_{xy}(T)|$  follows  $\kappa(T)$  closely up to a peak of  $\sim 1.05\mu\text{V/K}$  at 35K and both  $S_{xy}(T)$  and  $\kappa(T)$  peak at the same  $T$ . The thermopower  $\alpha_{xx}$  departs strongly from the  $T^1$  and the difference forms a peak also slightly below 35 K indicative of phonon-electron drag.
- (4) Below 35K, there is a sharp decrease in  $S_{xy}(T)$  with decreasing  $T$  following a  $T^{3/2}$  law, with  $|S_{xy}|$  reaching  $\sim 0.4\mu\text{V/K}$  at 15K on the sample in Fig. 2. The specific heat of the substrate follows a  $T^3$  law consistent with the Debye model, though a slightly slower slope appears at the lowest temperatures, which may be due to an

incipient electron ( $C_p \propto T$ ) or a magnon ( $C_p \propto T^{3/2}$ ) contribution. The thermal conductivity also follows a  $T^3$  law down to 10K: this is understood by realizing that the phonon mean free path  $\Lambda$  now is a constant of the order of the sample thickness, and  $\kappa = 1/3 C_p v \Lambda$ , where  $v$  is the sound velocity. Again, there is excess conduction at the lowest temperature, possibly due to the same cause as in  $C_p$ . The phonon-drag effect on the thermopower  $\alpha_{xx}$  decreases at lower  $T$  where it diminishes to zero at 0K. The spin-Seebeck coefficient decreases following a  $T^{3/2}$  law, which is also the temperature-dependence of a magnon specific heat.<sup>94</sup>

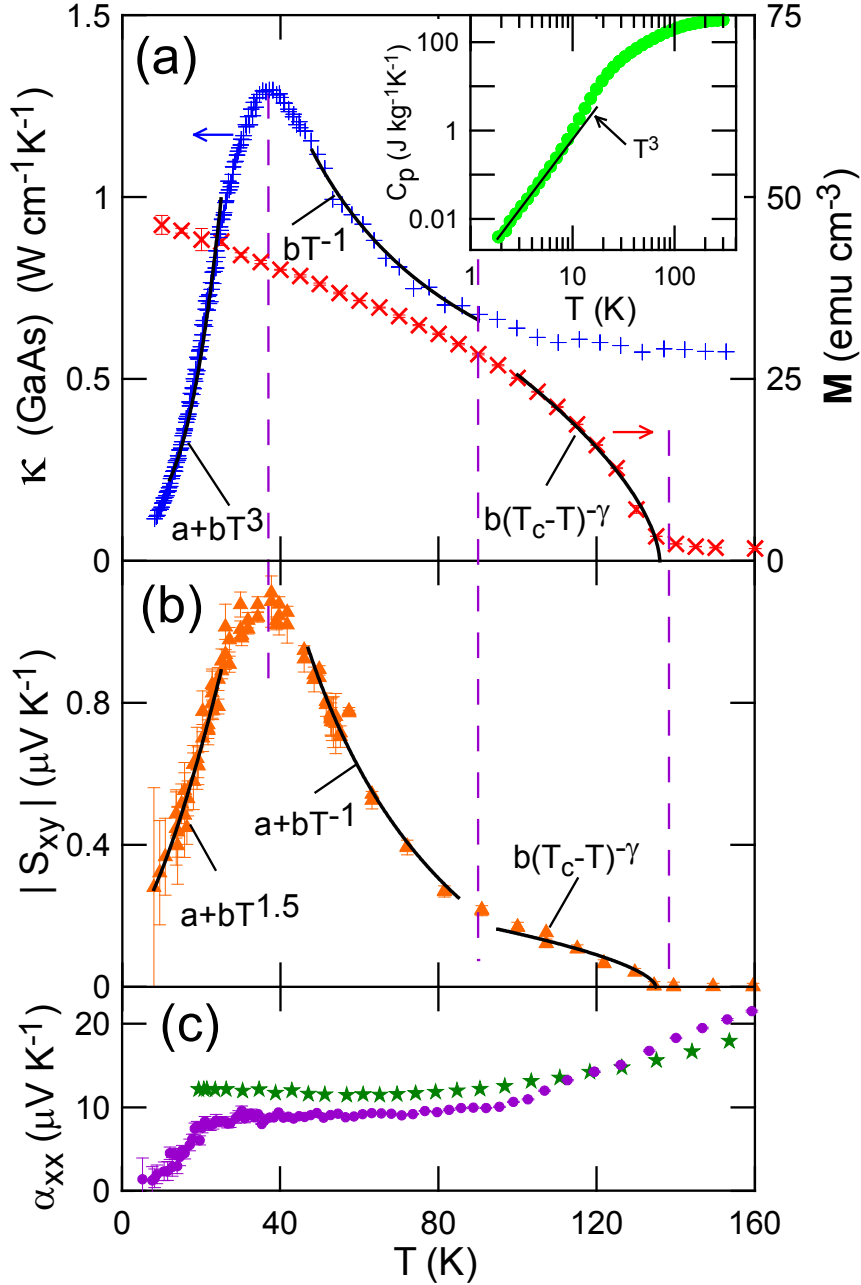


Figure 41: Thermal properties of one GaMnAs/GaAs sample versus temperature. (a) Magnetization of the GaMnAs and substrate (GaAs) thermal conductivity. The inset shows the substrate specific heat. (b) Spin-Seebeck coefficient  $S_{xy}$  of the GaMnAs. (c) Thermopower  $\alpha_{xx}$  of the sample (green stars) and of a similar sample (purple dots). The vertical dashed lines divide the figure into four ranges. Fits described in the text.

The above trends are reproduced on a second sample grown on a higher quality GaAs substrate, and consequently ten times higher peak thermal conductivity (Figure 42). The maximum in  $\kappa(T)$  is now lowered to  $\sim 10-15$  K although the extremely high thermal conductance of the sample makes an accurate measurement near the maximum difficult because the temperature gradients become very small. The spin-Seebeck coefficient now peaks at 10 K instead of 35 K in the previous sample (Figure 41). As the Pt strips on the two different samples are not exactly at the same  $x$  position nor do they have exactly the same thickness nor coupling to the GaMnAs, we refrain from a direct comparison. We do note that the sample in Figure 41 at 50 K  $|S_{xy}| \sim 0.75 \mu\text{V/K}$  which peaks at  $\sim 1.05 \mu\text{V/K}$  at 35 K while the sample in Figure 42 at 50 K  $|S_{xy}| \sim 0.2 \mu\text{V/K}$  which peaks at  $\sim 4 \mu\text{V/K}$  at 10 K. The magnitude scales roughly with the absolute value of the substrate thermal conductivity. The smaller value at of  $S_{xy}$  50 K for Figure 42 is because the Pt strip was located further away from the hot end of the sample ( $x = -L/2$ ). The phonon-drag peak in  $\alpha_{xx}$  is now a prominent feature with a maximum again at  $\sim 10-15$  K. This reveals that the amplitude of the spin-Seebeck effect in GaMnAs scales with the thermal conductivity of the substrate as well as with the intensity of phonon-electron drag in the thermopower as a function both of substrate condition and of absolute temperature. The observation that spin-Seebeck scales with thermal conductivity and phonon-electron drag is consistent with recent publications invoking magnon-phonon drag as a mechanism at least contributing to the spin-Seebeck signal of the ferromagnetic insulator YIG.<sup>4</sup>

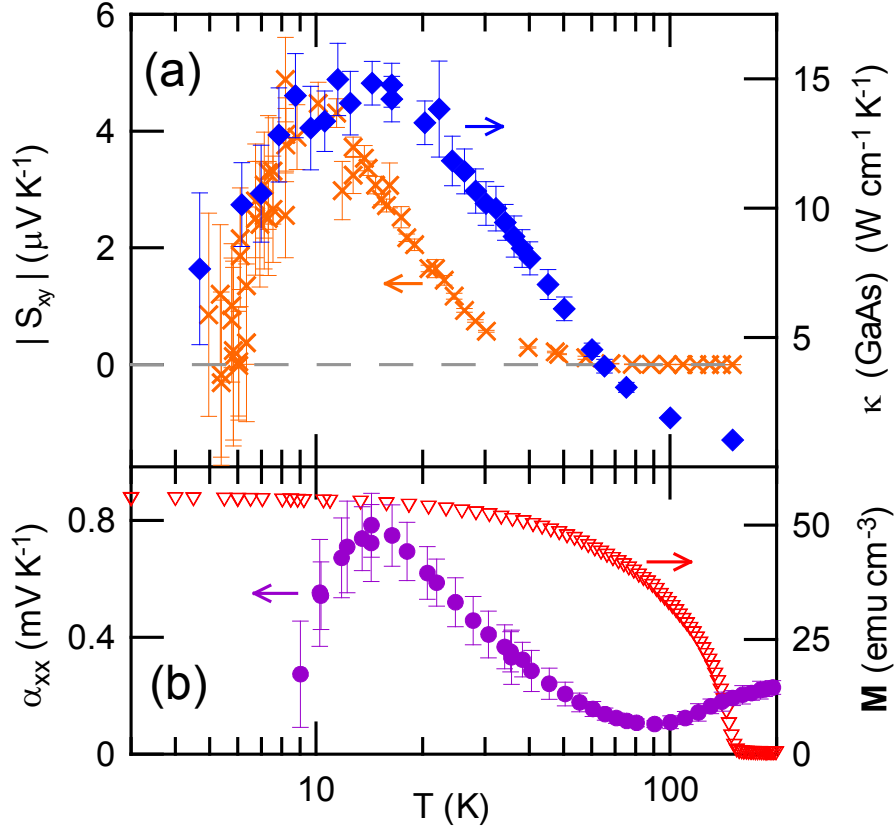


Figure 42: a) spin Seebeck coefficient and thermal conductivity and b) thermopower on high thermal conductivity GaAs substrate.

### Theory of Spin-Seebeck Effect in Ferromagnetic Semiconductors

First, we review the mechanism behind the phonon-electron drag contribution to the thermopower  $\alpha_{xx}$ . At higher temperatures, the classical diffusive thermopower is governed by the Boltzmann equation. In this regime, and for degenerately-doped semiconductors,  $\alpha_{xx} \propto T$  as observed above 90 K in Figure 41. Here electrons and phonons are constantly being brought back to mutual equilibrium by collisions, and the temperature gradient creates only a small perturbation of the electron equilibrium distribution function. When electron-phonon interactions dominate over other scattering mechanisms of both electrons and phonons, the phonon drag thermopower adds to the

diffusive thermopower in the form of a peak at a certain temperature. When enough phonons interact with electrons, rather than with other phonons or impurities and defects, they impart momentum to the electrons along  $\nabla T$  and move the electron distribution function away from equilibrium, resulting in an extra phonon-drag thermopower that can be orders of magnitude larger than the diffusive thermopower. The amplitude of this effect scales with the ratio between phonon/electron and phonon/phonon or phonon/defects interaction cross-sections, as well as with the density of phonons available to interact with the electrons. Therefore, in metals the phonon-drag thermopower peaks at a temperature close to the maximum in lattice thermal conductivity. Above that maximum, Umklapp processes compete with phonon-electron interactions to bring the phonons back to equilibrium, while below that temperature the number of phonons decreases following the Debye specific heat. The situation in degenerately-doped semiconductors is only slightly different: as observed in Figure 41 and Figure 42 the temperature of the maximum in the phonon drag contribution can differ somewhat from that of the maximum in the lattice thermal conductivity because it depends on the cross-section of the Fermi surface and the number of phonons that can interact with electrons on that surface. Comparing the two samples illustrates that the lower the phonon-phonon and phonon-defect interactions, the higher the relative magnitude of phonon-electron drag and the concomitant thermopower  $\alpha_{xx}$ .

In Figure 43, we offer a qualitative outline of the role of substrate phonons in the thermally-induced spin distribution. At least in the case of ferromagnetic insulators<sup>4</sup> the driving force for phonon-magnon drag is the difference between the temperature of the magnons  $T_M(x)$  in the ferromagnetic film and that of the phonons  $T_P(x)$  in the GaAs

substrate and in the film (Figure 43a), and, given the similarities between our observation of the spin-Seebeck effect in GaMnAs and that in YIG, we assume a similar case to hold here. The drag force only arises in the presence of a temperature gradient, which imparts an excess momentum to the phonons; in the absence of a gradient,  $T_M(x) = T_P(x)$  at all  $x$ . In the presence of a gradient,  $T_P(x)$  follows a linear profile between the hot and the cold end of the sample (Figure 43a). We assume that the temperature baths at the ends of the sample, i.e. the heater at the hot end and the heat sink at the cold end, only connect to the phonons, and that the magnons that interact with phonons can tunnel large distances and thus cross the 300  $\mu\text{m}$  gaps in the film resulting in an uninterrupted  $T_M$  profile (Figure 36). The difference  $\Delta T_M(x) = T_P(x) - T_M(x)$  between the two is calculated to follow a  $\sinh(x/\lambda)$  law<sup>94</sup> (Figure 36), and mirrors the observed spatial dependence of  $S_{xy}(x)$ . Near the center of the sample,  $\Delta T_M(x \sim 0)$  must be zero; the exact location depends on the thermal symmetry of the setup, in particular of the coupling to the reservoirs at the ends of the sample, and can be slightly offset from  $x = 0$ . At the hot end of the sample,  $\Delta T_M(x < 0) > 0$ , phonon-magnon drag tends to heat up the magnons; the reverse holds at the cold end where the phonons cool the magnons,  $\Delta T_M(x > 0) < 0$ .

Assuming for simplicity the classical picture for the magnons as perturbations of the spins residing Mn ions in the presence of a magnetizing applied field  $H_x$ , the local moments fill cones shown in Figure 43, and the average magnetic moment  $M_x(T, H_x)$  is the projection of these local moments along  $x$ . The zeroth order effect of the temperature gradient on these moments is via the temperature dependence of  $M_x(T_M(x))$  as seen in Figure 41a. Here, we envision a more dominant phonon-magnon drag mechanism. At the hot end of the sample, phonon drag heats up the magnons considerably above their

thermal equilibrium, resulting in a decrease of the average moment by a quantity  $\Delta M_x$  ( $x < 0$ )  $< 0$ , as shown in Figure 43c. At the cold end of the sample, the effect of drag is to cool the magnons, increasing their average moment by  $\Delta M_x(x > 0) > 0$ . Thus  $\Delta M_x(x) \sim \Delta T_M(x) \sim \sinh(x/\lambda)$ . The dependence of  $\Delta M_x$  on substrate  $\kappa$  and on  $T$  is a function of the intensity of the phonon-magnon drag. As with phonon/electron drag,  $\Delta M_x$  will therefore depend on the density of dragging phonons, and on the ratio of phonon/magnon to phonon/phonon and phonon/impurity interaction cross-sections. This is consistent with the observation that  $\Delta M_x(T) \sim \kappa(T)$  at least for  $T$  above the maximum in  $\kappa$ .

At  $T < 35$  K for the sample in Fig. 2, where  $S_{xy}$  and  $\alpha_{xx}$  have a maximum, the magnon specific heat scales with  $T^{3/2}$ , rather than the  $T^3$  for the phonons, and this is again consistent with the observed slope of  $S_{xy}(T < 35\text{K})$  (Figure 41b). Similar behavior is observed for the sample in Figure 42, where the maximum now appears at a lower temperature of 15 K.

Next we consider the effect of  $\Delta M_x(x)$  on the distribution of spin-polarized electrons. In GaMnAs, the charge carriers are highly spin-polarized (85%) holes.<sup>95</sup> The fact that a true zero (not an offset) is measured for  $S_{xy}(x \sim 0)$  near the middle of the sample indicates that spin polarized holes are not simply thermally diffusing into Pt since otherwise we would measure a signal even near  $x = 0$  due to the inherent spin polarization of the Fermi carriers. The fact that a spin current in Pt is generated only in regions where there is a non-equilibrium spin distribution suggests that the two are related. Perhaps the non-equilibrium spin distribution (Figure 43) is maintained by a continuous transfer of angular momentum to the magnons, thus requiring, by

conservation, a flow of angular momentum in the form of a balancing spin-current.<sup>92</sup> The spin-current then generates a voltage due to ISHE either in the Pt transducers or in the GaMnAs layer itself.

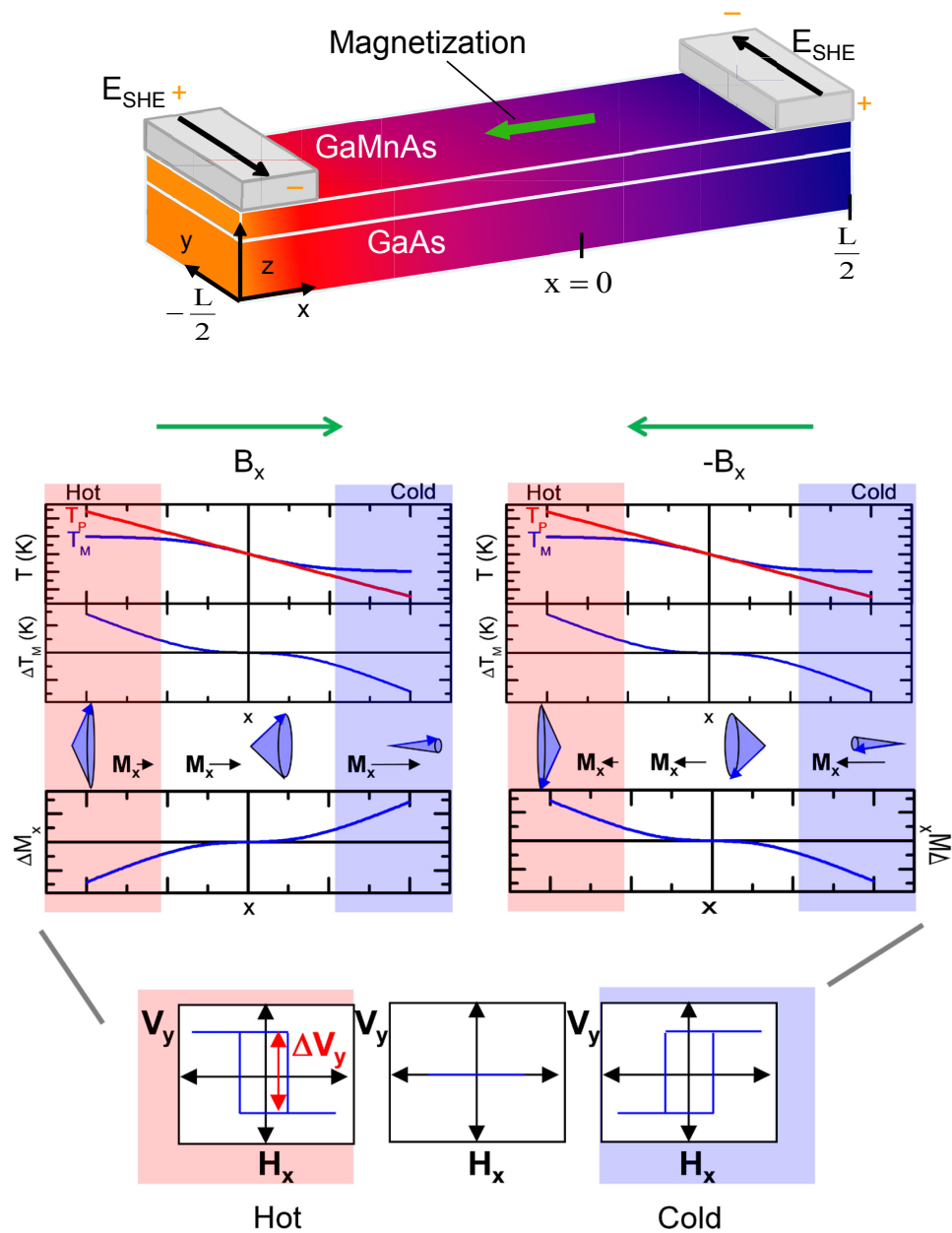


Figure 43: Spin-Seebeck effect shows odd hysteric behavior in ferromagnets. Temperature profile of phonons and magnons. The  $T$  difference between phonons and magnons act as a driving force. Cartoon showing the effect of phonon drag on the magnetic moment  $M_x$  in each region. Change in  $M_x$  due to phonon drag across the temperature gradient. Schematic hysteresis loops representing the voltage detected on the Pt strips in each region.

In conclusion, we have shown a clear correlation between the spin-Seebeck effect in GaMnAs, and the magnetization, substrate thermal conductivity, and phonon-drag thermopower. The effect of  $M(T)$  or  $\kappa(T)$  dominates different temperature ranges, with  $M(T)$  having the greatest effect above 85 K, and  $\kappa(T)$  below. The scaling holds for the dependence of the effects on both temperature and sample crystalline quality. The thermodynamic coupling of spins and phonons, shown here, opens opportunities for fundamentally new spin-caloric concepts, either in reversible thermodynamics or in transport. This may lead to phonon engineering of spin-based devices, where heat transfer can be integrated with magnetic functionality and may result in fundamentally new applications, like spin-based cooling.

### **Indium Antimonide: A Non-magnetic Material**

Electrons in this semiconductor can be highly spin-polarized in an applied magnetic field due to the relativistic spin-orbit interaction. Here we describe a spin-Seebeck effect that is three orders of magnitude larger ( $\sim\text{mV/K}$ ) occurring in a non-magnetic material, InSb. We propose that the spin-Seebeck effect in InSb is mediated by phonons that strongly drag electrons, thereby changing the electron's momentum and consequently modifying their spin-polarization through the spin-orbit effect. These results show that thermal spintronic effects can be comparable to classical thermopower in materials with simultaneously strong phonon-electron drag and spin-orbit coupling.

At the time of this work, it was understood<sup>91,92,93</sup> that the spin-Seebeck effect in ferromagnets (FM) results from the interaction between phonons and excitations of

magnetic ions (magnons) that creates a gradient in the magnetization across the sample. At steady state, the phonon driven excitation of magnons out of equilibrium is balanced by damping back to equilibrium. This dissipation of angular momentum generates a spin current flowing into an adjacent non-magnetic metal, a process called spin-pumping.<sup>93</sup> The amplitude of the effect is enhanced in the presence of strong phonon-magnon drag, and in the GaMnAs/GaAs system the highest spin-Seebeck effect value obtained ( $\sim 5 \mu\text{V K}^{-1}$ ) was reached when the lattice thermal conductivity and phonon-electron- drag were maximal (Figure 42). To maximize these effects here, we selected a system in which phonon-drag (PD), spin-orbit (s/o) coupling, and spin polarization are all three maximized: InSb.

Here we introduce a slight modification to the spin-Seebeck coefficient; we remove the factor of  $1/2$  that was used for ferromagnets, as the measured  $\Delta V_y$  was indeed twice the  $V_{\text{ISHE}} \cdot S_{xy} = E_{\text{ISHE}} / V_{xT}$ , and we retain the same units ( $\mu\text{V K}^{-1}$ ).

### **Material Background**

InSb crystallizes in a zincblende structure with  $a=0.648 \text{ nm}$ . The Fermi surface for lightly-doped InSb at low temperatures is spherical and located at the center of the Brillouin zone leading to isotropic behavior with  $m^* = 0.0136 m_e$  and  $\varepsilon_g = 235 \text{ meV}$  at  $4.2\text{K}$ .<sup>47</sup>

The InSb samples studied here (single crystals) are high-mobility ( $\mu \sim 120,000 \text{ cm}^2\text{V}^{-1}\text{s}^{-1}$ ) and lightly n-type ( $n=3.7 \times 10^{15} \text{ cm}^{-3}$ ) doped with Te. The surface of InSb has a very different charge carrier concentration than the bulk of the sample. InSb/vacuum interfaces surfaces are usually depleted, with the Fermi level pinned near the top of the

valence band (VB), but InSb/Pt interfaces attract a surface sheet of charge with  $\sim 10^{15} \text{cm}^{-2}$  holes, because the work function of Pt is much larger than the electron affinity on InSb (Figure 44a). Because  $\varepsilon_F$  is now close to 0.5eV into the VB, the light hole band has a very non-parabolic dispersion and the holes are subject to strong s/o coupling (see discussion surrounding Eq. 81 below; the s/o splitting energy for the  $\Gamma$ -point light VB is 0.8 eV<sup>47</sup>). It is likely that this inverted InSb p-layer under the Pt contributes to the ISHE effect observed in the Pt contacts themselves. A low and thin tunnel barrier (the I/V relations remain linear) separates the spin-polarized electrons and the spin-sensitive holes in InSb and electrons in Pt.

When electrons in InSb are subject to a magnetic field  $B$  they are forced to move in a helical motion; if they can complete several orbits without scattering (i.e. when  $\mu B > 1$ ), only one degree of freedom remains to their motion, that parallel to the direction of the magnetic field. The Lorentz force confines the motion in the perpendicular directions to cyclotron orbits that are quantized into Landau levels with orbital quantum number  $i$  ( $=0, 1, 2, \dots$ ). Each Landau level becomes further divided into two spin-polarized levels. The spin splitting in InSb is particularly large due to the s/o interaction. The equation of motion for the kinetic energy ( $\varepsilon$ ) of such electrons becomes, as previously discussed:

$$\gamma(\varepsilon) \equiv \varepsilon \left(1 + \frac{\varepsilon}{\varepsilon_g}\right) = \frac{\hbar^2 k_x^2}{2m^*} + \left(i + \frac{1}{2}\right) \hbar \omega_c + g s_x \mu_B B_x, \quad (94)$$

where  $\varepsilon_g$  is the energy gap,  $m^*$  is the electron effective mass,  $\hbar$  is the reduced Planck constant,  $k_x$  is the electron wave vector along  $x$ ,  $i$  is the orbital quantum number,  $\omega_c$

$(= \frac{eB_x}{m_c^*})$  is the cyclotron frequency,  $m_c^*$  the cyclotron mass,  $\mu_B$  is the Bohr magneton,  $g = -49$  the effective g-factor, and  $s_x$  is the projection of spin along  $x$  (+1/2 or -1/2). Therefore,  $g\mu_B B_x$  is the Zeeman splitting energy, the energy difference between spin-up ( $s_x=+1/2$ ) and spin-down ( $s_x=-1/2$ ) levels. For  $\varepsilon < \varepsilon_g, \gamma \sim \varepsilon$  and the energy bands are free-electron-like with  $\varepsilon \propto \hbar^2 k^2$ , but for  $\varepsilon > \varepsilon_g, \varepsilon \propto \hbar k$ , giving a linear relationship between energy and momentum.

Figure 44b shows the  $B_x$  dependence of each energy level ( $i, s_x$ ) from Eq. 81 at  $k_x = 0$ . For  $n = 3.7 \times 10^{15} \text{ cm}^{-3}$ , we calculate the location of the Fermi level  $\varepsilon_F$  at  $T = 0 \text{ K}$  (an acceptable approximation for  $T < 20 \text{ K}$  and  $B_x > 0.5 \text{ T}$ ), shown as a full line in Figure 44a. Therefore, at fields  $B_x > 1.6 \text{ T}$  most electrons occupy the lowest energy spin-polarized Landau level ( $i=0, s_x=1/2$ ), called the ultra-quantum limit (UQL). At  $T > 0$  and under the influence of  $\nabla T_x$ , a small fraction of these electrons populate the next ( $i=0, s_x=-1/2$ ) level following the Fermi-Dirac statistics.

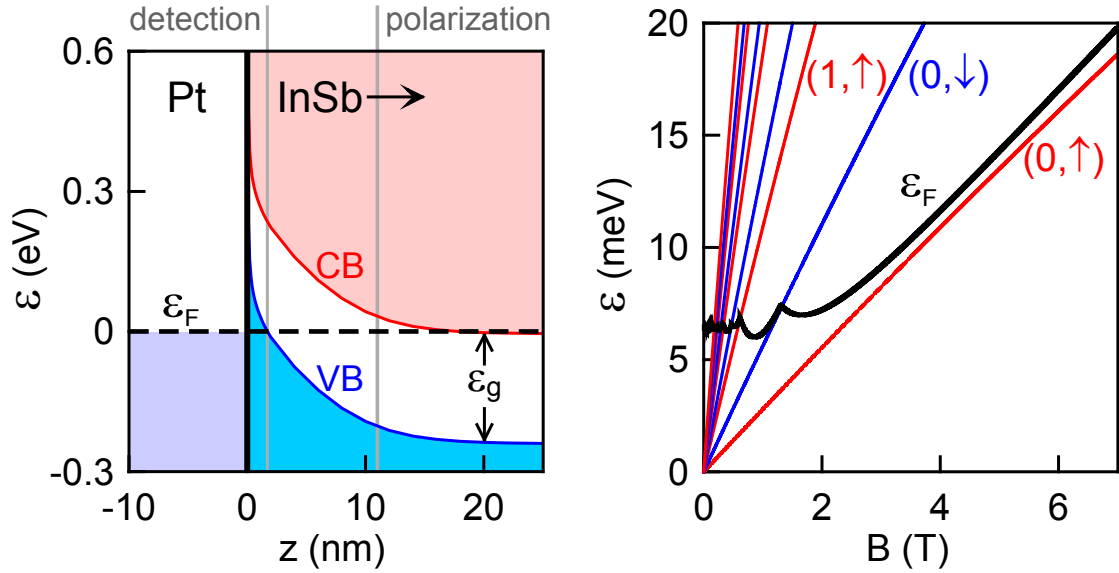


Figure 44: a) Pt-InSb interface is p-type near the InSb surface with a small depletion region. b) Fan chart for InSb and calculated  $\epsilon_F$  calculated relative to mid-gap. The data shown in this figure was calculated by Roberto Myers (a) and Joseph Heremans (b).

### Control Tests

Thermomagnetic and galvanomagnetic data are measured first without the use of a spin-sensitive detector. Classical transport properties ( $T < 10\text{K}$ ) show quantum oscillations, the Shubnikov – de Haas (SdH) effect,<sup>96</sup> as a function of  $B_x$  since  $\epsilon_F$  crosses different Landau levels as magnetic field is changed and as plotted in Figure 44. The last oscillation is observed at 1.6T, demonstrating that for  $B > 1.6\text{T}$  the sample is in the UQL see Figure 45. The temperature dependence of the electrical resistivity ( $\rho = \rho_{xx}$ ), and of the inverse Hall coefficient ( $R_H$ ) represented as  $n = 1/(R_H e)$ , and electron mobility  $\mu = R_H / \rho$ , are shown in Figure 45, alongside with the transverse magnetoresistance  $\rho_{xxz}$  and Hall  $\rho_{xyz}$  resistivities, which display SdH oscillations at  $B_x < 2\text{T}$ . The insets show the dependences up to 7T.

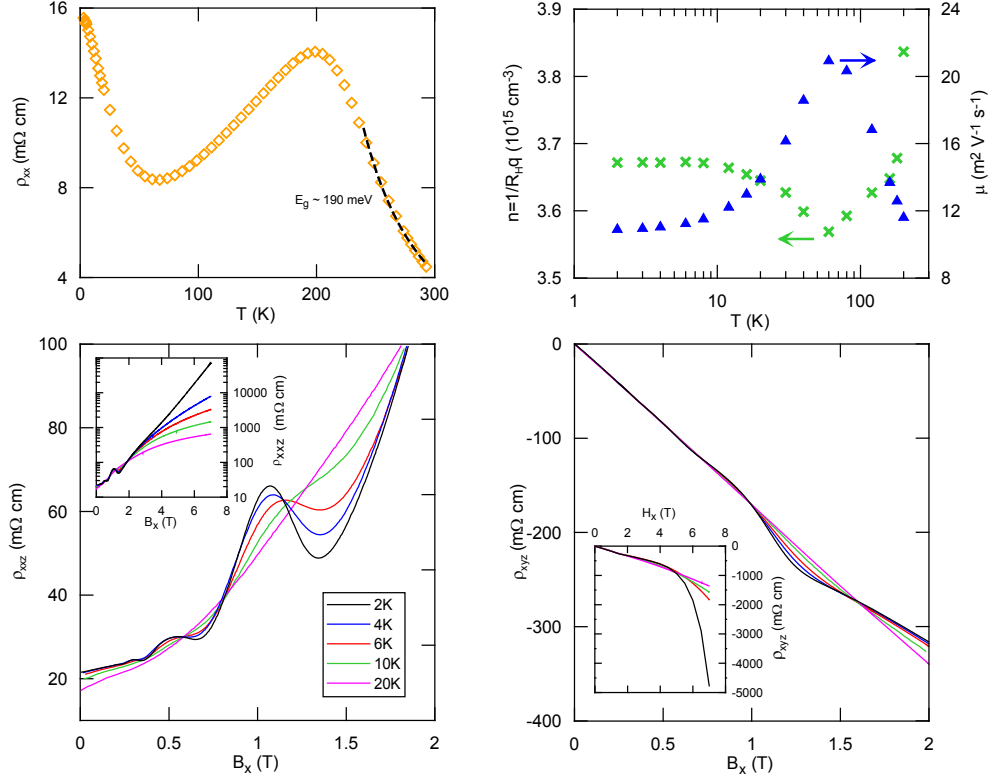


Figure 45: Galvanomagnetic properties of InSb.  $\rho(T)$  showing the band gap at higher temperatures.

At high fields and low temperatures ( $T \leq \sim 4\text{K}$ , inset in Figure 45),  $\rho_{xyz}$  shows a very strong departure from linearity. This is the magnetic freezeout effect,<sup>97</sup> which is easy to identify and is avoided in the SSE measurements.

Thermopower  $\alpha_{xx}$  shown in Figure 46 and Hall (Figure 45) confirm that the samples are n-type. The temperature-dependence of the carrier concentration  $n$  determined from the Hall coefficient seen in Figure 45 is most likely not related to a change in carrier concentration, but to a change in Hall prefactor  $r_H$ . This is defined because the relation between true carrier concentration  $n$  and the Hall coefficient is really  $R_H = r_H / (ne)$ , and we have assumed  $r_H = 1$  in Figure 45. The exact value of  $r_H$  depends on the scattering

mechanism, as discussed previously. The  $T$ -dependence of  $\mu$  suggests that at  $T < 10\text{K}$  defect scattering dominates, for  $10\text{K} < T < 50\text{K}$  ionized impurity scattering does, and  $T > 50\text{K}$  phonon scattering (acoustic and optical) dominate. Variations by 10% in  $r_H$  in those temperature ranges are thus expected.

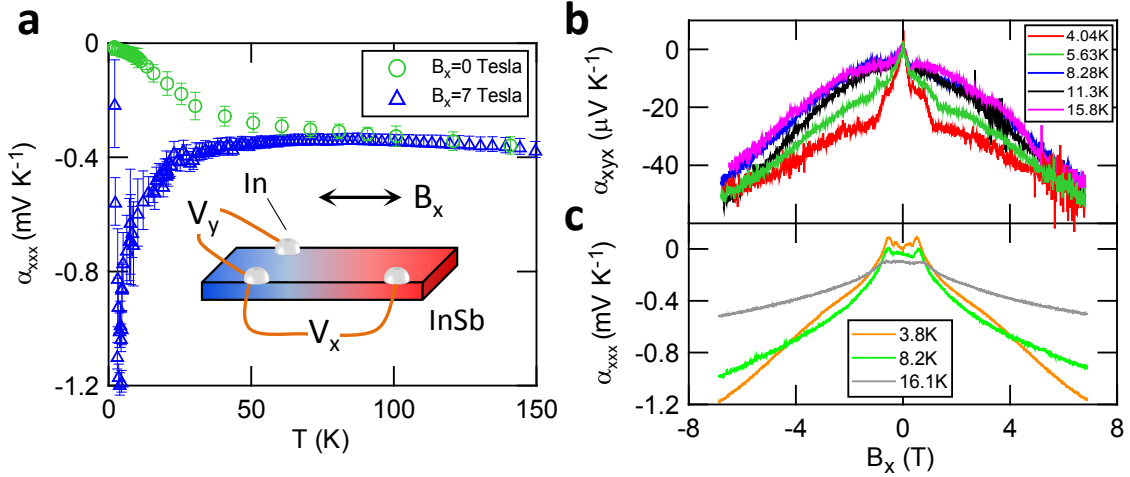


Figure 46: Thermomagnetic properties of InSb. (a) thermopower  $\alpha_{xxx}(T)$  with  $B_x // \nabla_x T$  at  $B_x = 0.7\text{T}$ . Schematic (not to scale) of In point contacts on InSb. (b)  $\alpha_{xyx}(B)$  most likely resulting from a small parasitic  $\nabla_{y,z} T$  and misalignments in Cu contact placement along  $x$ . (c)  $\alpha_{xxx}(B)$  has oscillations at low  $B$ .

The classical charge-transport properties of the samples with the magnetic field aligned parallel to heat fluxes as in the spin-Seebeck effect experiments are reported in Figure 46. Figure 46a shows the temperature dependence of the thermopower  $\alpha_{xxx}$ , at zero field and in the presence of  $B_x // \nabla T_x$ ; Figure 46c shows it as a function of magnetic field. The strong enhancement of thermopower with increasing  $T < 40\text{K}$  does not correspond to a decrease in electron concentration and is due to the onset of very strong PD. Figure 46b shows a

“planar Nernst” thermopower  $\alpha_{xyx}$ , although great care was taken to avoid small misalignments in the  $(x,z)$  plane and the reported  $\alpha_{xyx}$  may not have any physical significance; the purpose of the experiment is to show the  $E_y$  that is picked up in the same configuration as the spin-Seebeck effect shown in Figure 48 in the absence of a spin-sensitive detector. It is clear that none of the potential parasitic effects is of the same order of magnitude as the spin-Seebeck effect signals in Figure 48; neither have they the position dependence along the sample, or the magnetic field dependence of the spin-Seebeck effect signals.

As was the case for the thermomagnetic properties with  $B$  in the plane of the sample along  $x$ , these transverse thermomagnetic coefficients (except  $\alpha_{xx}(B_x)$ ) are smaller than the SSE signals (Figure 48), do not vary along the length of the sample, and display different magnetic field dependences. There are SdH oscillations below 1.26T in  $\alpha_{xxz}$  and conventional Nernst ( $\alpha_{xyz}$ ) (Figure 47). We note that in Figure 46,  $\alpha_{xx}(B_x)$  has a mostly linear dependence on  $B_x$ , with a slope of that changes by  $\sim 3$  near the UQL as the number of subbands changes from 3 to 1. In Figure 47,  $\alpha_{xx}(B_z)$  is mostly quadratic in  $B_z$ . The magnitude at low temperature can become very large, indeed comparable to the SSE, but the alignment of the sample in field is very different.

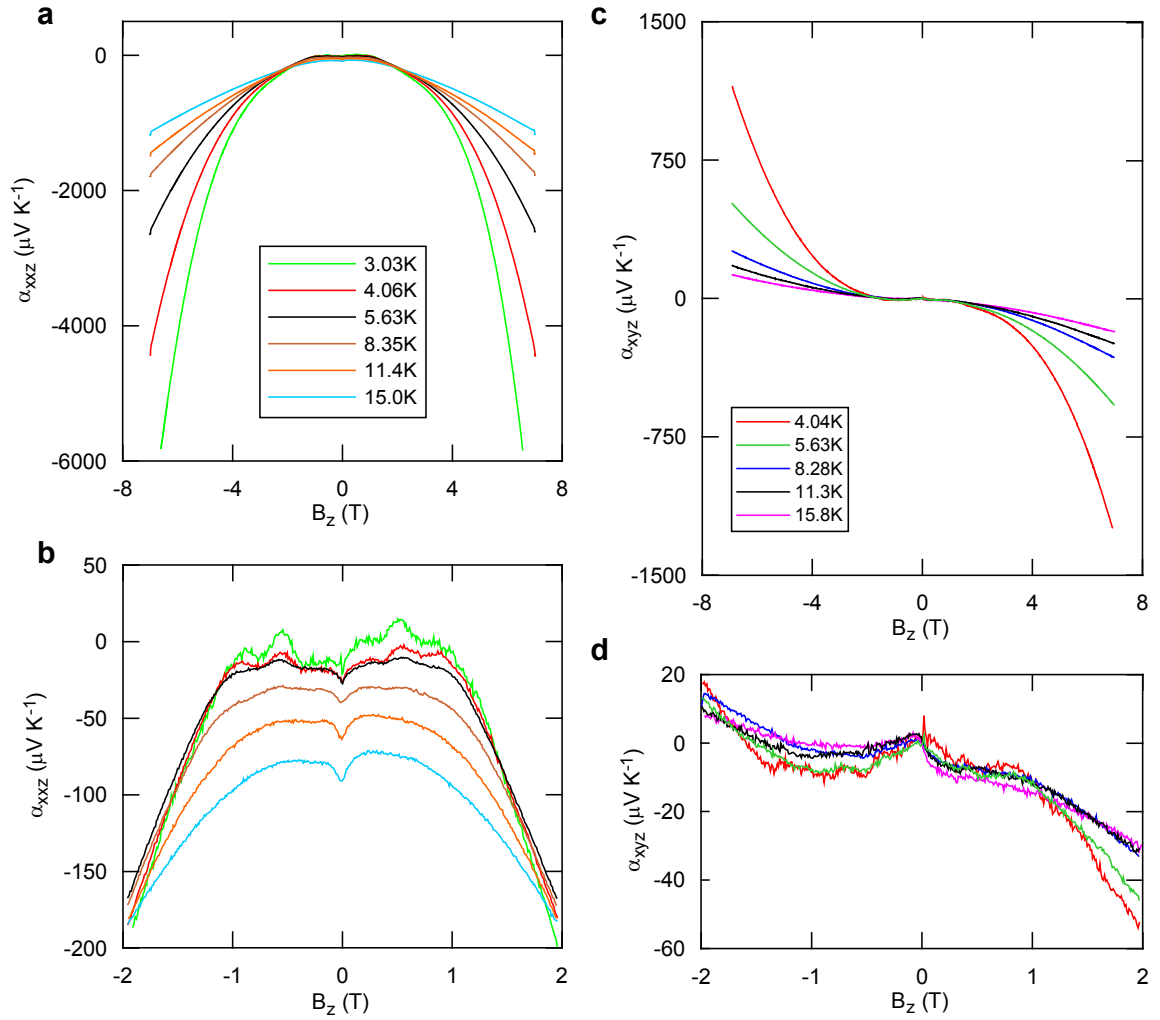


Figure 47: Thermomagnetic properties with  $B$  oriented along the  $z$ -axis. (a) and (b) are transverse magnetothermopower, and are even in  $B$ . (c) and (d) are conventional Nernst effect.

### Spin-Seebeck Effect

Figure 48 shows  $S_{xy}$  as a function of applied field,  $B_x$ , for four Pt transducers, two at the hot end (red, orange traces) and two at the cold end (green, blue traces) of the sample at four different temperatures. The hot and cold ends of the sample have antiparallel directions of  $S_{xy}$ , as was the case for the spin-Seebeck effect in FM. The traces show a large even dependence on  $B_x$ , and a small odd one, especially below the UQL. These measurements were repeated on a second sample (Figure 50), and the even part of  $V_y$  measured at 31.2K on the hottest and coldest Pt strip of that are shown Figure 49a These voltages are plotted as a function of the  $\Delta T_x$  between thermometers in Figure 49b, which illustrates that the response varies linearly with  $\nabla T_x$ , again as was the case for the spin-Seebeck effect signal in FM; this justifies a posteriori the definition of the quantity  $S_{xy} = \frac{E_y}{\nabla T_x}$ . Like in the case of the spin-Seebeck effect signal in FM, this signal is only observed on spin-sensitive detectors and displays a polarity inversion near the middle of the sample. For those reasons, we conclude that Figure 48 shows SSE signals that originate from the effect of  $\nabla T_x$  on the spin-polarized carriers in the n-type InSb.

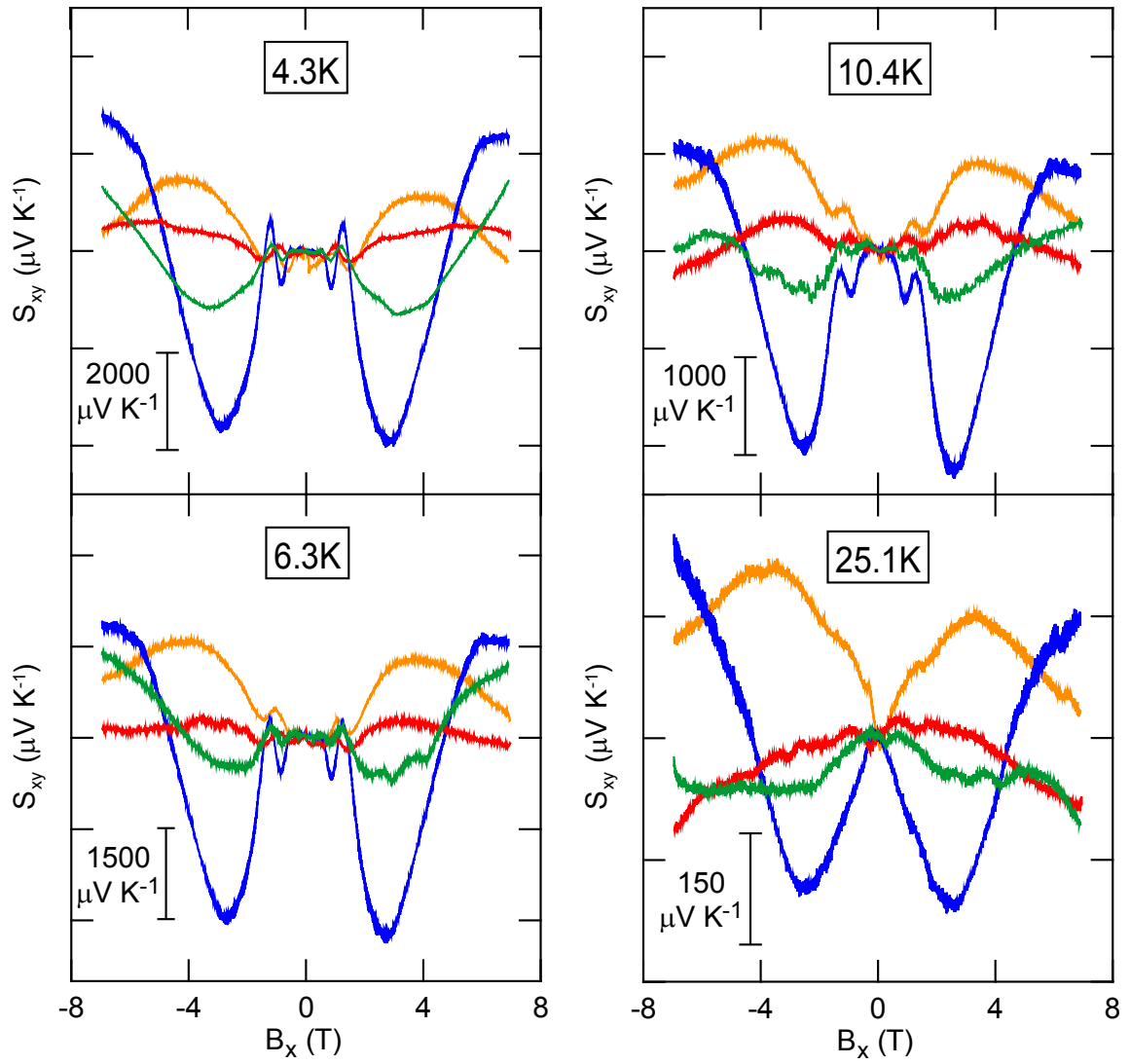


Figure 48: Experimental data on the spin-Seebeck effect in InSb.  $S_{xy}(B_x)$  on 1<sup>st</sup> InSb sample.

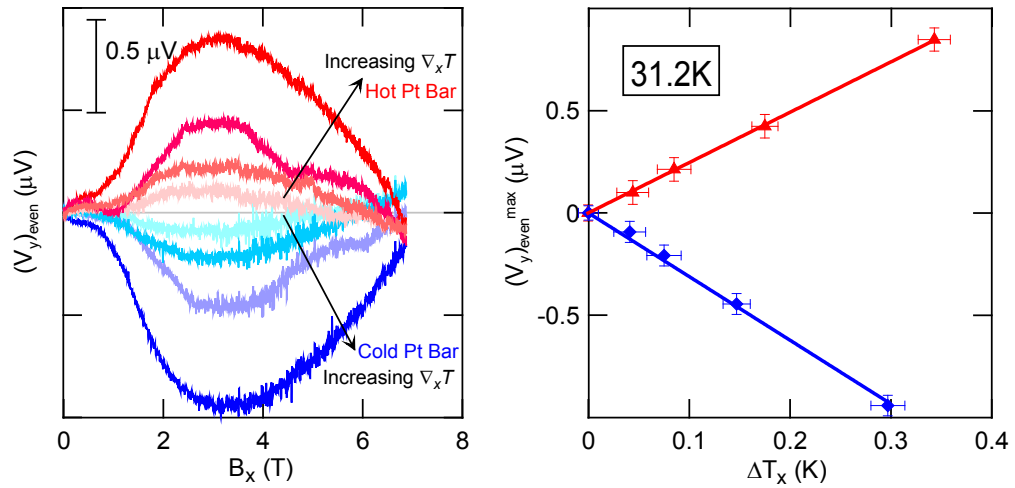


Figure 49: Even part of spin-Seebeck at various temperature gradients on second InSb sample. Magnitude of  $\Delta V_y$  scales linearly with  $\Delta T_x$ .

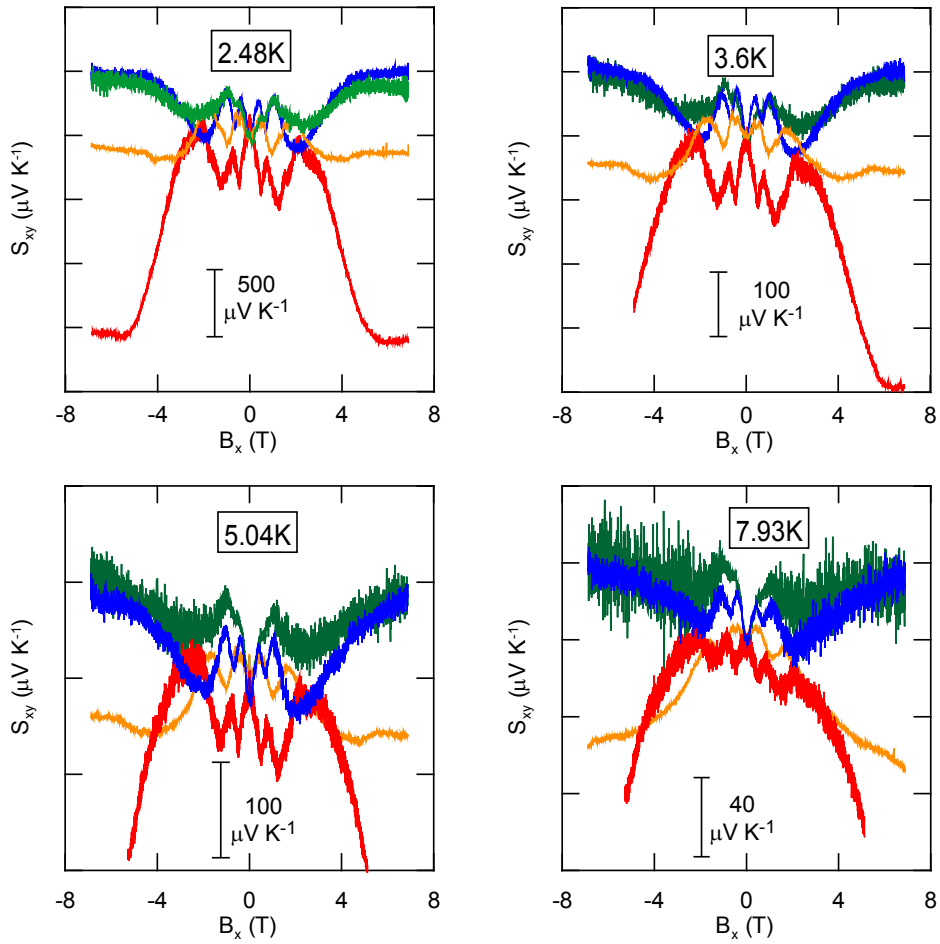


Figure 50: Spin-Seebeck effect in InSb on a 2<sup>nd</sup> sample.

In practice,  $V_y$  ( $\nabla T_x=0$ ,  $B_x=0$ ) has a residual non-zero value, especially at low  $T$ , which was subtracted out; the resulting traces are displayed in Figure 48 & Figure 50. Below the UQL in the SdH regime,  $S_{xy}(B_x)$  shows an oscillatory dependence on  $B_x$  with the same period in  $1/B_x$  as the SdH oscillations. Interestingly, above the UQL  $S_{xy}$  continues to change as a function of  $B_x$ : even though  $S_{xy}$  is sensitive to orbital quantization, its origin is clearly different than SdH. The maximum value of  $S_{xy}$  reaches  $8\text{mV K}^{-1}$  near 2.8 K, over 1000 times larger than the largest value of spin-Seebeck effect measured on a FM. That maximum is also plotted as a function of  $T$  in Figure 51. Here we see that the spin-Seebeck effect signal above the UQL persists up to 40K, a temperature far in excess of the 10-15K where the SdH oscillations disappear, reinforcing the conclusion drawn from the  $B_x$  dependence:  $S_{xy}$ , whose origin lies in spin-polarization, exists in InSb even when orbital quantization is no longer resolved.  $S_{xy}(T)$  in Figure 51 follows an  $\exp(-\Theta/T)$  function that is clearly distinct from an activated behavior and functionally similar to the Dingle-functions the SdH oscillations follow,<sup>96</sup> although much less attenuated than the latter.

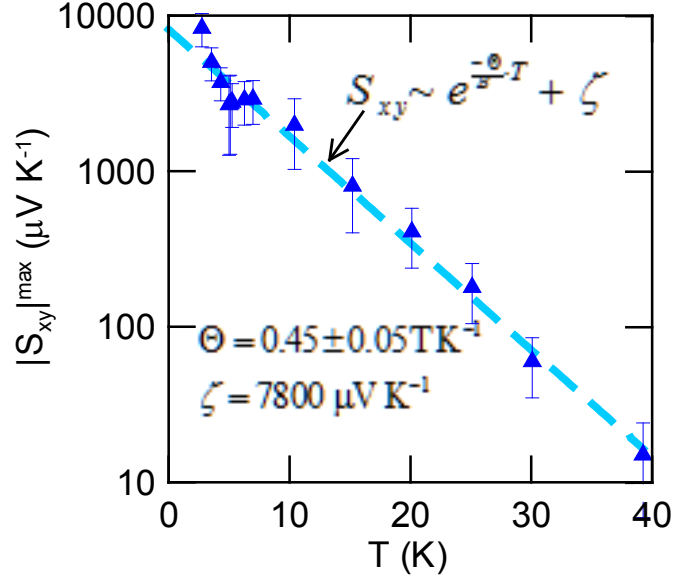


Figure 51: Maximum of  $S_{xy}$  on the cold Pt bar in sample 1 in Figure 48.

The even dependence of  $S_{xy}(B_x)$  above the UQL is opposite to that in FM where  $S_{xy}(B_x)$  has been seen to be odd. Second, phonon-magnon effects dominate in FM, while there are no magnons in InSb. Phonon-electron interactions are the dominant mobility-limiting mechanism in most conductors at higher temperatures and thus quite strong, in contrast to the much weaker phonon-magnon interactions at least in FM insulators like YIG, consistently with the relative magnitudes of the effects in the different materials.

### Mechanism of Non-magnetic Spin-Seebeck Effect

Notice that the sign of momentum change in phonon-magnon drag is not important in FM because the change in  $\mathbf{M}$  is thermally driven. Therefore the sign of the spin-current (and resulting ISHE voltage in Pt) is determined by the relative orientation of magnetization  $\mathbf{M}$ ;  $S_{xy}$  is odd with  $B_x$ . The reverse holds in InSb, because the orientation of electron spins (determined by the spin splitting) is directly coupled to their  $\mathbf{k}$ -vector through Dresselhaus s/o coupling, which dominates in bulk InSb.<sup>98</sup> Thus, when a phonon drags an electron and alters its  $\mathbf{k}$ -vector, the direction of change in momentum determines

the sign of the change in spin polarization, and therefore the sign of spin-current resulting in  $S_{xy}$ . For example, if the total spin splitting for conduction band electrons is  $\Delta\varepsilon_{\uparrow\downarrow} = \Delta\varepsilon_{g\uparrow\downarrow} - \Delta\varepsilon_{k\uparrow\downarrow}$ , where  $\Delta\varepsilon_{g\uparrow\downarrow}$  is the Zeeman-type equilibrium spin splitting and is not altered by  $\nabla T$ , and  $\Delta\varepsilon_{k\uparrow\downarrow}$  is the  $\mathbf{k}$ -dependent spin splitting, then the sign of the thermally induced spin-current (and therefore the sign of  $S_{xy}$ ) will track the sign of  $\Delta\varepsilon_{k\uparrow\downarrow}$  (see Fig. 3). Because by the band structure and s/o interactions  $\Delta\varepsilon_{k\uparrow\downarrow} \propto \Delta k_x$  and by phonon-drag  $\Delta k_x \propto q_x$ ,  $S_{xy}$  will only depend on the direction of drag vis-à-vis  $B$ . Using now the two-temperature model developed for spin-Seebeck effect in FM,<sup>92,93</sup> we define the equilibrium temperature between phonons and electrons to be in the middle of the sample, and view PD as cooling electrons ( $\Delta k_x < 0$ ) on the cold end and heating them ( $\Delta k_x > 0$ ) on the hot end of the sample. We explain next how this leads to an  $S_{xy}(B)$  that is even in  $B$ , with no dependence on the sign of the background spin splitting.

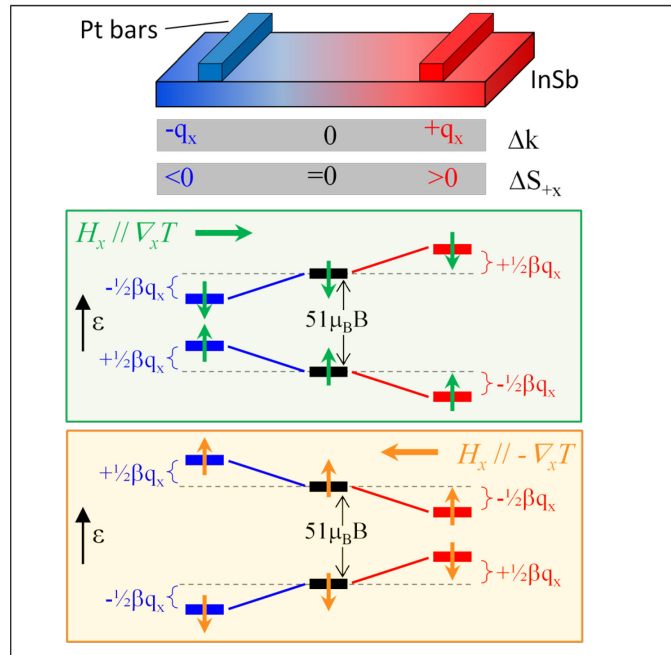


Figure 52: Explanation of spin-Seebeck effect mechanism in InSb

The s/o interaction can be understood by visualizing the rotating reference frame of an electron moving through the InSb crystal with momentum  $k_x$ . In the rotating frame, the positive ions rotate around the electron, thereby generating a magnetic field  $B_{s/o}$ . In the middle of the sample, where  $\Delta T=0$ , a free electron ( $g_f=2$ ) moving down the lattice with a momentum  $k_x$  experiences the effective magnetic field  $B_{s/o}$  from the clockwise (CW) rotation of positive ions. In the presence of an applied field  $B$ , the resulting  $\Delta\varepsilon_{\uparrow\downarrow} = g_f\mu_B(B+B_{s/o})$  is different from what it would be in free space. For InSb,  $\Delta\varepsilon_{\uparrow\downarrow} = -51\mu_B B$  (note that, because  $g\sim-51$ ,  $B_{s/o}\sim-25B$ ). At the hot end, PD increases the electron momentum, which in the rotating electron reference frame results in an increase in the apparent CW rotation of the ions, thereby increasing the spin-splitting ( $|\Delta B_{s/o}| > 0$ ). At the cold end, the PD decreases electron momentum resulting in decrease in the ion rotation, reducing the spin-splitting ( $|\Delta B_{s/o}| < 0$ ).

To get an order of magnitude of the effect, one can define locally at  $k=k_F$  an approximate Dresselhaus parameter as  $\beta \equiv \frac{\Delta\varepsilon_{\uparrow\downarrow}}{\Delta k_x}$  to represent the dependence of the splitting of the last two levels. A temperature difference of  $\Delta T$  will then increase phonon momentum by  $\Delta q \equiv \frac{k_B \Delta T}{2hc}$  where  $c$  is the average sound velocity (2660 m s<sup>-1</sup> is the average between longitudinal and transverse acoustic modes along [100] in InSb<sup>47</sup>). The Zeeman splitting will shift by  $\Delta\varepsilon_{\uparrow\downarrow} = \beta \frac{k_B \Delta T}{2hc}$ . We have no experimental value for  $\beta$  in magnetic field for the bands concerned at  $k_F$ , but can estimate its order of magnitude to be larger than 10<sup>-8</sup> meV m (obtained from using the  $k$ -linear term along [100] in Ref. [98], even though that is a zero field, and the  $k^2$  and  $k^3$  terms are known to be much larger), and

on the order of  $\hbar v_G \sim 3 \times 10^{-7} \text{ meV m}$  ( $v_G$  is the group velocity). For  $\Delta T = 40 \text{ mK}$ , as we use near  $5 \text{ K}$ ,  $|\Delta \varepsilon_{\uparrow\downarrow}|$  is of the order of tens of  $\mu\text{eV}$ , which considerably affects the Fermi distribution of electrons between the two Zeeman-split levels as  $k_B T \sim 400 \mu\text{eV}$ . Such model predicts not only that  $S_{xy}$  is an even function of  $B_x$ , but also that  $\lim_{B \rightarrow \infty} (S_{xy}) = 0$ .

There is a small odd-in- $B_x$  component to  $S_{xy}(B_x)$ , especially below the UQL where SdH oscillations are observed. We suggest that this odd component arises from the classical magneto-thermopower, an even function of field, arises from spin-polarized particles. A perturbation of carrier concentrations due to  $\nabla T$  will induce a similar perturbation in spin-polarization.

In summary, we have experimentally demonstrated the SSE in a non-magnetic material, observing a thousand-fold increase in  $S_{xy}$  relative to previous reports in magnetically ordered materials. This observation indicates that the fundamental mechanisms driving the SSE rely on an out of equilibrium spin polarization, and not directly on magnetic exchange. The magnitude and generality of this effect in turn raise the potential for further optimization and perhaps ultimately all solid-state thermomagnetic devices similar to, and possibly competitive with, current thermoelectric technologies.

## Conclusions

To summarize, we have explored the nature of the Tl chemical bond in PbTe-PbS alloys and have shown that the loss of resonance at increased S is due to chemical pressure. Further, the Tl 6s-states bond with the Te-5p orbitals, and this knowledge should help researchers narrow their search for resonant impurities to those where the s-states can interact with the host band structure. We reach a  $zT \sim 1.6$  in this material. The high  $zT$  in Tl free PbTe-PbS alloys results from the Fermi level reaching the heavy valance band; however our experimental evidence demonstrates these alloys are still direct gap semiconductors at operating temperatures, in contrast to a significant body of literature. Furthermore, contrasting the temperature dependence of the Hall coefficient in PbTeS:Tl and PbTeS:Na demonstrates that differing physical mechanisms are responsible for the high  $zT$  values reached in each material.

The spin-Seebeck effect is becoming an established effect at the boundary between the spintronics and thermoelectrics communities. Our experiments have uncovered numerous nuances of the effect, including that it is phonon driven and thus can be enhanced by phonon-magnon drag. The discovery of the giant spin-Seebeck effect in InSb has opened up a new avenue of research, leading to the possibility of designing thermo-spin generators and coolers.

## References

---

1. Uchida, K., et al., *Nature* **455** 778 (2008).
2. Adachi, H., *private communication*
3. Jaworski, C.M., et al., *Nature Materials* **8** 898 (2010)
4. Uchida, K., et al., *Nature Materials* **8** 894 (2010)
5. Jaworski, C.M., et al., *Phys. Rev. Lett* **106** 186602 (2011)
6. Rowe, D.M. (ed.) *CRC Handbook of Thermoelectrics: Macro to Nano* CRC, Boca Raton, 2005
7. Jin, H., Jaworski, C.M., and Heremans, J.P. *Appl. Phys. Lett.* (2012) *accepted*
8. Poudel, B. et al, *Science* **320** 634 (2008)
9. Snyder G.J. and Toberer E.S. *Nat. Mat.* **7** 105 (2008)
10. Harman, T.C., et al., *Science* **297** 2229 (2002); *J. Elec. Mater.* **34** L19 (2005)
11. Venkatasubramanian, R., et al., *Nature* **413** 597 (2001)
12. Vineis, C.J., et al., *Phys. Rev. B* **77** 235202 (2008)
13. Kan Koh, Y., et al., *Appl. Phys. Lett.* **94** 153101 (2009)
14. Hsu, K.F., et al., *Science* **303** 818 (2004)
15. Nielsen, M.D., *private communication*
16. Chamoire, A.M., et al., Review Article, *unpublished*
17. Morelli, D.T., et al., *Phys. Rev. Lett.* **101** 035901 (2008)
18. Nielsen, M.D., et al, *private communication*
19. Kohler, H. and Freudenberger, A., *Phys. Stat. Sol. (b)* **84** 195 (1977)
20. Preier, H., *Phys. Stat. Sol. (b)* **78** 637 (1976)
21. Ashcroft N.W. and Mermin, N.D. “*Solid State Physics*” Holt, Rinehart and Winston. 1976
22. Onsager, L., *Phys. Rev. B.* **37** 405 (1931)

- 
23. Stroud, D., *private communication*
  24. Ravich, Y.I., “*Semiconducting Lead Chalcogenides*” Plenum Press 1979
  25. Jonson, M. and Mahan, G.D., *Phys. Rev. B* **21** 4223 (1980)
  26. Gao, Y.B., Snyder, G.J., and Heremans J.P., *in preparation*
  27. Ravich, Y.I., and Vedernikov, *Proc. IX Int. Conf. on Thermoelectrics (USA)* 278 (1990)
  28. Mahan, D.G. and Sofo, J.O., *Proc. Nat. Acad. Sci.* **93** 15 7436 (1996)
  29. Jaworski, C.M., et al., *Phys. Rev. B*, **80** 125208 (2009)
  30. Jaworski, C.M., et al., *Phys. Rev. B*, **80** 233201 (2009)
  31. Pathria, R.K., “*Statistical Mechanics*” Butterworth-Heinemann, Oxford, 1996
  32. I.M. Tsidil’kovskii “*Thermomagnetic effects in semiconductors*”, Academic Press, New York, 1962
  33. Akgoz, Y.C., and Saunders, G.A., *J. Phys. C*, **8** 18 2962 (1975)
  34. Kato, Y. et al., *Science* **306** 1910 (2003)
  35. Myers, R.C., et al., *Phys. Rev. B* **74** 155203 (2006)
  36. Pei, Y., et al., *Nature*, **473** 66 (2011)
  37. Heremans, J.P., et al., *Science* **321** 554 (2008)
  38. Girard, S. et al., *J. Am. Chem. Soc.* **133** 16588 ( 2011)
  39. Jaworski, C.M., et al, *Energy & Environ. Science* **4** 4155 (2011)
  40. Bell, L., *Science* **321** 1457 (2008)
  41. Delaire, O., et al., *Nature Materials* **10** 614 (2011)
  42. Bozin, E. S. et al. *Science* **330** 1660 (2010).
  43. Abdullin, Kh A., *JETP Lett.* **40** 998 (1984)
  44. Jovovic, V., et al., *J. Appl. Phys.*, **103** 053710 (2008)
  45. Volkov BA, et al., *Physics Uspekhi* **45** (8) 819 (2002)
  46. Noda, Y., *Materials Transactions JIM*, **39** 5 602 (1998)
  47. Landolt-Börnstein Numerical Data and Functional Relationships in Science and Technology, new series Vol 17f, O. Madelung, Ed., Springer, Berlin 1983

- 
48. Preier., H., *J. Appl. Phys* **20** 189 (1979)
49. Wei S.H. and Zunger A., *Phys. Rev. B.* **55** 13606 (1997)
50. Heremans, J.P., et al. *Phys. Rev. B.* **70** 115334 (2004)
51. Veis, A.N., and Glebova, E.V., *Izv. Vyssh. Ucheb. Zaved. Fiz.* **26** 117 (1983)
52. Thiagarajan, S.J., et al., *phys. stat. sol. (RRL)* **1** 256 (2007)
53. Andreev A.A., *J de Phys. Colloque*, **11** 29 C4-50 (1968)
54. LaLonde, A.D., et al, *Energy & Environ. Sci.* **4** 2090 (2011)
55. Rogers, L.M., *Brit. J. Appl. Phys.* **18** 1227 (1967)
56. Ravich, Y.I., and Némov, S.A. *Physics-Uspeski* **41** (8) 735 (1998)
57. Airapetyants, S.V., et al., *Sov. Phys. Sol. State*, **8** 1336 (1966)
58. Andreev A.A. & Radionov, V.N. *Sov. Phys. Sem.* **1, 2**, 183 (1967); A. A. Andreev, *Sov. Phys. Solid State* **8** 2256 (1967)
59. Crocker, A.J., *J. Phys. Chem. Solids*, **28**, 10 1903 (1967)
60. Crocker A.J. and Rogers L.M., *J. Phys. Colloque* **29** C4-129 (1968)
61. Allgaier R.S. *Phys. Rev.* **119** 554-561 (1960), Allgaier, R.S. *J. Appl. Phys.* **32** 2185 (1961)
62. Kohklov, D., Lead Chalcogenides, Physics and Applications, Taylor & Francis, 2003
61. Allgaier and Houston, *J. Appl. Phys.* **37** 302 (1966)
62. Rodgers L.M. *Brit. J. Appl. Phys.* **18** 1227 (1967)
65. Tauber, R.N. Machonis, A.A. Cadoff, I.B. *J. Appl. Phys.*, **37** 4855 (1966)
66. Kolomoets, N.V., et al., *Sov. Phys. Sol. State.* **8** 2237 (1966)
67. Sitter, H. *Phys. Rev. B.* **16** 680 (1977)
68. Gibson, A.F., *Proc. Phys. Soc. B* **65** 378 (1952)
69. Dixon, *Phys., Rev.* **138** A873 (1965)
70. Ekumai, C.E., et al., *Phys. Rev B.* **85** 085205 (2012)
71. Tsu,, R., et al., *Phys. Rev.* **172** 779 (1968)
72. Jovovic, V. Ph. D. Dissertation. Ohio State University (2008)
73. Hoang K., and Mahanti, S.D., *Phys. Rev. B,* **78** 085111 (2008)

- 
74. Pei, Y., et al., *Energy Environ. Sci.*, **4** 2085, (2011)
75. Ravich Y.I., and Nemov S.A., *Physics-Uspekhi* **41** (8) 735 (1998)
76. Kaidanov, V.I., Nemov, S.A Ravich Y.I., *Sov. Phys. Semicond.* **26** 113 (1992)
77. Airapetyants, S.V. , et al., *Sov. Phys. Solid State*, **8** 5 1336 (1966)
78. Matsushita, Y., et al., *Phys. Rev. B*, **74**, 134512 (2006)
79. Bansil, A., et al., *Phys. Rev. B*, **60**, 13396 (1999)
80. Stopa, T. et al., *J. Phys.: Cond. Matt.* **16**, 4921 (2004).
81. Heremans, J.P. Ch. 12 in CRC Handbook on Thermoelectricity, D. M. Rowe, Editor, 2012 (in press)
82. Androulakis, J., et al., *J. Am. Chem. Soc.* **129** 9780 (2007)
83. Minnich, A.J., et al, *Energy Environ. Sci.* **2** 466 (2009)
84. Singh, D., *Phys. Rev. B.*, **81**, 195217 (2010)
85. Blakemore, J.S., “*Semiconductor Statistics*”, Dover Pubns (1987)
86. Crocker, A.J., and Rogers, L.M., *Brit. J. Appl. Phys.* **18** 563 (1967)
87. Rogers L.M. *Brit. J. Appl. Phys. (J Phys. D.)* ser. 2 vol. **11**067 (1968)
88. Geballe, T.H., and Hull, G.W., *Phys. Rev.* **98** 940 (1955)
89. Gould, C., Pappert, K., Schmidt, G., and Molenkamp, L., *Adv. Mater.* **19** 323, (2007)
90. K. Uchida, et al., *Sol. State. Comm.* **150** 525 (2010)
91. Adachi, H., et al., *Appl. Phys. Lett.* **97** 252506 (2010).
92. Adachi, H., Ohe, J., Takahashi, S., and Maekawa, S., *Phys. Rev. B.***83** 094410 (2011)
93. Xiao, J. et al. *Phys. Rev. B* **81** 214418 (2010)
94. D. J. Sanders and D. Walton, *Phys. Rev. B* **15** 1489 (1977)
95. J.G. Braden et al., *Phys. Rev. Lett.*, **91** 056602 (2003)
96. Shoenberg D., “*Magnetic Oscillations in Metals*” Cambridge University Press, Cambridge 1984
97. Shayegan, M. Goldman, V., Drew H.D. *Phys. Rev. B***38** 5585 (1988).
98. Dresselhaus G., *Phys. Rev.* **100** 580 (1955); *Phys. Rev. B*, **60**, 13396 (1999)